Structural and biophysical characterization of the human serotonin transporter

Inaugural-Dissertation

zur Erlangung des Doktorgrades
der Mathematisch-Naturwissenschaftlichen Fakultät
der Heinrich-Heine-Universität Düsseldorf

vorgelegt von

Daniel Worms
aus Regensburg

Hamburg, November 2018

aus dem Institut für Physikalische Biologie
der Heinrich-Heine-Universität Düsseldorf

Gedruckt mit der Genehmigung der
Mathematisch-Naturwissenschaftlichen Fakultät der
Heinrich-Heine-Universität Düsseldorf

Berichterstatter:

1. Prof. Dr. Jörg Labahn

2. Prof. Dr. Henrike Heise

Tag der mündlichen Prüfung: 24.01.2019

1 Introduction

1.1 The human serotonergic system

1.1.1 Biosynthesis and metabolism of serotonin

Serotonin (5-Hydroxytryptamine, 5-HT) is a neurotransmitter and paracrine hormone that regulates a wide range of biological processes in humans through interaction with specific receptors. It affects the cardiovascular system (vasoconstriction, hemostasis), the nervous system (mood, appetite, sexual behavior, cognitive function, circadian rhythm, sleep) and the gastrointestinal tract (intestinal movement) [1–4]. The name serotonin was proposed in 1948 [5], when a substance was isolated, that originates from blood serum and affects the vasotonus. The proposed structure was confirmed in 1951 [6] by chemical synthesis of 5-HT (Figure 1.1).

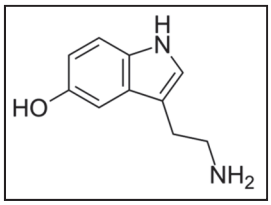

Figure 1.1: Chemical structure of serotonin.

Serotonin is widely distributed throughout nature. It is found in single-celled eukaryotes, all bilateral animals as well as in fungi and plants [7–9]. The serotonergic system of messenger and receptor is one of the phylogenetic oldest signal transmission system among animals and the primordial 5-HT receptor is thought to have evolved 700-800 million years ago [10]. In animals, including humans, serotonin is primarily found in the central nervous system (CNS), in the gastrointestinal (GI) tract and in blood platelets. The majority of 5-HT (~ 95 %) is located in the intestine, where it is synthesized by enterochromaffin cells and by serotonergic neurons of the myenteric plexus and plays an important role for peristaltic movement [11,12]. Within the CNS, 5-HT is almost exclusively synthesized in neurons originating in the raphe nuclei that project diffusely to all parts of the CNS, where 5-HT modulates neuronal processes and interacts with other neurotransmitter systems. [13,14] (Figure 1.2). Blood platelets are not able to synthesize 5-HT, but they possess a high-affinity 5-HT uptake system and therefore take it up from the blood as they pass through the intestinal circulation [12]. Serotonin is stored in and released from blood platelets to promote vasoconstriction of small vessels as well as platelet aggregation in order to improve wound healing [15,16].

Synthesis of 5-HT is a two-step reaction, which uses the amino acid L-tryptophan as the precursor molecule [12,17]. The first and rate limiting step is the hydroxylation of L-tryptophan

by the enzyme tryptophan hydroxylase (TPH) producing 5-hydroxtryptophan (5-HTP) [18]. In a second enzymatic step, 5-HTP is decarboxylated by L-aromatic amino acid decarboxylase to yield the final product 5-HT.

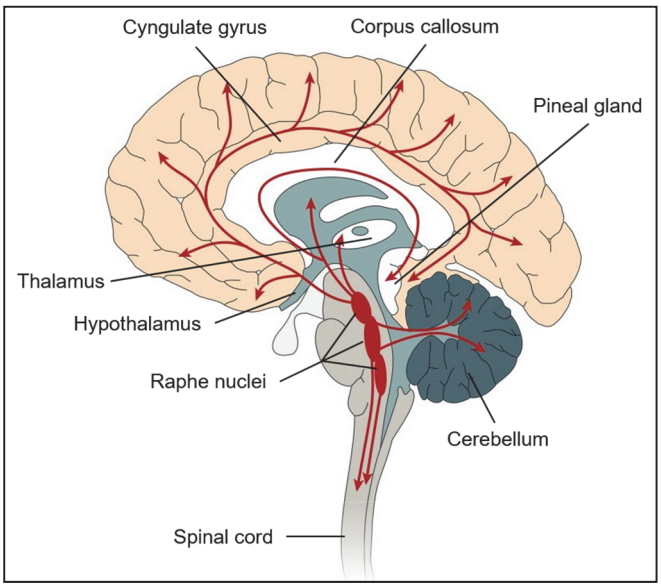

Figure 1.2: Innervation of serotonergic neurons in the CNS. Serotonin is synthesized in neurons originating in the raphe nuclei. These neurons innervate the spinal cord, the cerebellum and virtually all other brain regions (Figure adapted from [13]).

Following synthesis in a serotonergic neuronal cell, 5-HT is transported by the vesicular monoamine transporter 2 into vesicles, where it is stored until release (Figure 1.3). Upon neuronal stimulation, the vesicles fuse to the presynaptic membrane and release 5-HT into the synaptic cleft through exocytosis. The neurotransmitter binds to a specific receptor located at the postsynaptic membrane. Receptor activation upon 5-HT binding leads to a signal transduction via second messengers towards the neuron's soma. Furthermore, 5-HT can bind to a presynaptic autoreceptor on the neuron from where it was released provide feedback and regulate the cell's plasticity [19]. Eventually, 5-HT will be released from the receptor and will be taken up into the presynaptic neuron or into a neighboring glial cell through the serotonin transporter (SERT) to terminate the signal transduction [20]. Serotonin can then be recycled and stored in vesicles until future reuse [21] or it is degraded by the isoenzymes monoamine oxidase (MAO) A and, to a lesser extent, by MAO-B to 5-hydroxyindolacetic acid (5-HIAA), the main metabolite of 5-HT [22,23]. Another metabolic pathway coming from 5-HT leads to the production of melatonin, a pineal gland hormone that regulates the circadian rhythm [24].

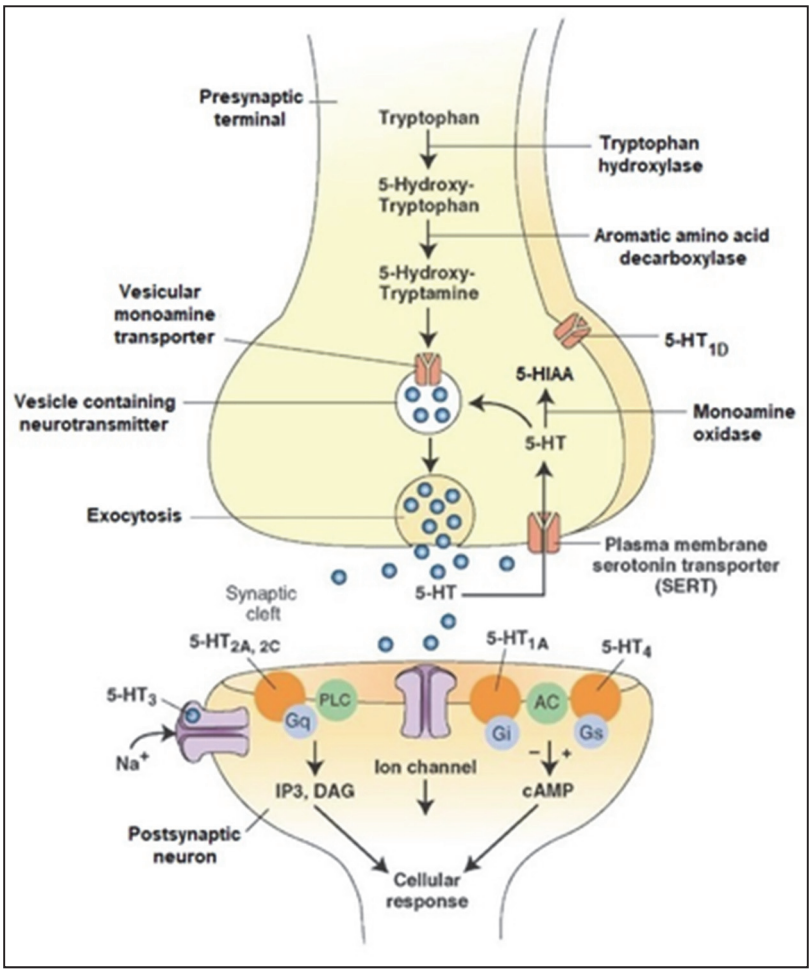

Figure 1.3: Lifecycle of a serotonin molecule. After synthesis of 5-HT in the neuron, it is stored in vesicles. Upon neuronal stimulation, vesicles fuse to the presynaptic membrane and release 5-HT into the synaptic cleft. The neurotransmitter binds to a specific receptor located at the postsynaptic membrane, where it triggers a signal transduction. Furthermore, 5-HT can bind to a presynaptic receptor on the neuron where it was released to provide feedback and regulate the cell's plasticity. Eventually, 5-HT is released from the receptor and will be taken up into the presynaptic neuron through the serotonin transporter (SERT) to terminate the signal transduction. Serotonin can then be recycled and stored in vesicles until future reuse or it is degraded by monoamine oxidase to 5-hydroxyindolacetic acid (5-HIAA), the main metabolite of 5-HT (Figure adapted from [25]).

1.1.2 Function of serotonin receptors

The wide physiological role of 5-HT is explained through the diversity of 5-HT receptors. Currently, 14 different types of 5-HT receptors are known, which are classified into seven families based on their structure, transduction mechanism and binding properties [26]. Except for 5-HT_3, all other 5-HT receptors belong to the rhodopsin family of G protein-coupled receptors (GPCRs) [27]. These membrane receptors are bound to a heterotrimeric G protein that carries a guanosine diphosphate (GDP) molecule at the G_α subunit in its inactive state. Binding of a ligand, e.g. 5-HT, leads to a conformational change in the receptor, which allows the receptor to act as guanine nucleotide exchange factor [28]. Exchange of GDP against

guanosine-5'-triphosphate (GTP) leads to the dissociation of the G protein subunits $G_{\alpha \cdot GTP}$ and $G_{\beta\gamma}$. These subunits interact with other intracellular proteins to continue the signal transduction cascade while the GPCR is able to bind another G protein [29]. The signal transduction pathway as well as the mechanism depends on the type of G_{α} subunit. There are two different pathways involved in the signaling of GPCRs: the cyclic adenosine monophosphate (cAMP) and the phosphatidylinositol (IP_3/DAG) pathway [30]. The $G_{\alpha s}$ subunit of 5-HT_4, 5-HT_6 and 5-HT_7 affects the enzyme adenylate cyclase (AC), which converts cytosolic adenosine triphosphate (ATP) to the second messenger cAMP and leads to an elevated cellular cAMP level with excitatory potential. In contrast to that, the $G_{\alpha i}$ subunit of 5-HT_1 and 5-HT_5 receptors inhibits AC, which leads to a decreasing cellular cAMP level. These receptors show an inhibitory potential. Subunits of the type $G_{\alpha q}$ target the IP_3/DAG pathway and activate phospholipase 2, which hydrolyzes phosphatidylinositol 4,5-bisphosphates into two second messengers: inositol 1,4,5-trisphosphate (IP_3) and diacylglycerol (DAG). IP_3 diffuses through the cytosol and binds to its receptor at the endoplasmatic reticulum to stimulate the release of Ca^{2+} ions into the cytosol, while DAG and Ca^{2+} activates protein kinase C [26,31–33]. The 5-HT_3 receptors belong to the Cys-loop ligand-gated ion channel superfamily. These receptors are cation-selective (Na^+, K^+, Ca^{2+}) and ligand induced activation of the receptor leads to opening of the channel. In turn, this neuronal depolarization, which is predominantly carried by Na^+ and K^+ ions, leads to a neuronal excitation within the central and peripheral nervous system [34,35].

The following list gives a short overview of different receptor types and their involvement in regulating physiological processes as well as their pathophysiological role:

- 5-HT_{1A}, 5-HT_{2A}, 5-HT_{2C}, 5-HT_6, 5-HT_7: Regulation of addiction, appetite, anxiety, learning, memory, mood, sexual behavior, gastrointestinal motility, thermoregulation, vasoconstriction [36–42,42–45]. These receptors are drug targets for the treatment of depression and anxiety in humans [46–48]

- 5-HT_{1B}, 5-HT_{1D}, 5-HT_{2B}: Regulation of addiction, anxiety, locomotion, learning, memory, mood, sexual behavior, sleep, vasoconstriction [41,49–54]. Especially 5-HT_{1B} and 5-HT_{1D} play a role in vasodilation and vasoconstriction of cerebral blood vessels and are therefore targets for migraine treatment through triptans [55,56].

- 5-HT_3: Regulation of addiction, anxiety, emesis, gastrointestinal motility, learning, memory, nausea [57,58]. Several chemotherapeutic substances induce a serotonin release from enterochromaffin cells that causes nausea and vomiting through

stimulating of 5-HT_3 receptors. Antagonists of 5-HT_3 are the primary drugs for treatment of chemotherapy-induced nausea and vomiting [12,59].

- 5-HT_4: Regulation of anxiety, appetite, gastrointestinal motility, learning, memory, mood, respiration [60,61]. This receptor type is a drug target for gastro-prokinetic agents that enhance gastrointestinal motility [62].

1.2 Serotonin and its role in depression in humans

The monoamine hypothesis of depression, first articulated in the 1960s, proposed that patients suffering from depression had depleted concentration of serotonin, dopamine, epinephrine and norepinephrine [63–66]. Evidence was found that especially serotonin plays a major role in this regard, and in 1969 it was proposed that 5-HT deficiency is causal for the formation of depression [67,68]. This hypothesis was based on the finding that the concentration of 5-HIAA, the main metabolite of 5-HT, in cerebrospinal fluid of depressive patients is reduced compared to healthy individuals [69,70]. Another study found decreased serotonin levels in depressive suicides [71]. The theory was further supported through observations made after drug induced serotonin deficiency or application of serotonin reuptake inhibitors [72]. In general, it is thought that the appearance of depressive symptoms is closely related to a serotonin household imbalance and a relative intracellular serotonin deficiency [73]. This imbalance could be due to a reduced availability of tryptophan, a reduced synthesis rate of 5-HT, a disrupted release and reuptake of 5-HT or a malfunction of post-synaptic 5-HT receptors [74]. In any case, the currently primary target of a therapeutic drug treatment is an increase of the intracellular 5-HT level.

Until today, three different classes of antidepressants have been developed. The introduction of the first antidepressant was based on serendipity: during the early 1950s, an antidepressant effect was described for isoniazid, a substance that is used in tuberculosis treatment [75]. The historical first class of antidepressants (MAOI) was named after its function to inhibit mitochondrial MAO [76] and members of this class can selectively inhibit MAO-A or non-selectively MAO-A and MAO-B. The inhibition of MAO increases the concentration of serotonin in the presynaptic terminal and makes it readily available for release upon neuronal stimulation [77]. The adverse effects and the requirement of a tyramine-reduced diet limited the use of MAOI in treatment of depression [78,79]. The second class comprises tricyclic antidepressants (TCAs). This class of drugs is named after their chemical structure that contains a core of three benzene rings. Most TCAs inhibit the SERT as well as the norepinephrine transporter (NET), thus leading to an elevated concentration of both neurotransmitters in the synaptic cleft [77]. Due to their undesired adverse-effect profile and

their non-selective pharmacological effects, the use of these drugs for treatment of depression was limited [80] and efforts were made to develop a new class of antidepressants based on rational drug design. This third class contains selective serotonin reuptake inhibitors (SSRIs), that are 20-1500-fold more selective for inhibiting SERT over NET and have minimal binding affinity for other postsynaptic receptors [81,82] while they showed fewer adverse effects, a broader therapeutic index and allowed simpler dosage strategies compared to TCAs and MAOI [83,84]. The chemical structure of one TCA and three different SSRIs used throughout this study are shown in Figure 1.4.

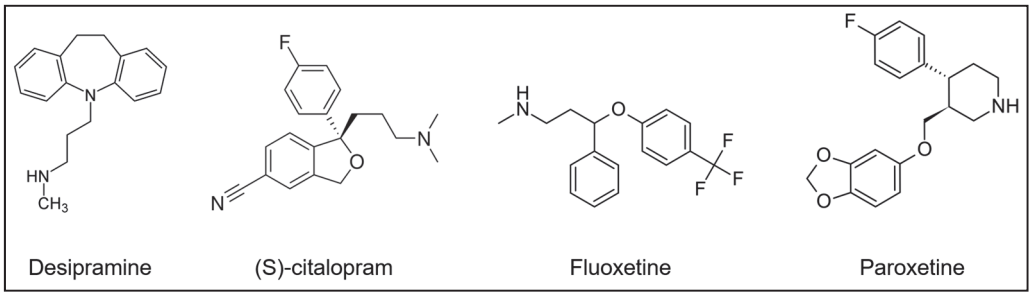

Figure 1.4: Chemical structure of SSRIs and TCAs. Desipramine contains two benzene rings fused to an azepine group and is a representative of tricyclic antidepressants (TCAs). (*S*)-citalopram, fluoxetine and paroxetine are chemically diverse compounds belonging to the class of selective serotonin reuptake inhibitors (SSRIs).

In principal, there are more ways to increase the 5-HT concentration. Admittedly, a direct treatment of depression with 5-HT is not possible due to the inability of 5-HT to cross the blood-brain barrier (BBB). Unlike 5-HT, its precursor L-tryptophan is actively transported across the BBB, but it competes with other neutral amino acids for transport [85,86] and needs to be converted to 5-HTP, which is the rate-limiting step in 5-HT synthesis [18]. This rate-limiting step can be avoided by direct administration of 5-HTP, which is also able to pass the BBB. Nonetheless, the clinical relevance of L-tryptophan and 5-HTP remains unclear. Evidence from a few placebo controlled clinical trials showed an alleviating effect on depression for both substances alone [87] or in combination with therapeutic agents (e.g. MAOI) [88], though the majority of studies were found to be inconsistent and did not allow evaluation of safety and efficacy [87,88]. Furthermore, the combination of 5-HT precursor molecules and antidepressants can lead to extremely high 5-HT concentrations, which can result in potentially fatal serotonin syndrome [89,90].

Despite the fact, that SSRIs are effective in treatment of depression and are among the most widely prescribed medications [91,92], the exact role of 5-HT in depression and antidepressant treatment remains unresolved. Although SSRIs increase extracellular 5-HT levels within minutes to hours after first application [93,94], a reduction of depressive symptoms is only found after several weeks of continuous treatment [95,96]. While some

researchers suggested that serotonin transmission is elevated in depression [97–99], the low serotonin hypothesis remains the fundamental basis of the most research in depression [100]. It is thought, that reduced 5-HT transmission is one of the more distal factors in the chain of neurological events. Ketamine, which inhibits a glutamate receptor, has rapid antidepressant effects that support the theory that depressive symptoms are more proximally controlled by glutamate transmission [101,102]. A review from 2015 concluded that 5-HT transmission is elevated in multiple depressive phenotypes and that the serotonergic system is evolved to regulate energy through oxidative phosphorylation, aerobic glycolysis and by controlling glucose homeostasis in the bloodstream [103]. Reduction of depressive symptoms is not achieved by direct pharmacological effects of SSRIs, but rather by the brain's compensatory responses (e.g. receptor internalization, reduced 5-HT synthesis rate) that attempt to restore energy homeostasis [103].

1.2.1 The serotonin transporter

Further development of new antidepressants that act on the serotonergic system requires a deep understanding of structure and function of SERT. The serotonin transporter is a membrane protein that belongs to the superfamily of neurotransmitter:sodium symporter (NSS). Members of this family catalyze substrate uptake (e.g. neurotransmitters, amino acids, osmolytes) by a substrate-sodium symporter potassium antiporter mechanism [104]. Within this superfamily, SERT belongs to the subfamily of monoamine transporters (MATs), which also includes dopamine transporter (DAT) and NET [105]. These three transporter proteins share a primary sequence homology of 40 % [106]. The serotonin transporter is located within the presynaptic membrane, where it binds to 5-HT and transports it across the membrane back into the presynaptic terminal, thus terminating the serotonergic neurotransmission. It is thereby modulating the length and intensity of serotonergic neurotransmission [107,108].

The gene encoding SERT is named *solute carrier family 6 member 4* (SLC6A4) and is found in humans on chromosome 17 on location 17q11.1-q12 [109]. The promoter region of SLC6A4 contains a polymorphism with short and long repeats (serotonin-transporter-linked polymorphic region, 5-HTTLPR) [110,111]. The long variation contains 16 repeats of a sequence while the short variant contains 14 repeats, and the short variant has been found to partly account for anxiety-related personality traits [112]. Mutations associated with 5-HTTLPR might change the serotonin transporter function and alter the level of extracellular 5-HT in the brain. Variations in the 5-HTTLPR have been associated with structural changes of the brain, resulting in a loss of grey matter in the cingulate cortex and amygdala [113]. The polymorphism was thought to be related to affective disorders [114], but a later study could not confirm this relation [115]. Similarly, it was found that 5-HTTLPR variants influences depressive responses to life stress,

an example of gene-environment interaction, but this could not be confirmed in a 2017 meta-analysis. Another study indicated that the polymorphism is related to treatment response so that long-allele patients respond better to antidepressants [116], but this association could not be confirmed [117].

1.2.1.1 Topology

Members of the MAT subfamily are integral membrane proteins, that possess 12 alpha-helical transmembrane domains (TMs), and TMs 1-5 and TMs 6-10 form an inverted-topological repeat with a central binding site for substrate and ions halfway across the membrane [118–120]. This central binding site overlaps with the primary inhibitor binding site [121]. A secondary, allosteric inhibitor binding site is formed by the extracellular vestibule (EV) in the outward-open conformation, which modulates transporter activity by altering kinetics of ligand dissociation from the central site when occupied [121–123]. The N-terminal and C-terminal ends of the transporter are located on the cytoplasmic side and play an important role in SERT regulation through binding to several other proteins, e.g. Sec24C, nNOS, PKC, Hic-5 and syntaxin 1A [124,125]. A topology model of SERT is shown in Figure 1.5.

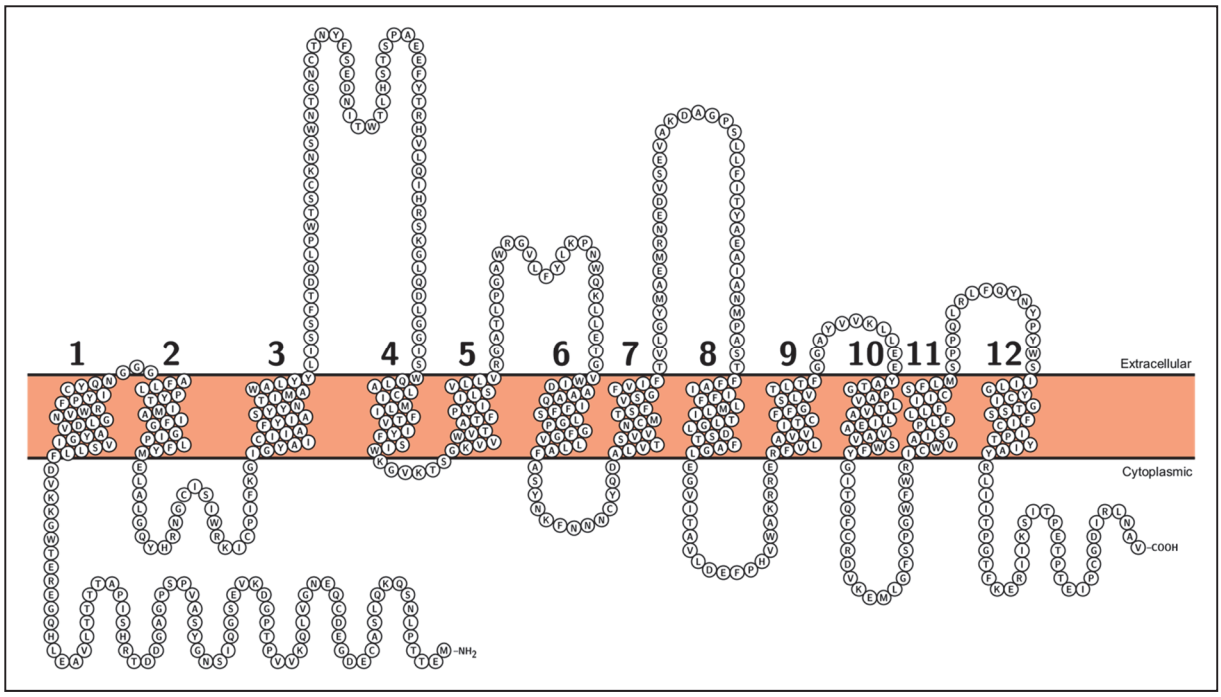

Figure 1.5: Topology model of SERT. Members of the monoamine transporter family have 12 transmembrane helices (TMs) with an inverted-topological repeat of TMs 1-5 and TMs 6-10. A central binding site for substrate and ions is located halfway across the membrane and a secondary, allosteric binding site is formed by the extracellular vestibule in the outward-open conformation. The N-terminal and C-terminal end is involved in SERT regulation. The topology model was created using Protter [126] based on the UniProt secondary structure annotation.

1.2.1.2 Transport mechanism

The underlying mechanism for substrate transport is explained by alternately exposing its binding site to the cytoplasmic and extracellular faces of the plasma membrane [127]. This requires the transporter to undergo conformational changes that closes access from one side and opens access to the other side. Furthermore, the induction of conformational change must be coupled to the occupancy of the transporter's binding sites. The proposed mechanism for 5-HT transport is shown in Figure 1.6 A. In its outward-open conformation, SERT binds Na^+, Cl^- and $HT\text{-}5^+$ in 1:1:1 stoichiometry. Only after binding all three substrates, SERT undergoes a conformational change that occludes the binding site from the extracellular space (outward-occluded) and exposes it to the cytoplasm (inward-open) [128]. After dissociation of Na^+, Cl^- and $5\text{-}HT^+$, a cytoplasmic K^+ ion binds to the transporter (inward-occluded) and it returns to the previous conformation (outward-open), where it releases K^+ to the extracellular space. The result of this process is an electroneutral exchange of K^+ with Na^+, Cl^- and $5\text{-}HT^+$ in 1:1:1:1 stoichiometry [129–131]. The Na^+/K^+ gradient across the membrane required for 5-HT transport is established by a Na+/K+-ATPase (Figure 1.6 B). Several pharmaceutical drugs as well as addictive drugs (e.g. cocaine; [132]) can bind to the transporter and inhibit the reuptake of 5-HT, thereby increasing extracellular 5-HT concentration. Furthermore, amphetamine and its derivatives (e.g. 3,4-methylenedioxymethamphetamine, MDMA) can reverse the transport direction resulting in an efflux of substrate [127,132–134].

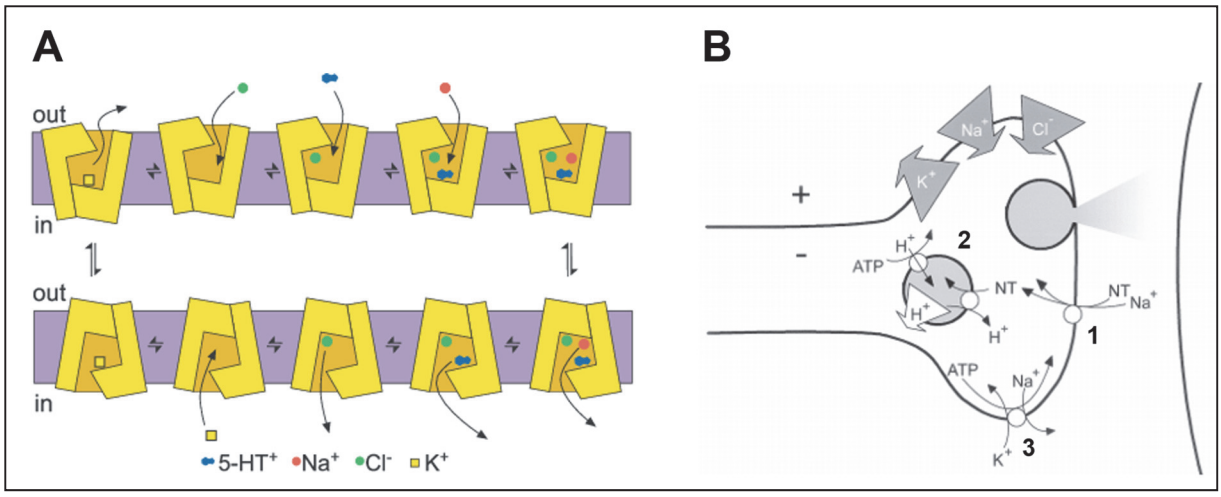

Figure 1.6: Proposed mechanism of serotonin transport. **(A)** Transport of 5-HT along with Na^+ and Cl^- requires binding of each substrate to the protein (upper middle). Only then is the transporter able to undergo a conformational change (right). In the inward-open conformation is the binding site exposed to the cytoplasm and substrates dissociate from the transporter (lower right). This allows a K^+ ion to bind (lower left), which induces a conformational change towards outward-open conformation (left). Dissociation of K^+ completes the cycle (Figure adapted from [127]). **(B)** After release, the transmitter (NT) is transported across the plasma membrane by a Na^+-dependent transporter in the plasma membrane (1). Transmitter delivered into the cytoplasm is further sequestered in synaptic vesicles by a vesicular transporter using the transmembrane H^+ gradient as a driving force (2). This driving force, shown by the arrow pointing in the direction of downhill H+ movement, is generated by an ATP-dependent H+ pump in the vesicle membrane. The Na+ and K+ gradients across the plasma membrane are generated by the Na+/K+-ATPase (3). This enzyme also creates a transmembrane electrical potential (negative inside) that causes Cl^- to redistribute. Neurotransmitter transport across the plasma membrane is coupled to the Na^+, Cl^-, and K^+ gradients and the membrane potential generated by the ATPase (Figure adapted from [133])

1.2.1.3 Binding sites

Initially, identification of inhibitor binding sites in mammalian MATs was based on site-directed mutagenesis experiments, but these experiments do not allow discrimination between direct and indirect effects of the mutations [135,136]. It is thought, that many of these mutations showed a change in inhibitor affinity due to allosteric rearrangements of the protein conformation rather than a direct interaction in the binding site [137–139]. The crystal structure of the leucine transporter (LeuT), a bacterial homologue of mammalian MATs, in complex with inhibitor molecules has been used as a model for binding site identification in SERT [140]. Recently published crystal structures of engineered thermostable (ts2; ts3) SERT in complex with inhibitors characterized the binding interactions of four different SSRIs (sertraline, fluvoxamine, paroxetine, S-citalopram) with SERT at the central binding site [118,141] as shown in Figure 1.7.

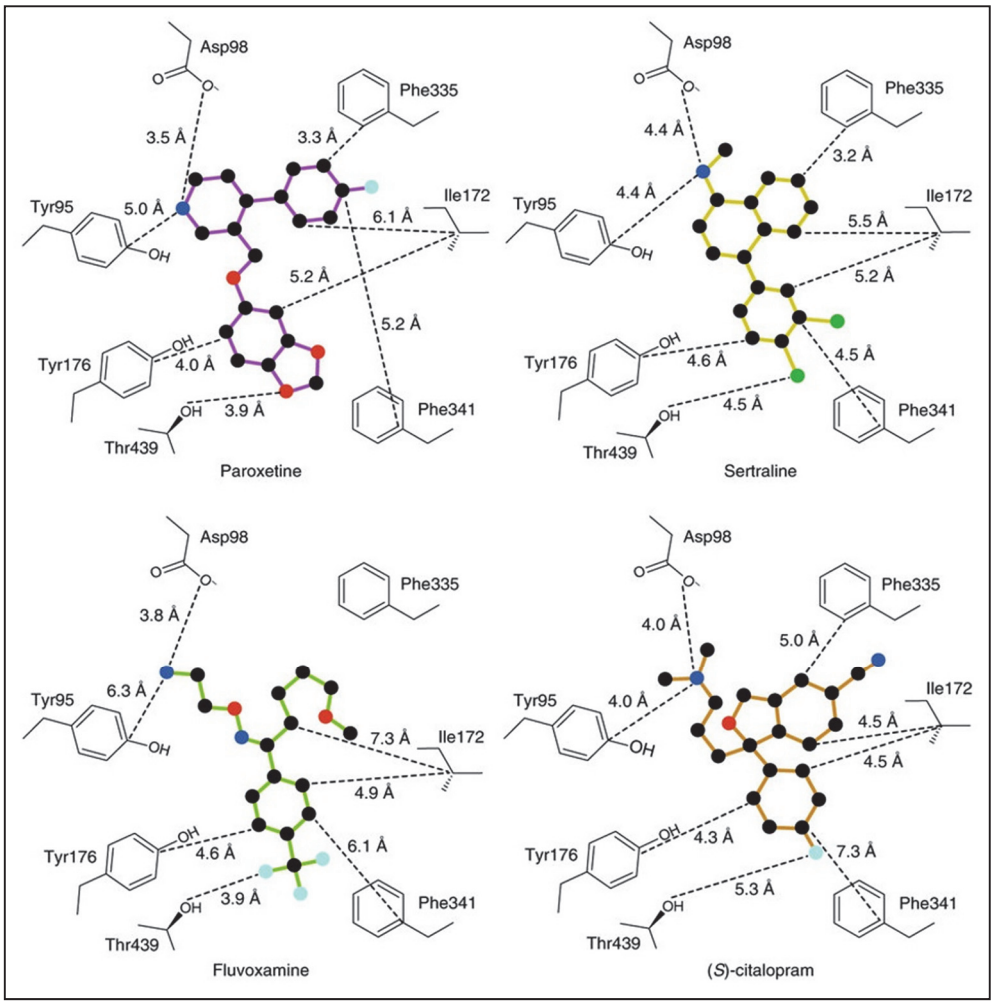

Figure 1.7: Binding interactions of SSRIs at the central binding site in SERT. Distances of each residue to various drug positions. **(A)** ts2-SERT:paroxetine **(B)** ts3-SERT:sertraline **(C)** ts3-SERT:fluvoxamine **(D)** ts3-SERT:(*S*)-citalopram. Figure adapted from [141].

Access to the central binding (S1) site is regulated through an extracellular gate, located at the base of the EV, and an intracellular gate near the cytoplasmic face. In the outward-open conformation, the aromatic side chain residues Tyr176 and Phe335, that are forming the lower portion of the extracellular gate are 10 Å apart, thus providing a pathway for substrates, inhibitors and ions to reach the central binding site. The intracellular gate is closed in this conformation, precluding direct access from the central binding site to the cytoplasmic space. The S1 site is formed by polar, aromatic and aliphatic side chain residues located in TM1, TM3, TM6 and TM8 (Figure 1.8). This binding site can be further divided into three subsites: subsite A is formed by residues Tyr95, Asp98, Ser336; subsite B contains the residues Ala169, Ile172, Ala173, Tyr176, Phe341, Ser439, Leu443; binding interaction in subsite C is mediated by Phe335, Thr497, Val501. The inhibitory effect of sertraline, fluvoxamine, paroxetine and S-citalopram is mediated through competitive binding to the primary site, which stabilizes the outward-open conformation. Occupancy of the primary site, which overlaps with the substrate binding site (except for Leu443, Thr497, Val501), permits substrate binding [142,143]. In

contrast to sertraline and fluvoxamine, (*S*)-citalopram was also found in the allosteric binding (S2) site [118].

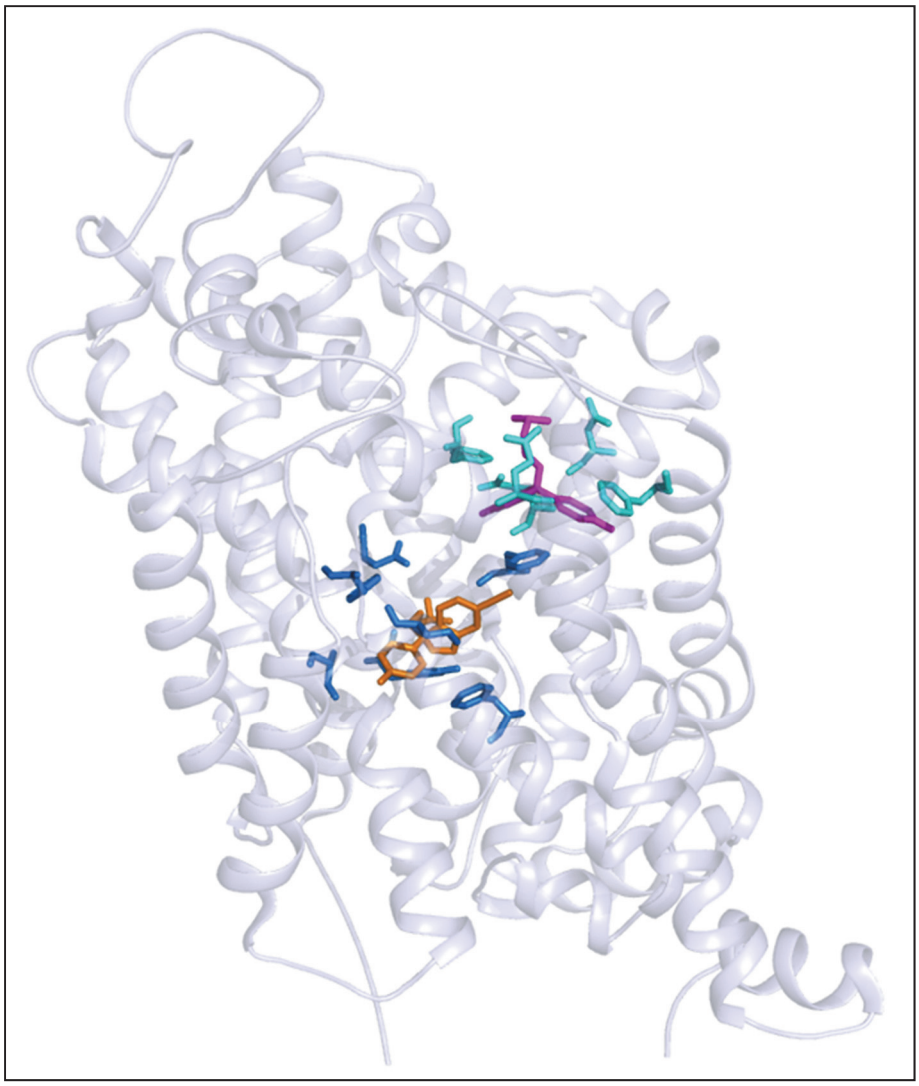

Figure 1.8: Structure of inhibitor bound hSERT. Cartoon representation of hSERT (PDB: 5I73), S-citalopram located at the central (orange) and allosteric (magenta) binding site of hSERT is shown as sticks. Residues interacting with the bound inhibitor at the central (blue) and allosteric (cyan) site are shown as sticks.

A putative second substrate binding (S2) site has been identified in LeuT, DAT, NET and SERT [144]. While it has been implicated in binding, its role in the substrate transport process remains unclear. For DAT it was proposed that binding to the S2 site triggers the release of substrate and sodium ions from the S1 site through an allosteric interaction [145,146]. Furthermore, an allosteric relationship between S1 and S2 sites in presence of inhibitor has been demonstrated for SERT [122,147]. The low-affinity S2 site in SERT can bind to detergent as well as inhibitor molecules, but structural evidence of substrate bound to the S2 site remains to be presented.

Initially it was shown that presence of unlabeled 5-HT reduces the dissociation rate of [^{3}H]imipramine, thereby suggesting an allosteric modulation. Further experiments showed that the dissociation rate of [^{3}H](*S*)-citalopram from the central binding site is reduced in presence of unlabeled SSRIs (*S*)-citalopram, (*R*)-citalopram, sertraline, paroxetine and 5-HT in a concentration dependent manner [121]. A similar effect could be observed for the TCAs imipramine and clomipramine [122]. The relative allosteric effect of (*S*)-citalopram depends on the ligand bound at the central site [148]. Furthermore, it was found that (*R*)-citalopram reduces the association rate of (*S*)-citalopram while minimally affecting maximum binding [149–151]. The allosteric site is located in the permeation pathway above the central binding site and occupancy of the allosteric site can prevent association to and dissociation from the central binding site through steric hindrance, thereby reducing the respective rate constants. Although the allosteric effects of citalopram on hSERT have been extensively investigated [123,152,153], the exact mechanism of allosteric modulation remains unclear.

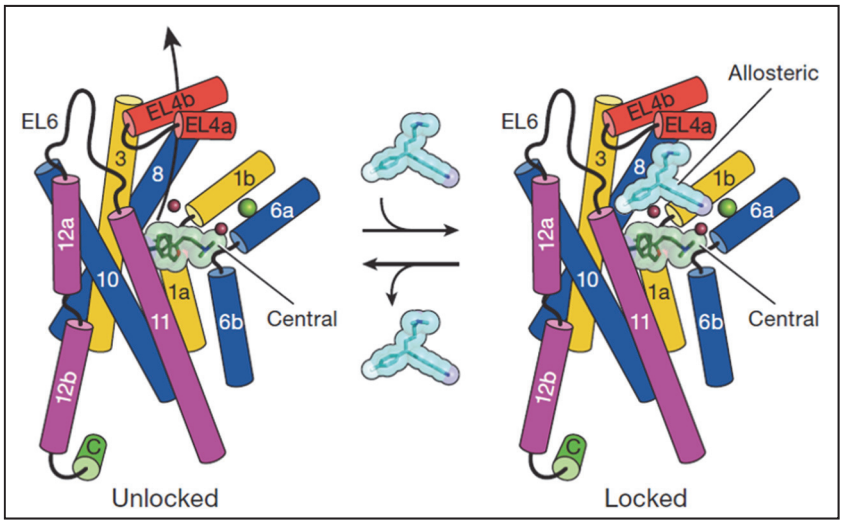

Figure 1.9: Allosteric modulation of inhibitor binding. Occupancy of the allosteric site with S-citalopram locks the SERT in its outward-open confirmation and impairs dissociation of S-citalopram from the central binding site. Figure adapted from [118].

Previous experiments that compared the Na^+ dependence on 5-HT transport and imipramine binding in SERT suggested a 1:1 stoichiometry for the substrate transport process and a 2:1 stoichiometry for binding of imipramine [131]. Indeed, the crystal structure of SERT:inhibitor complexes revealed the presence of two Na^+ ions and one Cl^- ion. The Na^+ binding stoichiometry for LeuT is 2, but the stoichiometry for transport is unknown [127]. As there is no SERT:5-HT structure available, it remains unclear, whether binding and transport stoichiometry are always different. Binding of ions in SERT is coordinated by residues in TM1, TM6 and TM7 for Na1; TM1 and TM8 for Na2; TM2, TM6 and TM7 for Cl.

1.3 Aim of this study

The serotonin transporter is an important drug target for treatment of depression in humans. The aim of this study is to gain insight into structure-function relationships of SERT, especially regarding uptake inhibition. Three-dimensional structures of SERT:drug complexes including both TCAs and SSRIs are needed to understand the binding and inhibition mechanism, especially at the allosteric site, and to identify those residues, that are involved in inhibitor binding. Information about structural data may guide the development of new antidepressants, that are superior in terms of efficacy, onset and adverse effects compared to currently available pharmaceuticals, by structure-based drug design. X-ray diffraction of protein crystal allows to determine the structure with high resolution. However, this attempt requires a high amount of homogenous purified protein, and expression in bacterial system is much faster and less cost intensive compared to mammalian expression systems. Furthermore, previous experiments at ICS-6 demonstrated that *E. coli* expressed hSERT can be crystallized using CIMP method. Expression of hSERT using baculovirus/insect cell system as an alternative to the bacterial system should be analyzed. To achieve this aim, the following objectives were initially defined:

- **Optimization of hSERT expression in *E. coli* and analysis of Sf9 expressed hSERT**

  Recombinant expression of hSERT in *E. coli* was previously established at ICS-6. Expression of two different hSERT constructs in different bacterial strains was planned to be investigated to reveal further optimization potential. Expression of hSERT in Sf9 was planned to be analyzed.

- **Homogenous purification of hSERT**

  Biophysical experiments as well as crystallization trials require large quantities of homogenous purified protein. Detergent screening for optimal solubilization of target protein was planned. Furthermore, purification of hSERT constructs with different tags should be analyzed. The use of custom ligand resins for specific hSERT purification was planned to be analyzed.

- **Thermostabilization of hSERT**

  The influence of detergents, lipids and ligands on the thermostability of hSERT should be analyzed to identify those compounds, that can help stabilizing the protein during the crystallization process.

- **Biophysical characterization of inhibitor binding and substrate transport**

  Binding of inhibitor molecules to purified hSERT was planned to be investigated and compared to kinetic values obtained from mammalian expressed hSERT described in the scientific literature. Furthermore, development of a transport assay to measure 5-HT uptake *in vitro* was planned.

- **Crystallization of hSERT**

  Crystallization of hSERT using different techniques (CIMP, Bicelle, *in surfo*) and in combination with different inhibitors was planned. Reproduction of previously obtained hSERT crystal was considered to be of high importance.

2 Material and methods

2.1 Material

2.1.1 Devices

Device	Manufacturer
ÄKTA explorer 100	GE Healthcare, Munich
Axio Scope.A1	Carl Zeiss, Jena
Baker SterilGARD II	Baker, Sanford
ChemiDoc XRS	Bio-Rad, Munich
DuoFlow 10	Bio-Rad, Munich
EmulsiFlex-C3	Avestin, Mannheim
Heraeus Biofuge Stratos Highconic Rotor	Thermo Scientific, Dreieich
Innova 4200/4220	Eppendorf, Hamburg
IPP 500 Incubator	Memmert, Schwabach
Mini-PROTEAN Tetra Cell	Bio-Rad, Munich
Model 425 CD Spectrometer	Aviv Biomedical, Lakewood
Monolith NT.115	Nanotemper, Munich
mosquito LCP	TTP Labtech, Melbourn
Multitron Standard	Infors HT, Bottmingen
Optima XPN-90 Type 70 Ti Rotor	Beckmann Coulter, Krefeld
Sigma 1-14K	Sigma Laborzentrifugen, Osterode
Sorvall LYNX 6000 F9 6x1000 LEX Rotor T29 8x50 Rotor	Thermo Scientific, Dreieich
Spectrafuge Mini	Labnet, Woodbridge
Stemi 2000-C	Carl Zeiss, Jena
Sub-Cell GT	Bio-Rad, Munich
T100 Thermal Cycler	Bio-Rad, Munich
T80+ UV-VIS Spectrophotometer	PG Instruments, Lutterworth
Thermomixer R	Eppendorf, Hamburg
Trans-Blot Trubo	Bio-Rad, Munich

2.1.2 Kits and consumables

Scientific Kit	Manufacturer
Cubic Phase I + II, JCSG Core I – IV, JCSG+, MbClass, PACT	Qiagen, Hilden
Gelfiltration Calibration HMW Kit	GE Healthcare, Munich
GeneJET Gel Extraction Kit	Thermo Scientific, Dreieich
MemGold, MemGold2	Molecular Dimensions, Newmarket
QIAprep Spin Miniprep Kit	Qiagen, Hilden
RED-tris-NTA NT-647 Labeling Kit	NanoTemper, Munich

Consumable	Manufacturer
BlueElf Prestained Protein Marker	Jena Bioscience, Jena
GelRed	Biotium, Fremont
GeneRuler 1 lb DNA Ladder	Thermo Scientific, Dreieich
Glas Capillaries	NanoTemper, Munich
PD-10 Desalting Column	GE Healthcare, Munich
PureCube 100 Indigo Ni-Agarose	Cube Biotech, Monheim
PureCube Ni-NTA Agarose	Cube Biotech, Monheim
PVDF Membrane Amersham Hybond	GE Healthcare, Munich
Q Agarose	Cube Biotech, Monheim
Superdex 200 10/300 GL	GE Healthcare, Munich
Superdex 200 16/60 pg	GE Healthcare, Munich
TGX Stain-Free FastCast	Bio-Rad, Munich
Whatman Gel Blot Paper	GE Healthcare, Munich

2.1.3 Chemicals

Chemical	Manufacturer
1,10-Phenanthroline hydrochloride	Carl Roth, Karlsruhe
1,2-Dimyristoyl-sn-Glycero-3-Phosphocholine (DMPC)	Avanti Polar Lipids, Alabasta
1,4-Dithiothreitol	Carl Roth, Karlsruhe
1-Oleoyl-rac-glycerol (Monoolein)	Cube Biotech, Monheim
1-palmitoyl-2-oleoyl-sn-glycero-3-phospho-(1'-rac-glycerol) (POPG)	Avanti Polar Lipids, Alabasta
1-palmitoyl-2-oleoyl-sn-glycero-3-phosphocholine (POPC)	Avanti Polar Lipids, Alabasta
1-palmitoyl-2-oleoyl-sn-glycero-3-phosphoethanolamine (POPE)	Avanti Polar Lipids, Alabasta
2,2,2-Trichloroethanol (TCE)	Merck, Darmstadt
2,2-didecylpropane-1,3-bis-β-D-maltopyranoside (LMNG)	Anatrace, Maumee
2-[4-(2,4,4-trimethylpentan-2-yl)phenoxy]ethanol (Triton X-100)	AppliChem, Darmstadt
2-[4-(2-hydroxyethyl)piperazin-1-yl]ethanesulfonic acid (HEPES)	AppliChem, Darmstadt
2-Amino-2-(hydroxymethyl)propane-1,3-diol (TRIS)	Sigma-Aldrich, Darmstadt
2-Mercaptoethanol (ß-ME)	Sigma-Aldrich, Darmstadt
3-([3-Cholamidopropyl]dimethylammonio)-2-hydroxy-1-propanesulfonate (CHAPSO)	Sigma-Aldrich, Darmstadt
4-(2-Aminoethyl)benzenesulfonyl fluoride hydrochloride (AEBSF)	Carl Roth, Karlsruhe
4-[[(3S,8S,9S,10R,13R,14S,17R)-10,13-dimethyl-17-[(2R)-6-methylheptan-2-yl]-2,3,4,7,8,9,11,12,14,15,16,17-dodecahydro-1H-cyclopenta[a]phenanthren-3-yl]oxy]-4-oxobutanoic acid (CHS, Cholesteryl hemisuccinate)	Anatrace, Maumee
5-Amino-2,3-dihydro-1,4-phthalazinedione (Luminol)	Sigma-Aldrich, Darmstadt
6-aminohexanoic acid	Sigma-Aldrich, Darmstadt
6-Cyclohexylhexyl β-D-maltoside (Cy-6)	Glycon, Luckenwalde
7-diethylamino-3-(4′-maleimidylphenyl)-4-methylcoumarin) (CPM)	Biotium, Fremont
8-Anilino-1-naphthalenesulfonic acid (ANS)	Sigma-Aldrich, Darmstadt
Acrylamide 4K - Solution (30 %) - Mix 29:1	AppliChem, Darmstadt
Agar-Agar	Carl Roth, Karlsruhe
Agarose powder	Bio-Rad, Munich

Chemical	Manufacturer
Ampicllin sodium salt	AppliChem, Darmstadt
Benzamidine hydrochloride	Sigma-Aldrich, Darmstadt
Betaine	Sigma-Aldrich, Darmstadt
Brain Polar Lipid Extract	Avanti Polar Lipids, Alabasta
Chloramphenicol	AppliChem, Darmstadt
Citalopram hydrobromide	Sigma-Aldrich, Darmstadt
Desipramine hydrochloride	Sigma-Aldrich, Darmstadt
Fluoxetine hydrochloride	Sigma-Aldrich, Darmstadt
Imidazole	Carl Roth, Karlsruhe
Kanamycin sulfate	AppliChem, Darmstadt
L(+)-Rhamnose monohydrate	AppliChem, Darmstadt
Leupeptin hemisulfate	Carl Roth, Karlsruhe
N,N,N′,N′-Tetramethylethane-1,2-diamine (TEMED)	AppliChem, Darmstadt
N,N-Dimethyldodecylamine N-oxide (LDAO)	Anatrace, Maumee
N-[N-(L-3-trans-Carboxyoxiran-2-carbonyl)-leucyl]-agmatin (E-64)	Carl Roth, Karlsruhe
n-Decyl-ß-D-maltopyranoside (DM)	Glycon, Luckenwalde
n-Dodecyl-phosphocholine (FOS-12)	Cube Biotech, Monheim
n-Dodecyl-ß-D-maltoside (DDM)	Cube Biotech, Monheim
n-Hexadecyl-phosphocholine (FOS-16)	Cube Biotech, Monheim
n-Nonyl-ß-D-glucopyranoside (NG)	Glycon, Luckenwalde
n-Octyl-ß-D-glucopyranoside (OG)	Glycon, Luckenwalde
n-Octyl-β-D-thioglucoside (OTG)	Glycon, Luckenwalde
Nonfat dried milk powder	AppliChem, Darmstadt
n-Tetradecyl-phosphocholine (FOS-14)	Cube Biotech, Monheim
Paroxetine hydrochloride	Cayman Chemical, Ann Arbor
Pepstatin A	Carl Roth, Karlsruhe
Polyoxyethylene (20) sorbitan monolaurate (Tween 20)	AppliChem, Darmstadt
Serotonin hydrochloride	abcr, Karlsruhe
Sodium dodecyl sulfate (SDS)	Carl Roth, Karlsruhe
Tryptone/Peptone ex casein	Carl Roth, Karlsruhe
Yeast extract	Carl Roth, Karlsruhe

All other chemicals were purchased from AppliChem.

2.1.4 Biological material

2.1.4.1 Organisms

Table 2.1: Bacterial and insect cell strains.

Strain	Genotype	Origin/Reference
Escherichia coli Top10	F - mcrA Δ(mrr-hsdRMS-mcrBC) φ80lacZΔM15 ΔlacX74 recA1 araD139 Δ(araleu)7697 galU galK rpsL (StrR) endA1 nupG	Invitrogen, Carlsbad
Escherichia coli OverExpress C43(DE3)	F^- ompT gal dcm $hsdS_B(r_B^- m_B^-)$ (DE3)	Lucigen, Middleton
Escherichia coli BL21(DE3) RP	E. coli B F– ompT hsdS(rB - mB -) dcm+ Tetr gal λ(DE3) endA Hte [argU proL CamR]	Stratagene, San Diego
Escherichia coli Lemo21	fhuA2 [lon] ompT gal (λ DE3) [dcm] ΔhsdS/ pLemo(CamR) λ DE3 = λ sBamHIo ΔEcoRI-B int::(lacI::PlacUV5::T7 gene1) i21 Δnin5 pLemo = pACYC184-PrhaBAD-lysY	New England Biolabs, Ipswich
Spodoptera frugiperda IPLB-SF-9AE		Oxford Expression Technologies, Oxford

2.1.4.2 Plasmids and constructs

Table 2.2: Bacterial plasmids.

Name	Antibiotic resistance	Promoter	Expression system	Origin/Reference
pQE-2	Ampicillin	T7	Bacteria	Qiagen, Hilden
pET-20b	Kanamycin	T7	Bacteria	Merck, Darmstadt
pOET-2	Ampicillin	Polyhedrin	Insect	Oxford Expression Technologies, Oxford
pOET-4	Ampicillin	p6.9	Insect	Oxford Expression Technologies, Oxford

Table 2.3: Expression constructs.

Construct	Affinity tag	Plasmid	Expression system	Restriction sites	Origin/Reference
His-hSERT	N-terminal His8-tag (HHHHHHHH)	pQE-2	Bacteria	unknown	ICS-6, Jülich
Rho-hSERT	C-terminal Rho-tag (TETSQVAPA)	pET-20b	Bacteria	unknown	Cube Biotech, Monheim
p2bv-hSERT	C-terminal Rho-tag (TETSQVAPA)	pOET-2	Insect	XhoI/BamHI	Own work
p4bv-hSERT	C-terminal Rho-tag (TETSQVAPA)	pOET-4	Insect	XhoI/BamHI	Cube Biotech, Monheim
p2bv-hCNX	N-terminal His_8-tag (HHHHHHHH)	pOET-2	Insect	EcoRI/BamHI	GeneArt / own work
p4bv-hCNX	N-terminal His_8-tag (HHHHHHHH)	pOET-4	Insect	EcoRI/BamHI	GeneArt / own work

Designing of constructs p2-hSERT, p2-hCNX and p4-hCNX was done using the software ‘Genome Compiler’ [154].

2.1.4.3 Antibodies

Table 2.4: Antibodies used for immunodetection.

Antibody	Description	Suppplier
α-Penta-His	Mouse monoclonal against Penta-His epitope; HRP conjugated working dilution: 1:10,000	Qiagen, Hilden
α-Rho1D4	Mouse monoclonal against Rho1D4 epitope; working dilution: 1:5,000	Cube Biotech, Monheim
Goat α-mouse HRP conjugate	Secondary antibody against mouse; HRP conjugated working dilution: 1:5,000	Sigma-Aldrich, Darmstadt

2.1.5 Media

All prepared media was autoclaved before use. Preparation of complex auto-induction medium was done according to a published method [155]. Serum-free medium for insect cell culture was purchased from Lonza, Basel (Insect-XPRESS).

Table 2.5: Composition of bacterial culture medium.

Component	ZY	LB (pH 7.4)	TB	SOB
Tryptone	16 g/L	10 g/L	12 g/L	20 g/L
Yeast extract	10 g/L	5 g/L	24 g/L	5 g/L
NaCl	5 g/L	10 g/L	-	0.6 g/L
Agar	-	-	15 g/L	-
Glycerol	-	-	4 g/L	-
K_2HPO_4	-	-	72 mM	-
KH_2PO_4	-	-	17 mM	-
KCl	-	-	-	2.5 mM
$MgCl_2$	-	-	-	10 mM
$MgSO_4$	-	-	-	10 mM

Table 2.6: Composition of complex auto-induction medium for bacterial culture.

Component	Volume	Composition	Final concentration
ZY medium	928 mL	Tryptone	1 % (w/v)
		Yeast extract	0.5 % (w/v)
20x NPS	50 mL	Na_2HPO_4	50 mM
		KH_2PO_4	50 mM
		$(NH_4)_2SO_4$	25 mM
50x 5052	20 mL	Glycerol	0.5 % (w/v)
		Glucose	0.05 % (w/v)
		α-Lactose	0.2 % (w/v)
1 M MgSO4	2 mL	$MgSO_4$	2 mM
1000x trace elements	0.2 mL	$FeCl_3$	50 mM
		$CaCl_2$	20 mM
		$MnCl_2$	10 mM
		$ZnSO_4$	10 mM
		$CoCl_2$	2 mM
		$CuCl_2$	2 mM
		$NiCl_2$	2 mM

2.2 Methods

2.2.1 Microbiological methods

2.2.1.1 Bacterial cell culture

2.2.1.1.1 Preparation of chemical competent cells

For preparation of chemical competent *Escherichia coli* (*E. coli*) cells 200 mL SOB medium (Table 2.5) was inoculated at a ratio of 1:100 with 2 mL of an overnight grown starter culture [156,157]. Cells were grown at 30 °C and 120 rpm until OD_{600} ~0,3 was reached. Cells were kept on ice for 15 min and centrifuged at 5,000 rpm at 4 °C for 15 min. The pellet was gently resuspended in 1/5 of culture volume in ice cold TBF-1 buffer (30 mM NaAc pH 6.0; 50 mM $MgCl_2$; 100 mM NaCl; 10 mM $CaCl_2$; 15 % (w/v) Glycerol) and incubated for 15 min on ice. The resuspended cells were centrifuged at 5.000 rpm at 4 °C for 15 min. The pellet was gently resuspended in 1/25 of culture volume in ice cold TBF-2 buffer (10 mM MOPS pH 7.0; 75 mM $CaCl_2$; 10 Mm NaCl; 15 % (w/v) Glycerol) and kept on ice for 15 min. The resuspended cells were distributed in 100 µL aliquots in 1.5 mL reaction tubes, flash frozen with LN_2 and kept at -80 °C for long term storage.

2.2.1.1.2 Transformation of chemical competent cells

The transformation of *E. coli* cells was done according to a published method [158]. An aliquot (100 µL) of chemical competent cells of the desired *E. coli* strain and plasmid DNA of the desired construct was thawed on ice. Cells were incubated with 15 ng of plasmid DNA on ice for 30 min. Cells were treated with a heat shock at 42 °C for 90 sec., followed by a cooling step on ice for 2 min. The transformation reaction was supplemented with 500 µL fresh LB medium (Table 2.5) and incubated for 30-60 min at 37 °C and 750 rpm. Cells were sedimented at 12,000 × g for 1 min, resuspendend in 100 µL supernatant, plated onto LB agar plates [159] and grown under antibiotic selection at 30 °C for 18 h.

2.2.1.1.3 Overexpression of hSERT in *Escherichia coli*

An overnight grown starter culture of C-Rho-hSERT in *E. coli* C43 (DE3) was used to inoculate TB medium (Table 2.5) to an OD_{600} of ~0.04. Cells were grown at 37 °C and 100 rpm in a medium volume of 1/10 of the total flask volume. Protein overexpression was induced by adding 0.4 mM IPTG after the cells reached and OD_{600} of ~0.6 – 0.8 and the temperature was set to 18 °C. Cells were harvested at 5,000 rpm for 15 min at 4 °C after 16 h of expression.

Overexpression of N-His_8-hSERT in *E. coli* BL21 (DE3) RP was done using complex auto-induction medium (CAIM). ZY based CAIM (Table 2.6) was inoculated with an overnight grown

starter culture to an OD_{600} of ~0,02. Cells were grown at 37 °C and 100 rpm in a medium volume of 1/10 of the total flask volume. The temperature was decreased to 18 °C after 2 h and cells were harvested at 5000 rpm for 15 min at 4 °C after another 22 h.

Overnight starter cultures were grown in the presence of 2 % (w/v) Glucose to suppress basal transcription. Antibiotics were used for growth selection at the following final concentrations: Kanamycin 50 µg mL^{-1}; Ampicillin 100 µg mL^{-1}; Chloarmphenicol 25 µg mL^{-1}.

2.2.1.2 Insect cell culture

2.2.1.2.1 Establishment and maintenance of *Spodoptera frugiperda*

Initially, cells from *Spodoptera frugiperda* IPLB-SF9-AE (Sf9) were seeded as adherent culture in T75 flasks at a density of 0.5 × 10^6 cells mL^{-1} in 10 mL serum-free medium (Insect-XPRESS; Lonza, Basel) and incubated at 28 °C. Cells were dislodged from the surface through mechanical force on the outside of the T75 flask. Cells were passaged with fresh medium in a dilution ratio of 1:4 or 1:5 when the culture reached ~90 % confluency. After two to three rounds of passaging, cells were transferred to a 500 mL suspension flask and seeded at a density of 0.5 × 10^6 cells mL^{-1} in a medium volume of 1/5 of the total flask volume. The culture was incubated at 28 °C and 225 rpm. Cells in suspension culture were passaged after reaching a density of 3-6 × 10^6 cells mL^{-1}. Cells were counted using a hemocytometer after mixing equal volumes of culture sample and Trypan blue. All cells were handled under aseptic conditions.

2.2.1.2.2 Cotransfection and viral replication

Cells from Sf9 culture with a minimum of 95 % viability were seeded at a density of 0.5 × 10^6 cells mL^{-1} in 2 mL serum-free medium (Insect-XPRESS; Lonza, Basel) per well in a 6-well plate and incubated at 28 °C for 1 h. After cells attached to the surface, 1 mL of medium was removed and the cotransfection mix (100 µL serum-free medium; 5 µL flashBAC virus DNA (OET, Oxford); 500 ng transfer vector containing insert (OET, Oxford); 10 µL Insect GeneJuice (Merck, Darmstadt) was added. Cells were incubated at 28 °C and 1 mL of serum-free medium was added after 16 h. After five days of incubation, the supernatant was removed from each well and stored in the dark at 4 °C as P0 virus stock. To achieve a higher concentration of virus particles, 0.5 mL of P0 virus stock was added to 100 mL Sf9 suspension culture. Cells were incubated at 28 °C and 225 rpm in a 500 mL suspension flask for three to five days. The suspension was centrifuged at 3,000 rpm for 15 min. and the clarified supernatant was stored in the dark at 4 °C as working P1 virus stock.

2.2.2 Biochemical methods

2.2.2.1 Molecular cloning

2.2.2.1.1 Plasmid DNA amplification and isolation from *Escherichia coli*

Escherichia coli Top10 cells were transformed with the desired plasmid DNA (2.2.1.1.2). A single colony was picked and used to inoculate 5 mL LB medium (Table 2.5). Cells were grown overnight at 37 °C and 120 rpm. Isolation of plasmid DNA from *E. coli* is based on alkaline lysis [160] and was done with MiniPrep Kit (Qiagen, Hilden) according to manufacturer's manual.

2.2.2.1.2 Restriction digestion of DNA

The coding sequence for the target protein (insert) was released from its cloning vector using appropriate endonuclease restriction enzymes. Linearization of the transfer vector was done using the same combination of restriction enzymes. The reaction setup for restriction digestion is shown in Table 2.11. Samples were incubated for 5 min at 37 °C, followed by an incubation step of 5 min at 80 °C to deactivate restriction enzymes and avoid unspecific restriction activity. The samples were then subjected to agarose gel electrophoresis (2.2.2.1.4) to separate digested from undigested DNA. Extraction and purification of the digested DNA was done using GeneJet Gel Extraction Kit (Thermo Scientific, Dreieich) according to manufacturer's manual.

Table 2.7: Reaction mix for restriction digestion of DNA

Component	Volume
10x FastDigest Green buffer	2 µL
FastDigest Restriction enzyme	1 µL (each)
FastAP alkaline phosphatase	1 µL
Plasmid DNA	2 µL (up to 1 µg)
H2O (nuclease-free)	ad 20 µL

2.2.2.1.3 Ligation of DNA

The purified insert was ligated with the linearized transfer vector using T4 DNA Ligase. The reaction setup is shown in Table 2.12. Samples were incubated for 10 min at 22 °C. An aliquot of 5-10 µL of the ligation mix was used for transformation into *E. coli* Top10 (2.2.1.1.2).

Table 2.8: Reaction mix for ligation of DNA

Component	Volume or amount
Linearized vector DNA	100 ng
Insert DNA	1:1 to 5:1 molar ratio over vector
10x T4 DNA Ligase buffer	2 µL
T4 DNA Ligase	0.2 µL
H_2O (nuclease-free)	ad 20 µL

2.2.2.1.4 Agarose gel electrophoresis

Agarose gel electrophoresis is a method to separate DNA fragments according to their seize. The sample containing different DNA species will be loaded onto an agarose gel, that contains buffer filled pores. The pore size is determined by the concentration of agarose molecules, i.e. a higher concentration of agarose will result in a smaller pore size. After applying an electrical current, the negatively charged DNA molecules will migrate through the gel pores towards the anode. Smaller DNA molecules migrate faster through the pores than larger molecules, which will result in a size-based separation of DNA molecules.

Samples were loaded onto a 1 % (w/v) agarose gel prepared in TAE-Buffer (40 mM TRIS, pH 8.0; 40 mM AcOH; 1 mM EDTA). A constant voltage of 120 V was set for 1-1.5 h. GeneRuler 1 kb DNA Ladder (Thermo Scientific, Dreieich) was loaded in a well next to the sample wells to estimate the size of DNA fragments. The DNA was stained with GelRed (Biotium, Fremont) and images were captured with ChemiDoc XRS (Bio-Rad, Munich) after excitation with UV light. Separated DNA bands were purified using GeneJET Gel Extraction Kit (Thermo Scientific, Dreieich).

2.2.1.1.5 Spectroscopic DNA quantification

The concentration estimation of a nucleic acid solution was done by measuring the absorption of a sample at 260 nm. Concentration c of nucleic acid was calculated using Lambert-Beers law (equation 1):

$$\mathrm{c} = \frac{A_{260}}{\varepsilon_{260} \times d} \qquad (1)$$

with A_{260nm} as absorption of sample at 260nm, ε_{260nm} as sepcific extinction coefficient (50 L mol^{-1} cm^{-1}) und d as path length (1 cm).

2.2.1.1.6 Sequencing of isolated plasmid DNA

Sequencing of plasmid DNA was done at Seqlab, Göttingen.

2.2.2.2 Purification of hSERT

All buffers used throughout the purification (Table 2.9) were filtered and degassed before use.

Table 2.9: Purification buffers

Name	Composition
Sucrose buffer	50 mM HEPES pH 7.9; 20 % (w/v) Sucrose; 1 mM EDTA
Lysis buffer	20 mM TRIS pH 7.5; 150 mM NaCl; 10 % (w/v) Glycerol; 2 mM MgCl2; 10 µM E-64; 1 µM Pepstatin A; 10 µM Leupeptin; 1 mM Pefabloc SC; 2 mM Benzamidine; 2 mM β-ME; 1 mg mL^{-1} Lysozyme; 30 U mL^{-1} DNAse I
Membrane suspension buffer	20 mM TRIS pH 7.5; 500 mM NaCl; 30 % (w/v) Glycerol; 0.5 mM TCEP; 10 µM E-64; 1 µM Pepstatin A; 10 µM Leupeptin; 1 mM Pefabloc SC; 2 mM Benzamidine
Solubilization buffer	20 mM TRIS pH 7.5; 500 mM NaCl; 10 % (w/v) Glycerol; 0.5 mM TCEP; 1 % (w/v) Fos-choline 12; 10 mM EDTA; 10 µM E-64; 1 µM Pepstatin A; 10 µM Leupeptin; 1 mM Pefabloc SC; 2 mM Benzamidine
NTA Wash Buffer I	20 mM TRIS; 150 mM NaCl; 10 % (w/v) Glycerol; 0.5 mM TCEP; 1 % (w/v) Fos-choline 12; 5 mM Imidazole; 1 µM E-64; 1 µM Leupeptin; 1 µM Pepstatin A; 1 mM Pefabloc SC; 1 mM Benzamidine; 10 mM EDTA
NTA Wash Buffer II	20 mM TRIS; 150 mM NaCl; 10 % (w/v) Glycerol; 0.5 mM TCEP; 0.1 % (w/v) Fos-choline 12; 10 mM Imidazole; 1 µM E-64; 1 µM Leupeptin; 1 µM Pepstatin A; 1 mM Pefabloc SC; 1 mM Benzamidine; 10 mM EDTA
NTA Wash Buffer III	20 mM TRIS; 150 mM NaCl; 10 % (w/v) Glycerol; 0.5 mM TCEP; 0.1 % (w/v) Fos-choline 12; 25 mM Imidazole; 1 µM E-64; 1 µM Leupeptin; 1 µM Pepstatin A; 1 mM Pefabloc SC; 1 mM Benzamidine; 10 mM EDTA
NTA Elution Buffer	20 mM TRIS; 150 mM NaCl; 10 % (w/v) Glycerol; 0.5 mM TCEP; 0.1 % (w/v) Fos-choline 12; 250 mM Imidazole; 1 µM E-64; 1 µM Leupeptin; 1 µM Pepstatin A; 1 mM Pefabloc SC; 1 mM Benzamidine; 10 mM EDTA
Rho Wash Buffer I	20 mM TRIS pH 7.5; 500 mM NaCl; 10 % (w/v) Glycerol; 0.5 mM TCEP; 0.1 % (w/v) Fos-choline 12
Rho Wash Buffer II	20 mM TRIS pH 7.5; 150 mM NaCl; 10 % (w/v) Glycerol; 0.5 mM TCEP; 0.1 % (w/v) Fos-choline 12
Rho Elution Buffer	20 mM TRIS pH 7.5; 150 mM NaCl; 10 % (w/v) Glycerol; 0.5 mM TCEP; 0.1 % (w/v) Fos-choline 12; 200 µM Rho peptide
IEC dilution buffer	20 mM TRIS pH 7.5; 10 % (w/v) Glycerol; 0.1 % (w/v) Fos-choline 12
IEC Low Salt buffer	20 mM TRIS pH 7.5; 25 mM NaCl; 10 % (w/v) Glycerol; 0.1 % (w/v) Fos-choline 12
IEC High Salt buffer	20 mM TRIS pH 7.5; 500 mM NaCl; 10 % (w/v) Glycerol; 0.1 % (w/v) Fos-choline 12
SEC buffer	20 mM TRIS pH 7.5; 150 mM NaCl; 10 % (w/v) Glycerol; 0.5 mM TCEP; 0.1 % (w/v) Fos-choline 12

2.2.2.2.1 Preparation of *Escherichia coli* membrane fraction

Cells were thawed on ice, resuspended in 5 mL ice cold resuspension buffer (Table 2.9) per gram cells and kept at 4 °C for 10 min under gentle stirring. The cells were sedimented at 7,000 × g, 4 °C for 40 min. The cell pellet was resuspended in 5 mM $MgSO_4$ and kept at 4 °C for 10 min under gentle stirring. The resuspended cells were sedimented at 4,500 × g, 4 °C for 20 min to remove the periplasmic fraction [161]. The collected cells were then resuspended in 8 mL ice cold Lysis buffer per gram cells and homogenized with 10-15 strokes in a glass homogenizer. Cells were kept at 4 °C for 1 h under constant stirring. Cells were passed 8-10 times through a cell disruptor (EmulsiFlex-C3) at 15-20,000 bar. The lysate was sedimented at 10,000 × g, 4 °C for 40 min to remove cell debris and inclusion bodies. The remaining supernatant was centrifuged at 267,000 × g, 4 °C for 1 h. The resulting pellet was collected, resuspended in membrane suspension buffer, and homogenized. After determination of total membrane protein concentration with Bradford assay (2.2.2.4.1), the membrane suspension was aliquoted in 1 mL aliquots into 2 mL reaction tubes, flash frozen with LN_2 and stored at -80 °C.

2.2.2.2.2 Solubilisation of *Escherichia coli* membrane fraction

Membrane aliquots were unfrozen on ice and diluted into Solubilisation buffer (Table 2.9) to a total protein concentration of 1-4 mg mL^{-1}. The membrane suspension was kept in the cold room at 4 °C under slow and constant stirring. The resulting supernatant after ultracentrifugation (267,000 × g, 4 °C, 1 h) was passed through a filter (0.2 µm) and immediately used for further purification.

2.2.2.2.3 Affinity chromatography

Affinity chromatography purification is based on a non-covalent binding of an analyte to a ligand, which is covalently linked to a stationary phase. This allows the removal of impurities through washing of the stationary phase. The analyte can then be displaced from the ligand by adding a molecule in high concentrations that competes with the analyte over ligand binding. In this present work, two different affinity chromatography matrices have been used routinely. Purification of his-tagged hSERT was done using immobilized metal ion affinity chromatography (IMAC). This method uses nitrilotriacetic acid (NTA) as a chelating agent, that is bound through a linker to an agarose matrix. It will form a complex with Ni^{2+} ions through four coordination positions. The remaining two coordination positions of the Ni^{2+} ion can than interact with the polyhistidine sequence of the target protein. High concentration of imidazole

can displace the His-tagged protein from the Ni^{2+} ion and is used for elution of the target protein. Purification of rho-tagged hSERT was done using rho1D4-antibody immobilized on an agarose matrix [162]. This antibody specifically binds to the amino acid sequence TETSQVAPA, which is fused to the C-terminal end of hSERT. Elution of the target protein is mediated through adding an excess of rho1D4 peptide that competitively binds to the antibody.

For his-tagged hSERT, the supernatant after solubilization (2.2.2.2.2) was incubated for 2 h at 4 °C with 1-5 mL PureCube Ni-NTA (Cube Biotech, Monheim) under slow and constant stirring in batch mode. The protein bound matrix was poured into an empty chromatography column (Bio-Rad, Munich) and the flow through was collected. The resin was washed with 10 CV Wash buffer I, 10 CV Wash buffer II and 10 CV Wash buffer III (Table 2.9) to remove unbound and unspecific bound proteins. Finally, bound target protein was eluted with 8x 1 CV Elution buffer containing 250 mM Imidazole. Elution fractions were either flash frozen with LN_2 and stored at -80 °C or immediately pooled and diluted in a 1:5 ratio with IEC dilution buffer and further purified with IEC (2.2.2.2.4).

For rho-tagged hSERT, the supernatant after solubilization (2.2.2.2.2) was incubated overnight at 4 °C with 1-2 mL PureCube Rho1D4 agarose (Cube Biotech, Monheim) under slow and constant stirring in batch mode. The protein bound matrix was poured into an empty chromatography column (Bio-Rad, Munich) and the flow through was collected. The resin was washed with 10 CV Rho Wash buffer I and 10 CV Rho Wash buffer II (Table 2.9) to remove unbound and unspecific bound proteins. Finally, bound target protein was eluted by incubating the Rho1D4 agarose for 1 h at 4 °C with 1 CV Elution buffer containing 200 µM rho peptide. The elution step was repeated five more times. Elution fractions were either flash frozen with LN_2 and stored at -80 °C or immediately pooled, concentrated by ultrafiltration (50 kDa MWCO; Amicon Ultra, Merck Milipore, Darmstadt) and further purified with SEC (2.2.2.2.5).

2.2.2.2.4 Ion exchange chromatography

The principle of ion exchange chromatography (IEC) is based on electrostatic attraction between the analyte and the stationary phase, which contains charged ionizable functional groups. These functional groups can interact and bind analyte ions of opposite charge. Elution of the analyte can be achieved through changing the pH and thereby altering the binding properties or through increasing the concentration of counterions that compete with the analyte over binding to the functional group of the stationary phase. Based on the charge of the functional groups, IEC can be further divided into cationic (positive charged group) and anionic (negative charged group) exchange chromatography.

Elution fractions after IMAC (2.2.2.2.3) were pooled and diluted in a 1:5 ratio with IEC dilution buffer (Table 2.9) to decrease concentration of NaCl and imidazole to 25 mM and 42

mM, respectively. The sample was loaded onto a manually packed 5 mL PureCube Q Agarose column (Cube Biotech, Monheim) with a flow rate of 0.3 mL/min at a DuoFlow 10 (Bio-Rad, Munich) FPLC system at 4 °C. The matrix was washed with 10 CV of IEC Low Salt buffer to remove unspecifically bound protein. Elution was carried out with a step gradient from 25–500 mM NaCl in steps of 1 % per 2 CV, which equals to an increase of 4.75 mM NaCl per step. Fractions that eluted from the resin at ~80 mM NaCl were pooled and concentrated by ultrafiltration (50 kDa MWCO; Amicon Ultra, Merck Milipore, Darmstadt). The concentrated sample was filtered to remove aggregated protein and then further purified through SEC (2.2.2.2.5)

2.2.2.2.5 Size-exclusion chromatography

Gel filtration is a technique to separate a mixture of proteins according to their size under non-denaturing conditions. It is based on the principles of size-exclusion chromatography (SEC). The stationary phase is a gel matrix with a defined pore size. Molecules in the liquid phase migrate through the gel matrix, where smaller molecules will diffuse into the pores and be retained until they diffuse out of the pores. Larger molecules cannot enter the pores and migrate faster through the gel matrix.

Size-exclusion chromatography was done using either ÄKTA explorer 100 (GE Healthcare, Munich) or DuoFlow 10 (Bio-Rad, Munich) FPLC system at 4 °C. The target protein was subjected to Superdex 200 10/300 GL for analytical scale or Superdex 200 16/60 pg (both GE Healthcare, Munich) for preparative scale purification. Samples were concentrated to a volume that corresponds to ~1 % of the respective CV. Column was preequilibrated with 2 CV SEC buffer (Table 2.9). The flow rate was set to 0.2 mL/min with a fraction size of 0.5 mL. Calibration of SEC columns was done using Gel Filtration Calibration Kit HMW (GE Healthcare, Munich).

2.2.2.3 Protein reconstitution

A lipid bilayer is important for membrane proteins to retain their native structure and function. Reconstitution of membrane proteins into an artificial lipid bilayer environment allows the protein to be assayed *in vitro* under close-to-native conditions without the presence of detergents, that can destabilize the membrane protein. Phospholipid vesicles (liposomes) form a self-closed lipid bilayer into which the membrane protein is incorporated [163]. Pre-formed, detergent-destabilized liposomes are mixed with the detergent-purified membrane and incubated. Incorporation of the membrane protein and formation of closed liposomes can be initiated through detergent removal.

2.2.2.3.1 Reconstitution of hSERT into liposomes

The method described by Geertsma et al [164] was modified for reconstitution of FC12 purified hSERT into liposomes. Lipids (1-palmitoyl-2-oleoyl-sn-glycero-3-phospho-(1'-rac-glycerol) (POPG); 1-palmitoyl-2-oleoyl-sn-glycero-3-phosphocholine (POPC); 1-palmitoyl-2-oleoyl-sn-glycero-3-phosphoethanolamine (POPE)) were dissolved in $CHCl_3$ and mixed in a 1:1:1 molar ratio (referred to as POPx) to a final amount of 50 mg. Organic solvent was evaporated using a gentle stream of nitrogen. The lipid film was dried overnight in a vacuum chamber. Dried lipids were suspended in Liposome buffer I (Table 2.10) to a final concentration of 20 mg mL^{-1} and sonicated to form small unilamellar vesicles. These were fused together to form large multilamellar vesicles through three cycles of flash-freezing in LN_2 and thawing at RT. The suspension was passed 11 times through a polycarbonate filter (30 or 100 nm) at 50 – 60 °C and diluted with Liposome buffer II to a final concentration of 4 mg mL^{-1}. Pre-formed liposomes were destabilized by adding stepwise 10 µL Liposome buffer III containing 1 % (w/v) FC-12 while monitoring the scattering at 540 nm. Addition of detergent was stopped after reaching saturation point R_{sat}. Destabilized liposomes and FC12 purified hSERT at a concentration of 1 mg mL^{-1} were combined at ratios from 1:20 to 1:400 and incubated at 4 °C for 1 h. Detergent was removed by six consecutive additions of 40 mg Bio-Beads SM-2 (Bio-Rad, Munich) per 1 mL of solution every 2 h. Bio-Beads were separated from the solution with an empty PD-10 column. Reconstituted hSERT was collected through ultracentrifugation (267,000 × g; 30 min; 4 °C) and resuspended in Liposome buffer III.

Table 2.10: Liposome reconstitution buffers

Name	Composition
Liposome buffer I	20 mM TRIS pH 7.4; 150 mM NaCl; 10 % (w/v) Glycerol; 0.5 mM TCEP
Liposome buffer II	20 mM TRIS pH 7.4; 150 mM NaCl; 0.5 mM TCEP
Liposome buffer III	20 mM TRIS pH 7.4; 150 mM NaCl; 2 % (w/v) Glycerol; 0.5 mM TCEP

2.2.2.4 Protein analytical methods

2.2.2.4.1 Spectroscopic protein quantification

A spectrum of a protein sample was measured within a range from 200 – 320 nm at a step size of 1 nm using 1 mL quartz micro cuvettes with a path length of 1 cm in a UV/VIS spectrophotometer. Concentration was calculated following Lambert-Beers law (equation 1):

$$c = \frac{A_{280nm}}{\varepsilon_{280nm} \times d} \quad (1)$$

with A_{280nm} as absorption of sample at 280 nm, ε_{280nm} as sepcific extinction coefficient (~71,400 L mol^{-1} cm^{-1} for hSERT) und d as path length (cm). The specific extinction coefficient and molecular weight (MW) for hSERT was estimated using the web service 'ProtParam' [165].

The photometric quantification of protein concentration according to Bradford [166] was done by adding 5 µL sample to 950 µL Bradford reagent (4.7 % (v/v) EtOH; 8.5 % (v/v) H_3PO_4; 0.01 % (w/v) Coomassie Brilliant Blue G-250) and 45 µL H_2O and incubating for 5 min at room temperature. Buffer without protein was used as a reference. The absorption at 595 nm was measured in 1 mL micro cuvettes using UV/VIS spectrophotometer. Bradford solution was calibrated with Lysozyme over a range from 0.2-1.6 mg mL^{-1}.

2.2.2.4.2 Polyacrylamide gel electrophoresis

Separation of proteins under denaturing conditions was done using SDS polyacrylamide gel electrophoresis (SDS-PAGE) according to Lämmli [167]. The 5x sample buffer (Table 2.12) contains a reducing agent (β-ME) and an anionic detergent (SDS), that disrupts the protein's tertiary structure and unfolds it into a linear molecule. SDS binds to the protein's surface thereby covering the protein's individual net charge with its own negative charge. The sample will be loaded to a polyacrylamide gel that contains pores of a defined size range, depending on the polyacrylamide concentration. When applying a current, the negatively charged protein molecules migrate through the gel matrix towards the anode. The migration speed depends on the protein molecule's size, with smaller proteins migrating faster than larger proteins. This method allows a separation of protein molecules based on their different sizes.

Gels containing 10 % (v/v) polyacrylamide (Table 2.11) were casted using MiniPROTEAN Tetra Cell System (Bio-Rad, Munich). Samples were prepared in 5x sample buffer and heated to 46 °C for 30 min before loading to the gel. Separation was done at a constant electrical current of 40 mA per gel. BlueElf Prestained Protein Marker (Jena Bioscience, Jena) was used to estimate the MW of protein bands. The resolving gel was supplemented with 0.5 % (v/v) TCE to enable rapid detection of Trp containing protein bands after excitation with UV light [168]. Staining of polyacrylamide gels was done by incubating the gels for 2 h in fresh blue silver staining solution, followed by destaining in H_2O for 1-2 h. Images were recorded with ChemiDoc XRS (Bio-Rad, Munich) and analyzed with Image Lab [169].

Table 2.11: Gel composition for SDS-PAGE

	Stacking gel (5 %)	Resolving gel (10 %)
H2O	6.80 mL	8.20 mL
Acrylamide (30 %)	1.70 mL	10.00 mL
1 M TRIS pH 8.8	-	6.30 mL
1 M TRIS pH 6.8	1.25 mL	-
10 % (w/v) SDS	0.10 mL	0.25 mL
10 % (w/v) APS	0.10 mL	0.25 mL
TEMED	0.01 mL	0.01 mL
Total volume	*~10 mL*	*~25 mL*

Table 2.12: Buffer composition for SDS-PAGE

Name	Composition
5x sample buffer	62 mM TRIS; 2 % (w/v) SDS; 5 % (v/v) β-ME; 20 % (w/v) Glycerol; 0.2 % (w/v) Bromphenol blue
Electrophoresis buffer	25 mM TRIS; 192 mM Glycine; 0.1 % (w/v) SDS
Blue silver staining	10 % (v/v) H_3PO_4; 10 % (w/v) $(NH_4)_2SO_4$; 20 % (v/v) MeOH; 0.15 % (w/v) Coomassie G-250

2.2.2.4.3 Western blot immunodetection

After separation by SDS-PAGE (2.2.2.4.2), the method described in [170,171] was used to transfer the proteins to a PVDF membrane through electrophoresis. Alternatively, the sample was directly spotted onto a nitrocellulose membrane without prior electrophoretic separation [172]. Transferred proteins will be detected through antibody mediated chemiluminescence. The Western blot membrane is incubated with an antibody, that specifically binds to an epitope of the target protein. The primary (α-his) or secondary (α-rho) antibody is conjugated to the enzyme horseradish peroxidase (HRP), which catalyzes the oxidation reaction of luminol in presence of H_2O_2. During this reaction, the luminol molecule emits photons at a wavelength of 428 nm, that can be detected with a camera.

The PVDF membrane (GE Healthcare, Munich) was activated for 30 sec. in MeOH and incubated for 5 min together with Whatman paper and SDS-PAGE gel (2.2.2.4.2) in Transfer buffer (Table 2.13). Semi-dry transfer was done using Trans-Blot Turbo Transfer System (Bio-Rad, Munich) at constant 2.5 A for 5-10 min. Alternatively, sample was added in steps of 2 µL to the membrane with 5 min drying time until a total volume of 10 µL was reached. After transfer, membrane was washed in TBS buffer for 10 min, followed by 30 min incubation with Blocking buffer at RT. The primary antibody was added to the Blocking buffer in a dilution of 1:10.000

(α-his) or 1:5.000 (α-rho), respectively and incubated at RT for 1 h or at 4 °C overnight. The membrane was washed 2x 10 min with TBS-T and 1x 10 min with TBS. In case of rho-hSERT, the membrane was incubated with a secondary antibody (α-mouse) for 1 h at RT or 4 °C overnight followed by the same washing steps mentioned before. Equal volumes of ECL I and ECL II were mixed and added to the membrane. Images were immediately recorded using ChemiDoc XRS (Bio-Rad, Munich) and analyzed with Image Lab [169].

Table 2.13: Buffers used for Western blot transfer and antibody incubation

Name	Composition
Transfer buffer	39 mM Glycine; 48 mM TRIS; 20 % (v/v) MeOH
TBS	20 mM TRIS pH 7.6; 137 mM NaCl
TBS-T	20 mM TRIS pH 7.6; 137 mM NaCl; 0.1 % (v/v) Tween 20
Blocking buffer	5 % (w/v) non-fat milk powder in TBS
ECL I	100 mM TRIS pH 8.5; 0.0066 % (w/v) *p*-coumaric acid; 0.044 % (w/v) luminol
ECL II	100 mM TRIS pH 8.5; 0.022 % (v/v) H2O2

2.2.2.4.3 Mass spectrometry

Protein identification based on mass spectrometry was done using MALDI-TOF method. Protein bands in blue-silver stained SDS-PAGE (2.2.2.4.2) were submitted to EMBPL SPC (Hamburg) for analysis [173].

2.2.3 Biophysical methods

2.2.3.1 Circular dichroism spectroscopy

Circular dichroism (CD) spectroscopy is based on the differential absorption of left-handed and right-handed circular polarized light that passes through a sample with chiral chromophores [174]. Since all proteinogenic amino acids except Gly are chiral, the protein molecule itself is also considered as a chiral molecule and therefore absorbs left-handed and right-handed circular polarized light differently. In the far UV range (<260 nm), the peptide bond is the main contributing group to the CD spectrum. Different secondary structures exhibit a characteristic CD spectrum as shown in Figure 2.1. This technique is widely used to investigate secondary structure and functions in solution [175,176]. Furthermore, it can be used to determine the thermodynamics of protein unfolding and to monitor protein aggregation during thermal unfolding [177,178].

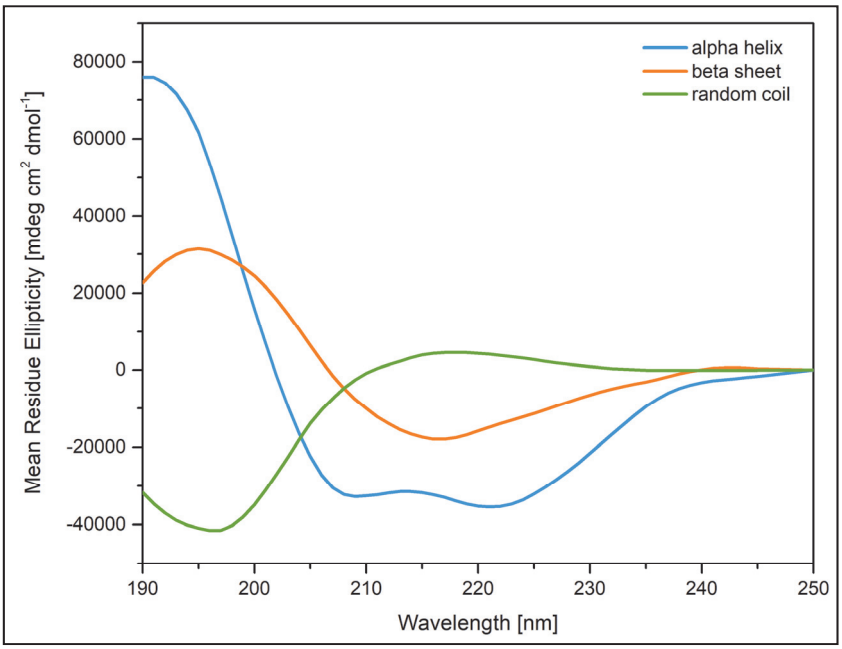

Figure 2.1: CD spectra for poly-*L*-lysine in different conformations. The pure α-helical spectrum (blue) exhibits two negative peaks at 208 nm and 222 nm, respectively. The pure β-sheet structure (orange) exhibits a negative peak at 218 nm and the pure random coil structure (green) shows a positive peak between 210 – 220 nm and a negative at 195 nm (adapted from [179]).

All measurements were done using an Aviv CD425 spectrometer (Aviv Biomedical, Lakewood) with a quartz cuvette of 1 mm path length. Purified hSERT was concentrated to ~1 mg mL^{-1} and then diluted in a ratio of 1:10 with CD buffer (10 mM NaH_2PO_4, pH 7.5; 150 mM NaF; 0.5 mM TCEP; 0.1 % (w/v) Fos-choline 12; 0.01 % (w/v) CHS) to a final volume of 300 µL. Ligands were prepared at a 100x stock solution over the desired final concentration in CD buffer, added to the sample and incubated for 10 min on ice. Measurements of single CD spectra were recorded at 4 °C. CD spectra were collected from 260-180 nm. For thermal unfolding experiments, the sample was heated from 5 °C to 95 °C in steps of 5 °C with a heating rate of 1 °C per minute and a signal averaging time of 6 sec.

Signal of CD spectra was normalized using equation 2 [174]:

$$[\theta]_{mrw,\lambda} = \frac{MRW \times \theta_\lambda}{10 \times d \times c} \qquad (2)$$

where $[\theta]_{mrw,\lambda}$ is the mean residue ellipticity (deg cm² dmol^{-1}), θ_λ is the observed ellipticity (degrees) at wavelength λ, d is the path length (cm), and c is the concentration (g mL^{-1}). The mean residue weight (MRW) was calculated according to equation 3:

$$\mathrm{MRW} = \frac{MW}{N-1} \qquad (3)$$

where MW is the molecular weight of the polypeptide chain (Da) and N the number of amino acids in the chain.

Secondary structure estimation was done by data deconvolution using DichroWeb online server with CDSSTR analysis algorithm using SMP180 reference set for membrane proteins [180–182]. Prediction of secondary structure content based on amino acid sequence was done using Predict Protein [183] and TMHMM server [184].

For evaluation of thermal protein unfolding, the CD signal at 222 nm was corrected as described in [185,185,185]. The fraction of unfolded (f_U) protein was calculated following equation 4:

$$f_U \cong \mathrm{y}_U = \frac{y - y_N}{y_D - y_N} \tag{4}$$

with y_N and y_D as the signal at the initial native or final denatured state, respectively. The fraction unfolded was plotted as a function of temperature and nonlinear regression analysis was carried out using equation 5 [185]:

$$\mathrm{y} = \frac{(y_F + s_F \times T) + (y_U + s_U \times T) \times e^{E(\frac{1}{T_m} - \frac{1}{T})}}{1 + e^{E(\frac{1}{T_m} - \frac{1}{T})}} \tag{5}$$

where y_F and y_U is the signal at folded and unfolded state, respectively, s_F and s_U is the slope at folded and unfolded state baseline, respectively, T is the absolute temperature (K), T_m is the melting temperature (K) and E is the free energy of unfolding (ΔG) divided by the ideal gas constant R (8.314 J mol^{-1} K^{-1})

2.2.3.2 Fluorescence spectroscopy

Fluorescence occurs, when an orbital electron is excited from its ground state S_0 to a higher singlet state S_1 upon absorption of photons (Figure 2.2). The excited electron can partly relax to a lower S_1 state through non-radiative transition, where the excitation energy is dissipated as heat to the environment. During the relaxation to S_0 ground state, the remaining excitation energy is released in a radiative transition, where the molecule emits photons. The wavelength of the emitted photons is shifted to a longer wavelength compared to the wavelength used for excitation.

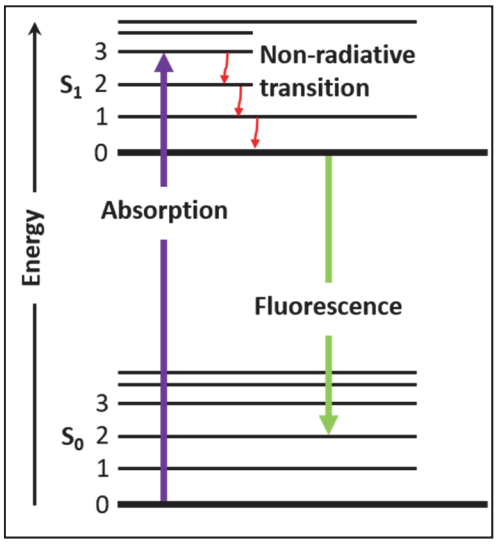

Figure 2.2: Jablonski scheme of fluorescence radiation. An orbital electron is excited from its ground state S_0 to a higher singlet state S_1 upon absorption (purple arrow) of photons. The excited electron can partly relax to a lower S_1 state through non-radiative transition (red arrows), where the excitation energy is dissipated as heat to the environment. During the relaxation to S_0 ground state, the remaining excitation energy is released in a radiative transition (green arrow), where the molecule emits photons of a shorter wavelength.

Investigation of protein properties can be done by either using an intrinsic fluorophore or by adding an extrinsic fluorochrome that will bind to the protein. Among the three aromatic amino acids, the emission spectrum of Trp shows the highest quantum yield (fluorescence intensity) and is therefore the preferred intrinsic fluorophore. Emission spectra of Trp reveal information about the microenvironment of Trp residues. Denaturation and unfolding leads to a decreasing fluorescence quantum yield and thereby to a shift of the emission maxima towards shorter or longer wavelengths.

Fluorescence spectroscopy experiments with hSERT using intrinsic Trp fluorescence were done with Aviv CD425 spectrometer (Aviv Biomedical, Lakewood) with a quartz cuvette of 1 mm path length. Purified hSERT was concentrated to ~1 mg mL^{-1} and then diluted in a ratio of 1:10 with CD buffer (10 mM NaH_2PO_4, pH 7.5; 150 mM NaF; 0.5 mM TCEP; 0.1 % (w/v) Fos-choline 12; 0.01 % (w/v) CHS) to a final volume of 300 µL. Ligands were prepared at a 100x stock solution over the desired final concentration in CD buffer, added to the sample and incubated for 10 min on ice. Emission spectra were collected from 450-280 nm with steps of 1 nm. For thermal unfolding experiments, the sample was heated from 5 °C to 95 °C in steps of 5 °C with a heating rate of 1 °C per minute and a signal averaging time of 1 sec.

For evaluation of thermal protein unfolding, the fluorescence data was corrected as described in [186]. The fraction of unfolded protein was calculated according to equation 5 (2.2.3.1) and plotted as a function of temperature. Non-linear regression analysis of protein

unfolding that follows a two-state transition from folded (F) to unfolded (U) state (F → U) is described by equation 6 [186]:

$$y = \frac{1}{1 + e^{(S - \frac{H}{T})}} \tag{6}$$

with $S = ln\frac{i}{k_i}$ and $H = \frac{E}{R}$, where i is the frequency factor of fluorescence radiation deactivation, k_i is the first-order rate constant for the deactivation process, E is the activation energy of the deactivation process, R is the gas constant (8.314 J mol^{-1} K^{-1}) and T is the absolute temperature (K). In case of a three-state transition from folded (F) to unfolded (U) state via an intermediate (I) step, the observed signal is the weighted sum of the two transitions F → I and I → U of the structural elements E_1 and E_2 in the protein, respectively, and is described in equation 7 [187]:

$$y = f_1 \times \left(\frac{1}{1 - e^{\left(S1 - \frac{H1}{T}\right)}}\right) + f_2 \times \left(\frac{1}{1 + e^{\left(S2 - \frac{H2}{T}\right)}}\right) \tag{7}$$

with $f_1 + f_2 = 1$ as the molar fraction of structural elements E_1 and E_2, respectively. Corresponding melting temperatures can be derived from the plot at half height of each transition step (equations 8, 9):

$$F \rightarrow I: \qquad y(T_{m1}) = \frac{f_1}{2} \tag{8}$$

$$I \rightarrow U: \qquad y(T_{m2}) = f_1 + \frac{f_2}{2} \tag{9}$$

Differential scanning fluorimetry (DSF) experiments with hSERT using 7-Diethylamino-3-(4'-maleimidylphenyl)-4-methylcoumarin (CPM) [188] or 8-Anilino-1-naphthalenesulfonic acid (ANS) [189] as extrinsic fluorophores were done using MyiQ real-time PCR system (Bio-Rad, Munich) at EMBL SPC, Hamburg. The final protein concentration used for this assay was 1.8 µM (hSERT in 0.1 % (w/v) Fos-choline 12) and 2.4 µM (hSERT in 0.02 % (w/v) DDM), respectively. The used fluorescent dyes and the experimental setup is shown in Table 2.14. Measurements were performed in a temperature range from 25 – 95 °C with a temperature gradient of 1 °C per minute. SEC buffer (Table 2.9) was used as a control. Data was evaluated by plotting the first derivative of the relative fluorescence intensity as a function of temperature and melting temperatures correspond to the maxima and minima of the function.

Table 2.14: Experimental setup and fluorescent dyes for differential scanning fluorimetry

	CPM (9.5 mM stock)	ANS (25 mM stock)
Protein sample (or buffer)	2.5 µL	2.5 µL
Dye solution	1.0 µL	1.0 µL
SEC buffer	21.5 µL	21.5 µL
Total volume	*25.0 µL*	*25.0 µL*

2.2.3.3 Microscale thermophoresis

Microscale thermophoresis (MST) [190,191] is a method that is based on the directed movement of molecules within temperature gradients in solution. Binding events between molecules will alter the size, charge, hydration shell or conformation of molecules and therefore influence the thermophoretic behavior. The temperature gradient will be induced by an infrared laser and movement within the gradient will be monitored through fluorescence, using either intrinsic protein fluorescence or an extrinsic fluorescent dye, that is covalently bound to the target molecule [192]. The experimental setup is shown in Figure 2.3.

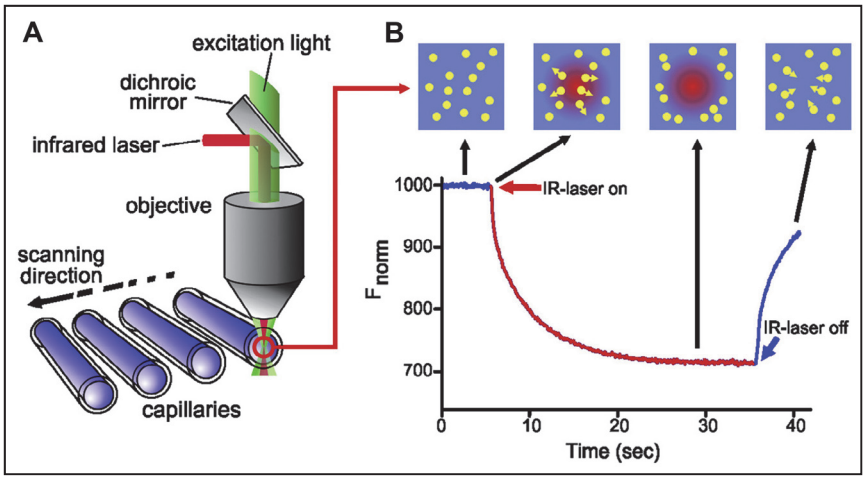

Figure 2.3: Experimental setup of microscale thermophoresis. (A) An infrared laser beam is reflected by a dichroic mirror and focused into the capillary containing aqueous sample to induce a local temperature gradient. A second beam, that can pass through the mirror, is used to excite fluorophores or fluorochromes in the heated spot. The emitted fluorescence is recorded with a CCD camera. (B) The normalized fluorescence is plotted against time. At $t = 5\ s$, the infrared laser is switched on and the temperature increases while labeled molecules move away from the heated spot because of thermophoresis, which leads to a decreased fluorescence signal in the spot. When the infrared laser is switched off, the molecules diffuse back (adapted from [193]).

The locally induced temperature gradient leads to a depletion of molecule concentration in the heated area, which is quantified by the Soret coefficient S_T (equation 10) [194]:

$$\frac{c_{hot}}{c_{cold}} = \exp(-S_T \times \Delta T) \approx 1 - S_T \times \Delta T \qquad (10)$$

with c_{cold} and c_{hot} as the local concentration of the fluorescent molecule before and after heating and ΔT as the induced temperature difference. The normalized fluorescence $F_{norm} = F_{hot}/F_{cold}$ measures this concentration ratio in addition to the temperature dependence of the dye fluorescence $\partial F/\partial T$ (equation 11) [194]:

$$F_{norm} = 1 + \left(\frac{\partial \mathrm{F}}{\partial \mathrm{T}} - S_T\right) \times \Delta \mathrm{T} \qquad (11)$$

Because of the linear correlation between fluorescence intensity and thermophoretic depletion, the normalized fluorescence from unbound molecule $F_{norm}(U)$ and bound complex $F_{norm}(B)$ superpose linearily. The changing fluorescence signal during the titration of target T can be described with equation 12 [194]:

$$F_{norm} = (1 - \mathrm{x}) \times F_{norm}(U) + x \times F_{norm}(B) \qquad (12)$$

with x as the fraction of target bound molecules. Using a serial dilution of target T will reveal quantitative binding parameters. Plotting F_{norm} as a function of concentration $[T]$ will yield a sigmoidal shaped curve. The dissociation constant K_D for a binding event is derived from the following fitting function (equation 13):

$$f_{(c)} = F_{norm}(U) + \frac{F_{norm}(B) - F_{norm}(U)}{2} \times \left(c_{Fl} + c + K_D - \sqrt{(c_{Fl} + c + K_D)^2 - 4 \times c_{Fl} \times c}\right) \qquad (13)$$

with c_{Fl} as concentration of fluorescent molecule and c as the concentration of ligand.

Binding affinity experiments between *E. coli* expressed hSERT and hSERT inhibitors were carried out using Monolith NT.115 (Nanotemper, Munich). Purified hSERT (100-300 nM) was labeled with the fluorescent dye RED-TRIS-NTA647 (Nanotemper, Munich) in a molar ratio between dye:protein of 1:12 at 4 °C overnight. Fluoxetine, Citalopram and Desipramine were titrated over a concentration range from 0.1 nM – 20 mM. Measurements were done at RT using 40 % infrared laser power and 40 % LED power.

2.2.3.4 Surface plasmon resonance

Surface plasmon resonance (SPR) is a method used to investigate molecular binding interactions. It is based on the change of refractive index of a medium in close vicinity of a metal surface upon binding of an analyte molecule to the metal surface [195]. A glass slide coated with a thin gold layer forms the floor of a flow cell (Figure 2.4). To detect binding between ligand and analyte, the ligand needs to be immobilized to the gold surface through a linker

molecule with a functional group. The analyte molecule is then injected into the flow cell. Polarized light from a laser source is directed through a prism to the uncoated side of the glass slide and the intensity of light reflected at the gold film will be recorded by a detector on the other side of the prism. At a critical angle, total internal reflection occurs along with an evanescent wave that interacts with the gold electrons and creates a surface plasmon, an electron wave that travels along the upper gold surface [196]. The partial conversion of energy from incident polarized light into a surface plasmon can be observed as a localized drop in reflected light intensity, which allows detection of the critical angle. This critical angle highly depends on the difference of refractive index between both sides of the gold film, the glass side, and the aqueous side. Binding of an analyte molecule to the surface of the gold film changes the local refractive index and therefore shifts the angle of light energy coupled to the surface plasmon wave. Thus, the angle of lowest reflection intensity changes in response to the amount of mass coupled near (< 300 nm) the gold surface. The angular shift of the low intensity band is plotted as 'Response Units' (RU) against time to obtain a sensorgram, that visualizes association und dissociation of the analyte molecule to the surface.

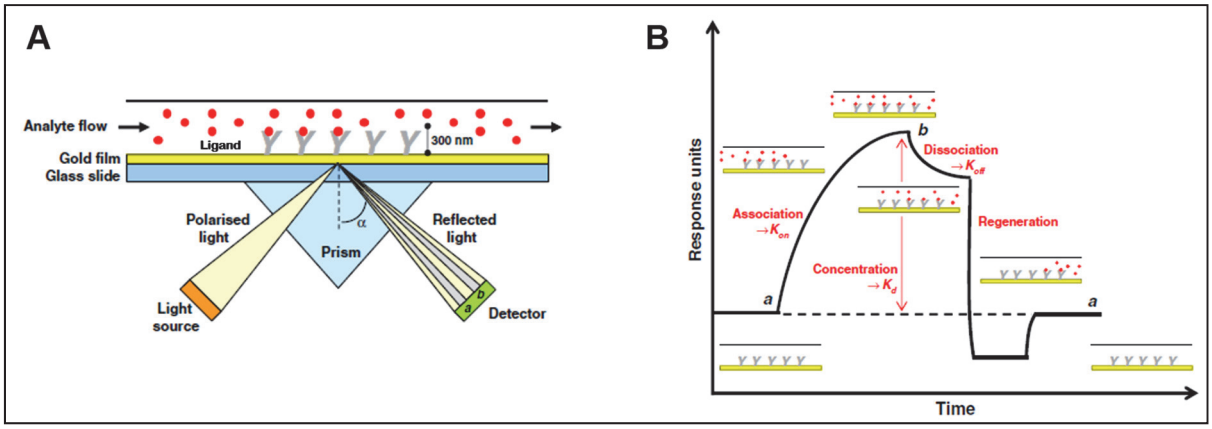

Figure 2.4: Experimental setup and basic principle of surface plasmon resonance. (A) A glass slide coated with a thin gold layer forms the floor of a flow cell. The ligand is immobilized to the gold surface through a linker molecule with a functional group. The analyte molecule is then injected into the flow cell. Polarized light from a laser source is directed through a prism to the under surface of the gold layer and the reflected light will be recorded by a detector. At a critical angle, total internal reflection occurs along with an evanescent wave that interacts with the gold electrons and creates a surface plasmon. This absorption of light can be detected through a decrease in intensity of the reflected light (a). The critical angle highly depends on the difference of refractive index between both sides of the gold film, the glass side, and the aqueous side. Binding of an analyte molecule to the surface of the gold film changes the refractive index and therefore shifts the critical angle (b). (B) The angular shift of the low intensity band is plotted as 'Response Units' (RUs) against time to obtain a sensorgram, that visualizes association und dissociation of the analyte molecule (adapted from [195]).

Binding affinity experiments carried out on a Reichert SR7500DC instrument (Xantec bioanalytics, Düsseldorf) were measured at 10 °C. N-His-SERT was immobilized for 15 min (flow rate 5µL min^{-1}) in one cell within a NiHC1000 sensor chip (Xantec bioanalytics,

Düsseldorf) to obtain around 4400 response units (RUs). The second cell was used as a control. Both cells were equilibrated with SPR running buffer I (20 mM TRIS; 150 mM NaCl; 10 % (w/v) Glycerol; 0.1 % (w/v) FC12; pH 7.5) to establish a stable baseline. Citalopram or desipramine were dissolved in SPR running buffer and injected (flow rate 30 µL min^{-1}) over the captured transporter and the reference cell at a concentration range from 50 pM to 5 µM. Association was monitored for 2.5 min and dissociation was monitored for 7.5 min. Each injection of analyte was followed by a buffer blank injection with SPR running buffer I. No regeneration was performed between analyte injections.

Binding affinity experiments carried out on a Biacore T200 instrument (GE Healthcare, Munich) were measured at 21 °C. N-His-SERT was immobilized for 5x 5 min (flow rate 5µL min^{-1}) in one cell within a Series S Senor Chip NTA (GE Healthcare, Munich) to obtain around 4,000 – 9,000 RUs. The second cell was used as a control. Both cells were equilibrated with SPR running buffer II (137 mM NaCl; 2.7 mM KCl; 10 mM Na_2HPO_4; 1.8 mM KH_2PO_4; 0.1 % (w/v) FC12; pH 7.5) to establish a stable baseline. Citalopram, desipramine or fluoxetine were dissolved in SPR running buffer and injected (flow rate 20 µL min^{-1}) over the captured transporter and the reference cell at a concentration range from 50 pM to 5 µM. Association was monitored for 2.5 min and dissociation was monitored for 7.5 min. Each injection of analyte was followed by a buffer blank injection with SPR running buffer II. No regeneration was performed between analyte injections.

Signal from sample injection as well as from blank injection were referenced against their respective signal from the empty flow cell. The initial three blank injection cycles after referencing showed a weak binding signal during injection within the range of 2-5 response units (RUs), while later blank cycle injections showed a stable baseline. Therefore, referenced blank data was not subtracted from referenced sample data. Data was adjusted on the x and y axis to compensate large bulk shifts during and after injection.

Equilibrium analysis was done using different linear transfomation methods: response units at the equilibrium phase (R_{eq}) after 90 sec. were normalized to the maximum binding signal ($Rmax$) and plotted as a function of the free analyte concentration [c] on a semi-logarithmic scale. This representation is known as Klotz plot [197] and the equilibrium dissociation constant K_D can be derived from the free analyte concentration $[c]$ that corresponds to half-maximum occupancy according to equation 14:

$$\frac{R_{eq}}{R_{max}} = \frac{[c]}{(k_D + [c])} \qquad (14)$$

For the Scatchard plot [198], the ratio of R_{eq} to free analyte [c] is plotted as a function of R_{eq}. In case of a linear relation, the slope of this line corresponds to the negative inverse of K_D as shown in equation 15:

$$\frac{R_{eq}}{[c]} = \frac{-R_{eq}}{k_D} + \frac{R_{max}}{k_D} \tag{15}$$

Data was log transformed for the Hill plot [199] analysis according to equation 16:

$$\log\left(\frac{R_{eq}}{R_{max} - R_{eq}}\right) = \mathrm{n} \times (\log[c]) - \log(k_D) \tag{16}$$

with n as Hill coefficient. Equation 16 is a linear equation where the slope of the line equals n and the y-intercept equals $-\log(k_D)$.

Kinetic analysis was carried out with TraceDrawer [200], BIAevaluation [201] or with Origin [202]. Nonlinear regression analysis was done using the following interaction models: 1:1 Langmuir binding, heterogeneous ligand, induced fit and conformational selection. Furthermore, an interaction model has been developed to account for negative cooperativity binding. The reaction schemes for the models tested in this study are shown in Figure 2.5.

1:1 Langmuir	Heterogeneous ligand	Induced fit	Conformational selection	Allosteric modulation
$L + A \underset{k_d}{\overset{k_a}{\rightleftharpoons}} LA$	$L + A \underset{k_{d1}}{\overset{k_{a1}}{\rightleftharpoons}} LA^1$ $L + A \underset{k_{d2}}{\overset{k_{a2}}{\rightleftharpoons}} LA^2$	$L^* + A \underset{k_{d1}}{\overset{k_{a1}}{\rightleftharpoons}} L^*A \underset{k_{d2}}{\overset{k_{a2}}{\rightleftharpoons}} LA$	$L^* \underset{k_{d1}}{\overset{k_{a1}}{\rightleftharpoons}} L + A \underset{k_{d2}}{\overset{k_{a2}}{\rightleftharpoons}} LA$	$L + A \underset{k_{d1}}{\overset{k_{a1}}{\rightleftharpoons}} LA^1 + A \underset{k_{d2}}{\overset{k_{a2}}{\rightleftharpoons}} LA^1A^2$ $L + A \underset{k_{d2}}{\overset{k_{a2}}{\rightleftharpoons}} LA^2 + A \underset{k_{d3}}{\overset{k_{a3}}{\rightleftharpoons}} LA^1A^2$

Figure 2.5: Reaction schemes of binding models. L denotes the ligand and A the analyte molecule, k_a is the second-order association rate constant and k_d is the first-order dissociation rate constant. A superscript star ($*$) indicates a conformational change of ligand and a superscript number of analyte molecule indicates primary (1) or secondary (2) binding site of SERT.

The simple 1:1 binding of ligand (L) and analyte (A) is described by the Langmuir adsorption model [203], the fitting equations for dissociation and association phase derived from this model are given by equations 17 and 18, respectively:

$$y = y_0 \times e^{(k_d \times (x_0 - x))} + R \tag{17}$$

$$y = y_o \times (1 - e^{((k_a \times c + k_d) * (x_0 - x))}) \quad (18)$$

where y_0 is the signal at equilibrium (RU), k_d (s^{-1}) is the first-order dissociation rate constant, k_a (M^{-1} s^{-1}) is the second-order association rate constant, x is time (s), x_0 is the time point of start or stop of injection, c is the concentration of analyte (mol L^{-1}) and R (RU) is the residual response at infinite time. The model for a heterogeneous ligand assumes that a second analyte molecule A binds to a secondary binding site on the same ligand molecule. Primary and secondary site are independent and binding and unbinding from individual sites is described with two sets of rate constants. In this case, the observed binding signal is the sum of two different binding or unbinding events, hence dissociation and association are the sum of two exponential equations as derived from the Langmuir model (equations 19, 20):

$$y = y_0 \times e^{(k_{d1} \times (x_0 - x))} + e^{(k_{d2} \times (x_0 - x))} + R \quad (19)$$

$$y = y_0 \times (1 - e^{((k_{a1} \times c + k_{d1}) * (x_0 - x))}) + (1 - e^{((k_{a2} \times c + k_{d2}) * (x_0 - x))}) \quad (20)$$

Involvement of a conformational transition in binding interaction can be described with two different schemes [204], induced fit and conformational selection, respectively. In the induced fit model, the conformation of the ligand changes only after binding of an analyte molecule and rate constants k_{a2} and k_{d2} refer to the transition from L^*A to LA and backward, respectively. This scheme is the simplest form of the Koshland-Nemethy-Filmer model of allosteric transitions [205], based on the induced-fit hypothesis [206]. The set of differential equations associated with this scheme is given by equation 21:

$$\begin{pmatrix} d[L^*]/dt \\ d[L^*A]/dt \\ d[LA]/dt \end{pmatrix} = \begin{pmatrix} -k_{a1}[A] & k_{d1} & 0 \\ k_{a1}[A] & -k_{a2} - k_{d1} & k_{d2} \\ 0 & k_{a2} & -k_{d2} \end{pmatrix} \begin{pmatrix} [L^*] \\ [L^*A] \\ [LA] \end{pmatrix} \quad (21)$$

The conformational selection model assumes a preexisting equilibrium of the ligand in two different conformations L^* and L, of which only L can interact with analyte A. In this case, the rate constants k_{a1} and k_{d1} refer to the transition from L^* to L and backward, respectively. This scheme is the simplest form of the Monod-Wyman-Changeux model of allosteric transitions [207]. The set of differential equations associated with this scheme is given by equation 22:

$$\begin{pmatrix} d[L^*]/dt \\ d[L]/dt \\ d[LA]/dt \end{pmatrix} = \begin{pmatrix} -k_{a1} & k_{d1} & 0 \\ k_{a1} & -k_{d1} - k_{a2}[A] & k_{d2} \\ 0 & k_{a2}[A] & -k_{d2} \end{pmatrix} \begin{pmatrix} [L^*] \\ [L] \\ [LA] \end{pmatrix} \quad (22)$$

The allosteric modulation model is an extended form of the heterogeneous ligand model. In this case, binding and unbinding to the secondary binding site is independent of the occupancy of the primary binding site, whereas binding and unbinding to the primary site depends on the occupancy of the secondary site and the rate constants are altered (k_{a3}, k_{d3}) if the second site is occupied. The set of differential equations associated with this scheme is given by equation 23:

$$\begin{pmatrix} d[L]/dt \\ d[LA_1]/dt \\ d[LA_2]/dt \\ d[LA_1A_2]/dt \end{pmatrix} = \begin{pmatrix} -(k_{a1}[A] + k_{a2}[A]) & k_{d1} & k_{d2} & 0 \\ k_{a1}[A] & -(k_{a2}[A] + k_{d1}) & 0 & k_{d2} \\ k_{a2}[A] & 0 & -(k_{a3}[A] + k_{d2}) & k_{d3} \\ 0 & k_{a2}[A] & k_{a3}[A] & -(k_{d2} + k_{d3}) \end{pmatrix} \begin{pmatrix} [L] \\ [LA_1] \\ [LA_2] \\ [LA_1A_2] \end{pmatrix} \quad (23)$$

Fitting equations of induced fit, conformational selection and allosteric modulation model for association and dissociation phase where calculated with Mathematica [208] and are shown in Appendix B.

2.2.4 X-ray crystallography

2.2.4.1 Protein crystallization

The three-dimensional structure solution of protein molecules through x-ray diffraction (2.2.4.2) requires the desired protein in its crystallized form. In aqueous solutions, crystallization can appear if a certain substance exceeds its solubility and reaches a state of oversaturation before it undergoes phase transition. For example, organic or inorganic compounds can be crystallized by slow cooling of a hot, saturated solution of this compound or by adding organic solvents [209]. Since exposure to heat and organic solvents denatures the protein, these techniques cannot be used for protein crystallization. Instead, proteins can be crystallized by adding a precipitant like $(NH_4)_2SO_4$ or PEG just below the concentration necessary to precipitate the protein. This mixture will be incubated in a closed system against the precipitant solution, usually in sitting drop or hanging drop mode. An ideal phase diagram for a typical crystallization experiment is shown in Figure 2.6. Usually, purified protein solution and precipitant solution will be mixed in a 1:1 volume ratio so that the precipitant concentration in the protein drop is half of that concentration found in the precipitant solution (1). Water from

the protein-precipitant drop will be removed through vapor diffusion to achieve an equilibrium for the precipitant concentration between both solutions. This leads to an increase of protein concentration which eventually reaches a phase, where forming of crystal nuclei occurs (2). The precipitation of protein from the solution will decrease the dissolved protein concentration and brings the experiment to the metastable zone, where protein molecules will attach to the nuclei, resulting in crystal growth (3). Initial crystallization experiments require extensive screening of a wide range of different precipitants in different concentrations to find conditions that lead to crystal formation.

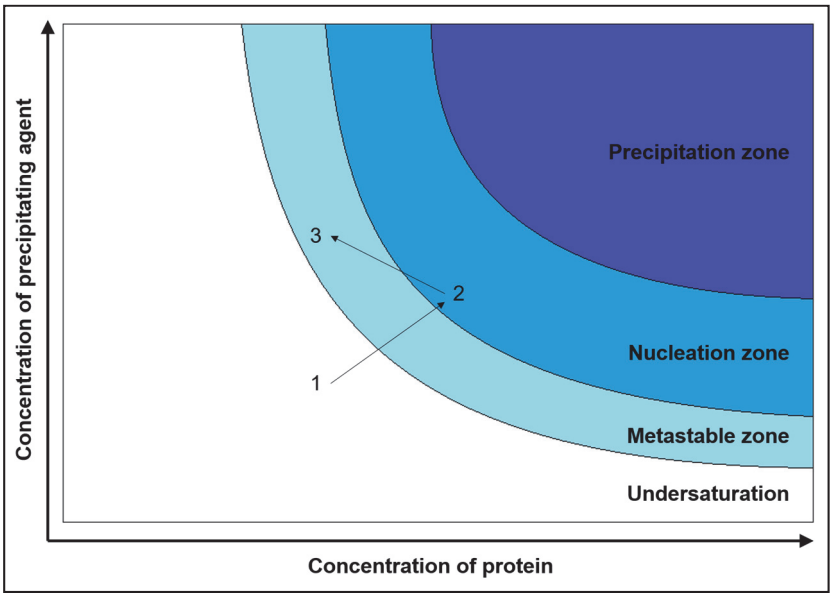

Figure 2.6: Phase diagram for protein crystallization through vapor diffusion. Usually, purified protein solution and precipitant solution will be mixed in a 1:1 volume ratio so that the precipitant concentration in the protein drop is half of that concentration found in the precipitant solution (1). Water from the protein-precipitant drop will be removed through vapor diffusion to achieve an equilibrium for the precipitant concentration between both solutions. This leads to an increase of protein concentration which eventually reaches a phase, where forming of crystal nuclei occurs (2). The precipitation of protein from the solution will decrease the dissolved protein concentration and brings the experiment to the metastable zone, where protein molecules will attach to the nuclei, resulting in crystal growth (3).

In contrast to soluble proteins, membrane proteins are purified with detergents to solubilize their membrane. In principle, detergent-solubilized membrane proteins can be crystallized using the same methods as for soluble proteins. The standard vapor diffusion crystallization from a detergent-protein solution (*in surfo* method) yields type II membrane protein crystals (Figure 2.7 A), that are highly disordered and therefore diffract to low resolution only [210,210,211]. Methods have been developed, that are using lipids or mixtures of short chain and long chain detergents to mimic the native lipid bilayer. These methods enable the growth of type I membrane protein crystals (Figure 2.7 B), that have a denser packing and diffract to higher resolution. The crystallization in bicelles uses a mixture of amphiphiles (detergent or

short-chain lipid) and long-chain lipids, that forms a disc shaped structure. Addition of detergent-solubilized membrane protein to the bicelle solution and incubation for 30 min leads to an integration of the membrane protein into the bilayer (Figure 2.7 C) [212]. This mixture can then be used for vapor diffusion crystallization experiments. The lipid cubic phase (LCP) crystallization method was initially described in 1996 [213]. It uses a mixture of monoolein (1-Oleoyl-rac-glycerol, MO) and water, that forms a bicontinuous cubic phase to accommodate the hydrophobic part of membrane proteins (Figure 2.7 D).

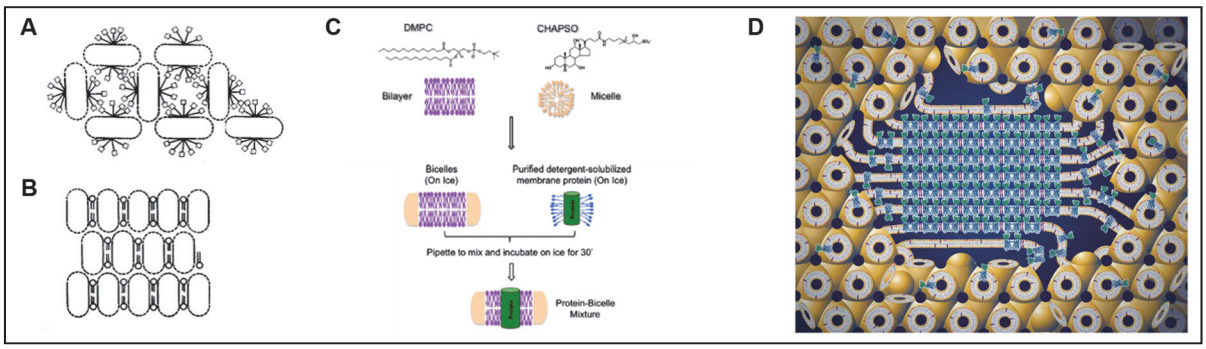

Figure 2.7: Membrane protein crystallization. (A) Standard vapor diffusion experiments for detergent solubilized membrane proteins yields type II crystals that diffract to low resolution only. (B) Crystal packing for type I membrane protein crystals, that diffract to higher resolution (A and B adapted from [210]). This type of crystals can be grown with methods that are mimicking the native lipid bilayer. (C) Bicelle crystallization uses a mixture of amphiphiles and long-chain lipids, that forms a disc-shaped structure with the membrane protein integrated into the bilayer (adapted from [212]). (D) Bicontinuous cubic phase composed of monoolein (tan), water (dark blue) and membrane protein (blue and green). The membrane protein is reconstituted into the curve bilayer of bicontinuous cubic phase. Adding precipitants leads to phase separation and diffusion of protein molecules into the lattice of the advancing crystal face (adapted from [214]).

Compared to detergent-based crystallization, crystals obtained from LCP showed a lower solvent content and a higher ordering [215]. Based on this method, the controlled *in meso* phase (CIMP) crystallization was described in 2012 [216]. Instead of directly mixing monoolein and membrane protein solution through a syringe, this technique uses standard 96-well crystallization plates with pre-coated MO spots in each well. The membrane protein solution will be added to the MO spot and incubated for 2-3 h. Afterwards, the precipitant solution will be added to the drop. Using different dilutions of the precipitant solution allows direct control over the cubic phase' hydration level and therefore targeting different meso phases (Figure 2.8).

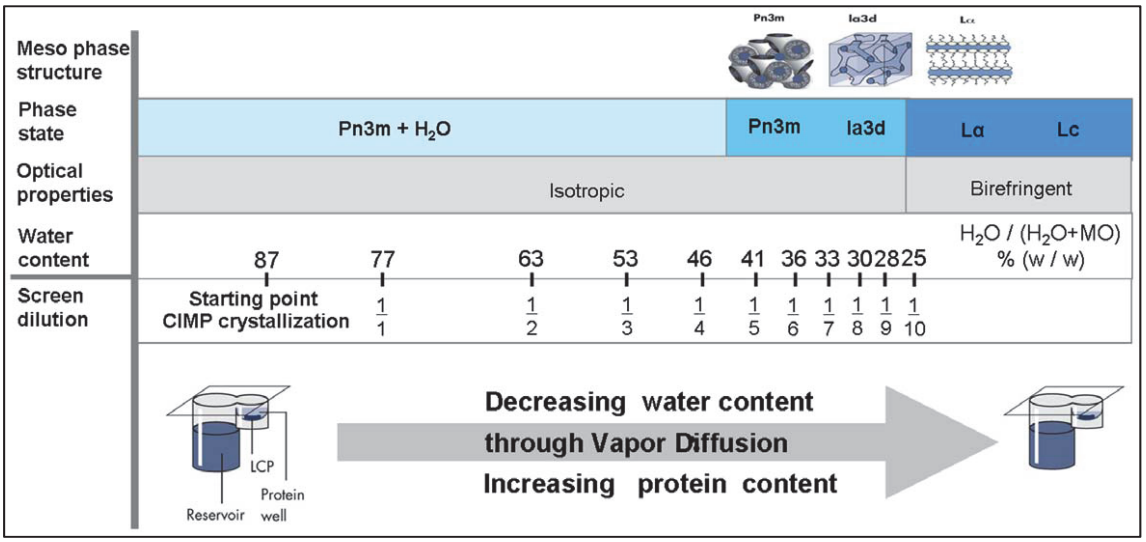

Figure 2.8: Simplified phase diagram of monoolein/water at 22 °C. With increasing water content, the layered lamellar phases (Lc, Lα), cubic phases (Ia3d, Pn3m) and the phase Pn3m + water are formed. The water content required for the formation of individual phases can be targeted by vapor diffusion and addition of diluted precipitant solution as indicated (adapted from [216]

For crystallization experiments using *in surfo* method, hSERT with a purity >95 % was concentrated to 3 mg mL^{-1}. The concentrated protein solution was dispensed into each crystallization well of a MRC 2-well crystallization plate (Jena Bioscience, Jena) with a volume of 100 – 200 µL using mosquito LCP robot (TTP Labtech, Melbourn). Equal volume of reservoir solution was added to the protein drop and the experiment was incubated against 75 µL reservoir solution. Plates were sealed and incubated at 4 °C and 16 °C, respectively..

Bicelle solutions were prepared at a final concentration of 40 % (w/v) with a molar ratio of DMPC:CHAPSO at 2.6:1, 2.8:1 and 3.0:1, respectively. Detergent purified hSERT was concentrated to 3 mg mL^{-1} and added to the bicelle solution at a ratio of 4:1 (v/v), yielding a final bicelle concentration of 8 % (w/v). After incubating the mixture on ice for 30 min, crystallization experiments were set up as described above for *in surfo* method. Plates were sealed and incubated at 16 °C.

Crystallization using the LCP-based CIMP method was done using CubeCrystal 2-well MO plates (Cube Biotech, Monheim). Detergent purified hSERT was concentrated to 3 mg mL^{-1} and dispensed into each well with a volume of 100 – 200 µL using mosquito LCP robot. The plates were sealed and incubated for 3 h at 21 °C. Afterwards, undiluted or a series dilution of screening solution was added to the drop and the experiment was incubated against 75 µL reservoir solution. Plates were sealed and incubated at 21 °C.

2.2.4.2 X-ray diffraction experiments

Crystals were harvested from the drop using nylon cryoloops (Hampton Research, Laguna Niguel) and immediately flash frozen in liquid nitrogen. Perfluoropolyether was used as a cryoprotectant to avoid damage to the crystal structure while freezing [217]. Diffraction experiments were carried out at PETRA III beamline (DESY, Hamburg) using a nitrogen stream to cool the crystals to 100 K during radiation exposure.

3 Results

3.1 Molecular cloning

3.1.1 Cloning of hSERT and Calnexin for insect cell expression

For co-expression of human serotonin transporter (hSERT) and human Calnexin (hCNX) in *S. frugiperda* (Sf9) cells, four constructs were designed and constructed, each in pOET2 and pOET4 transfer vector from OET (Oxford). The initial construct of hSERT was planned as its full-length sequence with the Rho1D4 affinity tag in its C-terminus was cloned into a pOET4 transfer vector. This construct was provided by Cube Biotech (Monheim) and named as p4bv-hSERT. The remaining constructs of hSERT and hCNX with pOET2 or pOET4 vector were designed with Genome Compiler [154] and named as p2bv-hSERT, p2bv-hCNX and p4bv-hCNX. The construct for hCNX was designed to include its full-length sequence along with the N-terminal signal peptide and a C-terminal His_8 affinity tag. The synthetic hCNX gene was obtained from GeneArt (Regensburg). The inserts for hSERT and hCNX were released from their vectors through enzymatic digestion (2.2.2.1.2) with XhoI/BamHI (hSERT) or EcoRI/BamHI (hCNX) and purified through gel separation and subsequent gel extraction (2.2.2.1.4). The target vectors were double-digested with the same restriction enzymes as those used for corresponding insert release and prepared for ligation (2.2.2.1.3). The ligation mix was directly used for transformation (2.2.1.1.2) in *Escherichia coli* (*E. coli*) Top10. Cells were grown on LB agar plates in presence of antibiotics to select vector carrying cells (2.2.1.1.2). Amplified and isolated vector DNA (2.2.2.1.1) from ten positive colonies for each construct was used for enzymatic restriction digestion analysis (Figure 3.1).

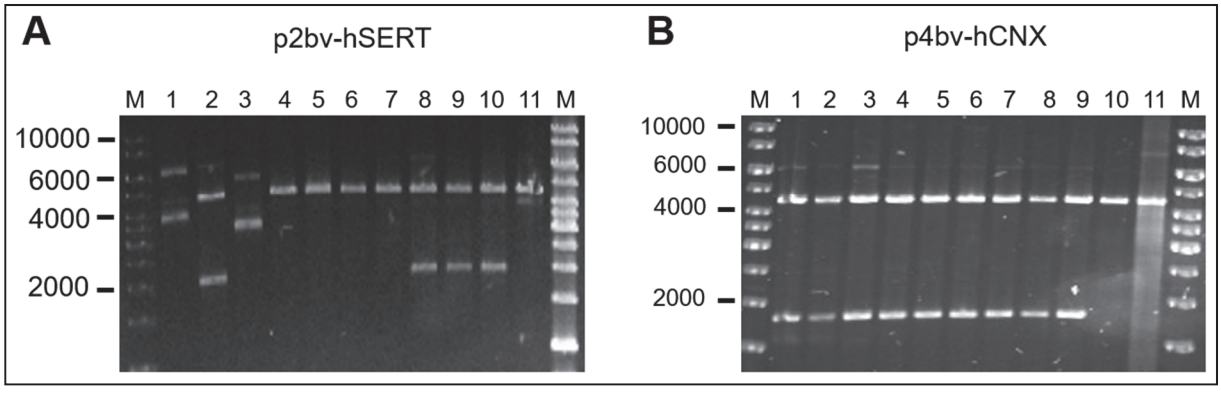

Figure 3.1: Restriction digestion analysis of insect cell expression constructs. Isolated vector DNA was digested with either (A) XhoI/BamHI digestion product of p2bv-hSERT or (B) EcoRI/BamHI digestion product of p4bv-hCNXI. The DNA band between 4.000 – 5.000 bp corresponds to the size of the linearized vector (4501 bp pOET2/pOET4) and the band around 2.000 bp corresponds to the respective insert (1937 bp hSERT; 1814 bp hCNX). M: marker; 1-10: double digested samples of purified plasmids from selected clone; 11: empty vector DNA

The analysis of samples from p2bv-hSERT (Figure 3.1 A) revealed four colonies (2, 8-10), that contained two distinct bands at ~4500 bp and ~2000 bp after enzymatic digestion. For p4bv-hCNX (Figure 3.1 B), nine samples (1-9) could be identified with a similar band pattern. These bands correspond to the size of the linearized transfer vector (pOET2/pOET4: 4501 bp) and the respective insert (hSERT: 1937 bp; hCNX: 1814 bp). Weak bands around 6.000 bp correspond to the size of the undigested construct. Purified DNA from samples that show an insert release where submitted for sequencing (2.2.1.1.6). Sample 10 for p2bv-hSERT and Sample 3 for p4bv-hCNX have been confirmed to contain the full-length sequence including affinity tag. Cloning of construct p2bv-hCNX was carried out by Weihou Guo (CSSB-FZJ).

3.2 Protein expression of hSERT

3.2.1 Protein expression of hSERT fusion protein in *E. coli*

3.2.1.1 Expression analysis of C-Rho-hSERT in different strains of *E. coli*

Following initial protein expression analysis for construct Rho-hSERT in pET20b (Table 2.3), that were done at Cube Biotech (Monheim), protein expression levels were compared between *E. coli* C43 and *E. coli* BL21(DE3) RP using TB medium (Table 2.5) at 20 °C. Samples from the culture were taken every hour over a time course of 16 h post induction with 0.4 mM IPTG. After sedimentation (10.000 × g; 5 min), cells were resuspended in Lysis buffer (Table 2.9) at a concentration of 25 mg cell pellet per mL buffer and lysed through repeated freeze-thaw cycles followed by 30 min incubation in an ice-cold ultrasonic bath. Samples for SDS-PAGE were prepared from lysate after sedimentation (10.000 × g; 40 min). Expression of Rho-hSERT was immunodetected after SDS-PAGE (2.2.2.4.2) and subsequent Western Blot transfer (2.2.2.4.3) as shown in Figure 3.2.

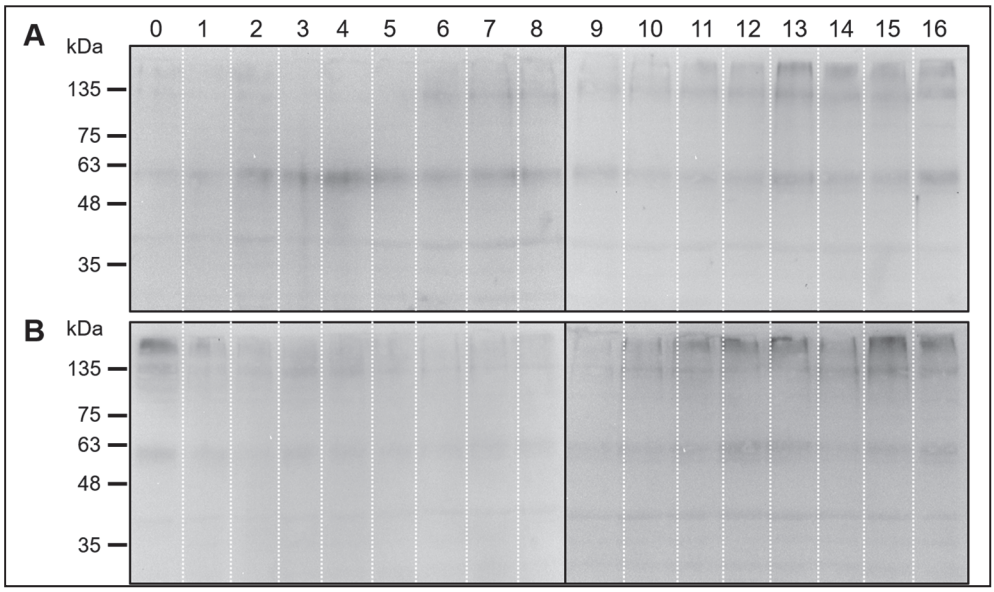

Figure 3.2: Expression analysis of C-Rho-hSERT in different *E. coli* strains. Immunodetection with α-Rho1D4 antibody. **(A)** Samples from the expression of C-Rho-hSERT in *E. coli* C43 using TB medium at 20 °C. **(B)** Samples from the express of C-Rho-hSERT in *E. coli* BL21(DE3) RP using TB medium at 20 °C. Each lane represents the sample after cell lysis and removal of cell debris and inclusion bodies for the indicated time point (h) post protein induction.

The vector pET20b shows a weak basal expression for both tested *E. coli* strains. The strongest expression signal for Rho-hSERT was found around 4 h using *E. coli C43* (Figure 3.2 A). The signal intensity for the full-length monomer around 60 kDa decreases from this time point on while the signal intensity for higher oligomeric states of Rho-hSERT around and above 135 kDa increases after 6 h. The higher oligomeric band can also be observed for Rho-hSERT when expressing in *E. coli* BL21(DE3) RP after 10 h (Figure 3.2 B). In contrast to C43, a dominant band for higher oligomeric forms can be observed prior to IPTG induced protein overexpression. The maximum signal intensity for full-length Rho-hSERT expressed in BL21(DE3) RP can be found after 12-13 h, but the overall expression yield seems to be low compared to C43.

3.2.1.2 Expression analysis of N-His_8-hSERT in different strains of *E. coli*

Protein expression analysis for the construct His_8-hSERT (Table 2.3) were carried out to compare the method established at ICS-6, FZ Jülich (*E. coli* BL21(DE3) RP; ZY-CAIM; 18 °C) with different *E. coli* strains (C41, C43, Lemo21) and with IPTG-induced overexpression using TB medium at 20 °C and 30 °C expression temperatures. Furthermore, expression in *E. coli* Lemo21 was modulated by adding 100 µM L-rhamnose. Preliminary analysis revealed, that concentrations of L-rhamnose above 100 µM abolish expression of His-hSERT in Lemo21. Samples from the culture were taken at certain time points (0, 2, 4, 20 and 24 h) after induction

with 0.4 mM IPTG (TB medium) and after temperature change (ZY-CAIM), respectively, and the optical density at 600 nm during expression was monitored (Figure 3.3). After sedimentation (10.000 × g; 5 min), cells were resuspended in Lysis buffer (Table 2.9) at a concentration of 50 mg cell pellet per mL buffer and incubated at RT for 1 h. Cells were incubated for 20 min in an ice-cold ultrasonic bath followed by sedimentation of cell debris and inclusion bodies at 10.000 g for 10 min. The resulting supernatant was spotted for every sample on a nitrocellulose membrane and expression of His_8-hSERT was detected with α-Penta-His antibody (2.2.2.4.3; Figure 3.4).

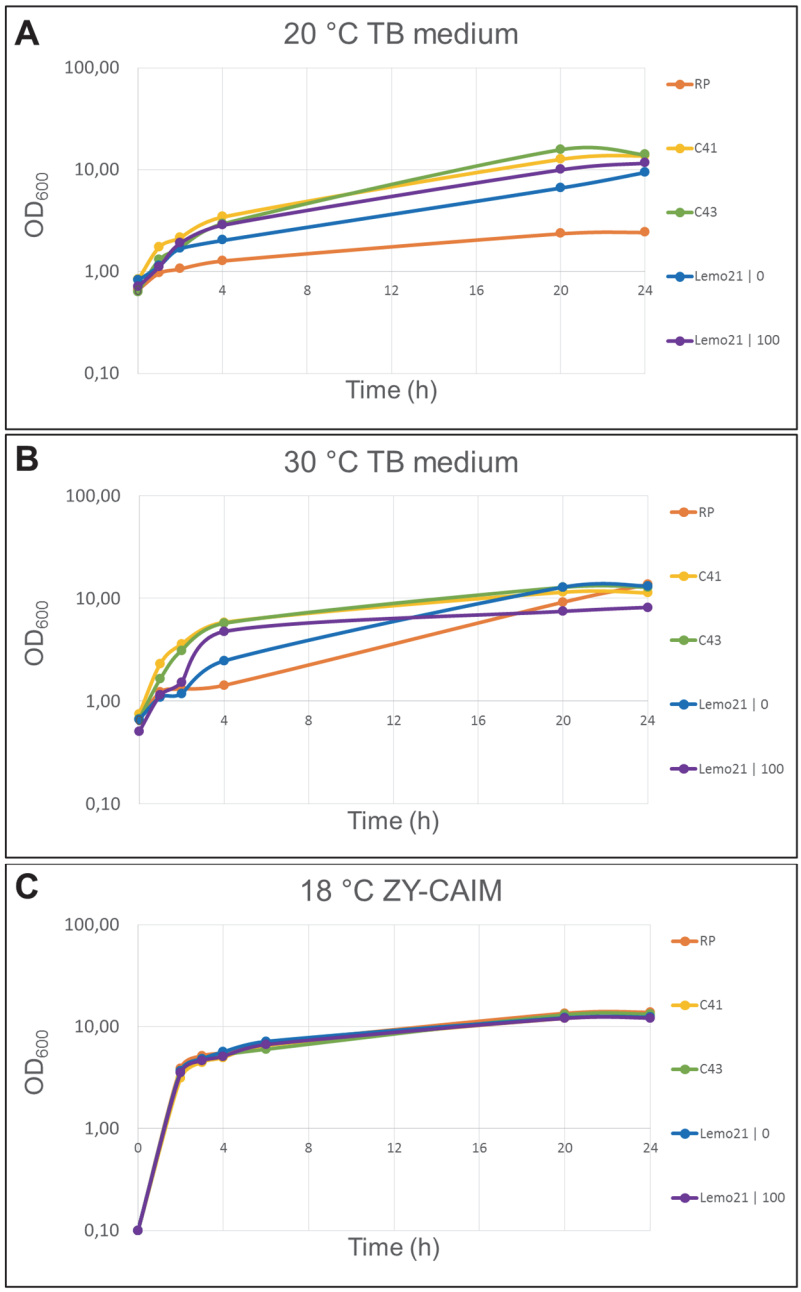

Figure 3.3: Growth curve of different *E. coli* strains expressing N-His_8-hSERT with varying conditions. **(A)** IPTG induced expression in TB medium at 20 °C. **(B)** IPTG induced expression in TB medium at 30 °C. **(C)** Auto-induced expression in ZY-CAIM at 18 °C.

Cells grown in TB medium were incubated at 37 °C and 110 rpm until they reached an OD_{600} of ~0.6. The incubation temperature was changed to either 20 °C or 30 °C and 0.4 mM IPTG was added to the medium. Overexpression of N-His_8-hSERT at either 20 °C or 30 °C was found in BL21(DE3) RP as well as in Lemo21 in absence (Lemo21-) or presence (Lemo21+) of 100 µM L-rhamnose within 1-2 h post induction with IPTG (Figure 3.4 A, 3.4 B). The growth rate of Lemo21+ at 20 °C is higher compared to Lemo21-, with a final cell density of ~12 and ~9, respectively (Figure 3.3 A). At 30 °C, this relationship turns around after ~9 h post induction and the final density reaches ~13 (Lemo21-) and 9 (Lemo21+), respectively (Figure 3.3 B).

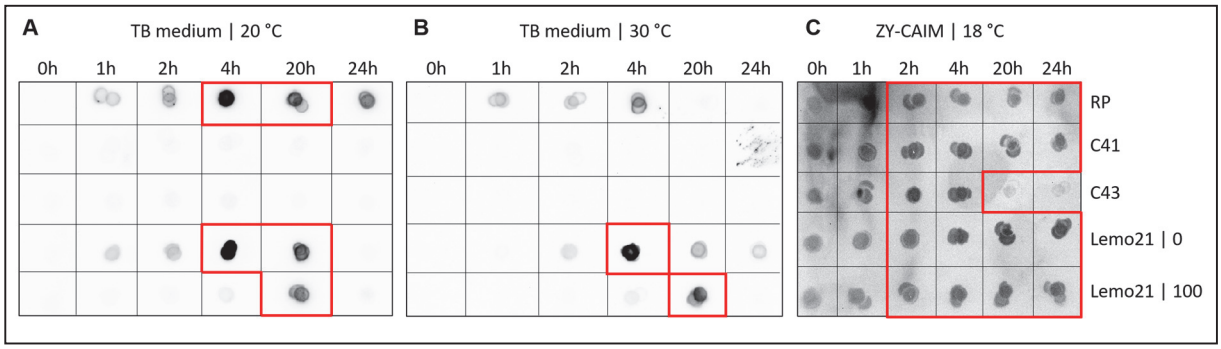

Figure 3.4: Protein expression analysis of N-His_8-hSERT in different *E. coli* strains with varying conditions. Immunodetection with α-His antibody. **(A)** IPTG induced expression in TB medium at 20 °C. **(B)** IPTG induced expression in TB medium at 30 °C. **(C)** Auto-induced expression in ZY-CAIM at 18 °C. Each sub-block represents the sample taken at indicated time points post induction (TB medium) or post change of temperature to 18 °C (ZY-CAIM) after cell lysis and removal of cell debris and inclusion bodies.

Although the final cell density of RP after 24 h at 30 °C reaches ~13 and an increasing expression signal can be observed from 1-4h after induction, no target protein can be detected after 20 h. At 20 °C, the growth of RP seems to be affected as it only reaches a cell density of 2,4 after 24 h of expression. The highest signal intensity is found after 4 h in BL21(DE) RP at 20 °C and in Lemo21- at both temperatures. Longer expression times (>20 h) showed a decrease in signal intensity, and this signal decay was stronger at higher temperatures. While C41 and C43 showed one of the highest cell densities (12-14), no protein expression signal could be observed in these strains. Cells grown in ZY-CAIM were incubated at 37 °C and 110 rpm for 3 h before the temperature was changed to 18 °C. Expression of N-His8-hSERT was found for all tested strains when using ZY-based controlled auto induction medium (CAIM; Figure 3.4 C). Overexpression started for all tested strains within the first 3 h of incubation at 37 °C. The highest signal intensity can be observed for C43 after 4 h and for Lemo21 in absence of L-rhamnose from 4-24 h after temperature change. The overall shape of the corresponding growth curves is similar for all tested strains with a final cell density of ~12 (Lemo21+, Lemo21-), ~13 (C41, C43) and ~14 (RP).

3.2.1.3 Expression analysis of N-His$_8$-hSERT in presence of chemical chaperones

Expression of N-His$_8$-hSERT was tested in *E. coli* BL21(DE3) RP, C43 and Lemo21 in presence (+) or absence (-) of 1 M sorbitol and 250 mM betaine [218,219]. Cells were grown at 37 °C in dYT or TB medium to an OD_{600} of ~0,6. Next, temperature was reduced to 21 °C and protein expression was induced by adding 0.4 mM IPTG. Cultures were harvested after 2 h of expression. Cells grown using ZY-based CAIM were inoculated to an OD_{600} of 0.05 and incubated at 37 °C for 3 h. Temperature was reduced to 18 °C and incubation continued for another 21 h before cultures were harvested (10.000 × g; 10 min). The resulting cell pellets were resuspended in 20 mL ice-cold Lysis buffer (Table 2.9) and incubated at 4 °C for 1 h. Following homogenization, cells were lysed by sonication (5x 1 min, 50 % pulse) and cell debris and inclusion bodies were removed by sedimentation (10.000 g, 10 min). Samples for SDS-PAGE were prepared from lysate after sonication as well as from supernatant and pellet after sedimentation and normalized according to their specific cell pellet weight (5 mg cells per lane). Following SDS-PAGE (2.2.2.4.2) and subsequent Western Blot transfer (2.2.2.4.3), expression of His-hSERT was detected with α-Penta-His antibody (Figure 3.5).

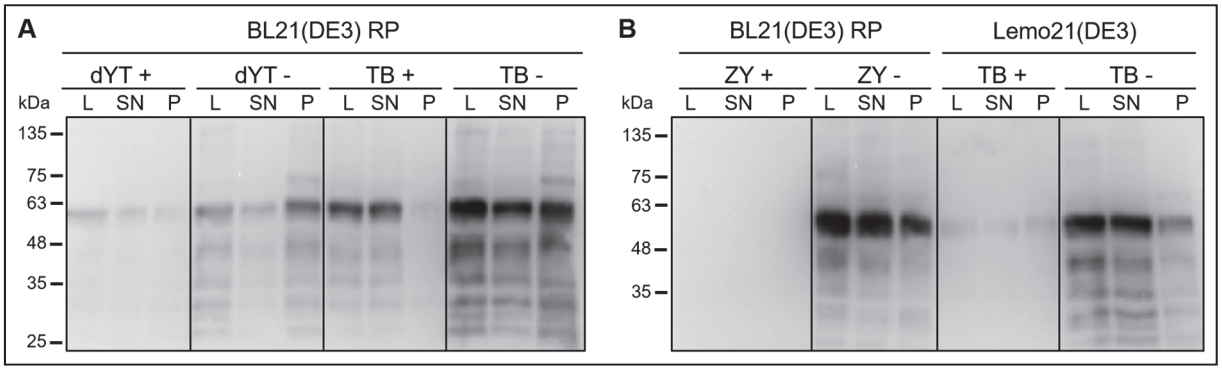

Figure 3.5: Expression analysis of N-His$_8$-hSERT in different strains of *E. coli* grown in presence of sorbitol and betaine. Immunodetection with α-His antibody. Cells from E. coli BL21(DE3) RP and Lemo21 were grown in dYT, TB or ZY-CAI medium in presence (+) or absence (-) of 1 M sorbitol and 250 mM betaine. L: lysate, S: supernatant, P: pellet

Initial analysis revealed no expression for Lemo21 grown in dYT medium and ZY-CAIM and for C43 in all tested media. These conditions were therefore excluded from further analysis. Expression of His-hSERT in BL21(DE3) RP was found for all tested conditions except for ZY-CAIM+. The strongest expression signal is always found in absence of the molecular chaperones (TB- and ZY- for RP; ZY- for Lemo21). Among these three conditions, the combination of RP/ZY- produces the highest signal intensity. In general, it seems that the presence of Sorbitol and Betaine strongly decreases the expression yield of the target protein.

From all different combinations that were grown in presence of molecular chaperones, only RP/TB+ produced amounts of His-hSERT comparable to the established expression protocol.

3.2.2 Expression of hSERT fusion protein in *S. frugiperda*

3.2.2.1 Expression analysis of C-Rho-hSERT in *S. frugiperda*

Test expression for construct p4bv-hSERT (Table 2.3) in IPLB-SF-9AE cells (Sf9; Table 2.1) was carried out by Barbara Maertens at Cube Biotech (Monheim). Baculovirus DNA containing the gene of interest under control of late p6.9 promoter was generated as described (2.2.1.2.2) and virus was replicated over two generations to produce a high titer virus stock. Cells were co-transfected at a density of 2 × 10^6 cells mL^{-1} in a volume of 3 mL suspension culture with three different ratios between Sf9 cells and virus particles (multiplicity of infection, MOI), 1, 2 and 5, respectively. Cells were incubated at 28 °C as a suspension culture until 50 h post infection. Samples of 100 µL were taken at 20, 29, 44 and 50 h post infection and cells were collected by sedimentation (300 × g, 10 min.) Samples for SDS-PAGE were prepared from the cell pellet resuspended in 100 µL PBS. Expression of Rho-hSERT was immunodetected with α-Rho1D4 antibody after SDS-PAGE (2.2.2.4.2) and subsequent Western Blot transfer (2.2.2.4.3) as shown in Figure 3.6.

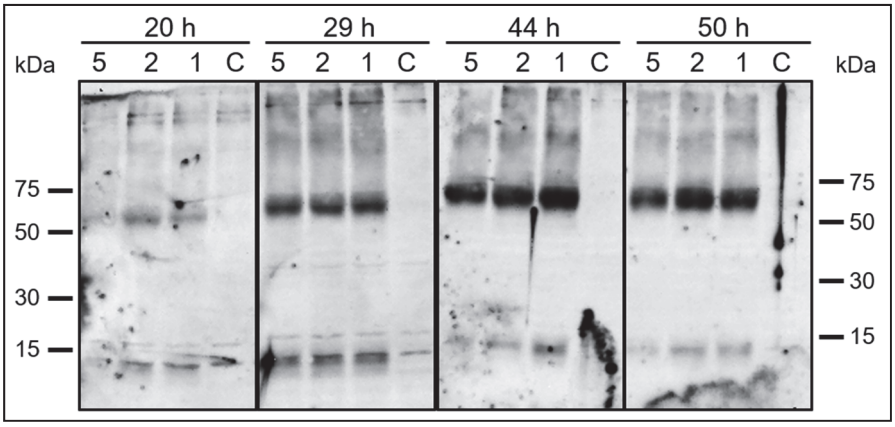

Figure 3.6: Expression analysis of C-Rho-hSERT in Sf9 cells. Immunodetection with α-Rho1D4 antibody. Cells were transfected using three different MOIs (1, 2 and 5). Non-infected cells were used as a control experiment (C). Samples were taken at indicated time points post transfection and represent the fraction after cell lysis.

Expression of Rho-hSERT was observed for all tested MOIs and the signal intensities among different MOIs at certain time points are similar. Considering the signal intensities among different time points, the maximum signal intensity is found 44 h post infection. Compared to the signal intensity of the full-length protein with an apparent MW of ~64 kDA, the amount of hSERT degradation products is relatively small.

3.2.2.2 Expression analysis of C-His$_8$-hSERT in *S. frugiperda*

Test expression for His-hSERT/pTriEx-4 in IPLB-SF-9AE cells (Sf9; Table 2.1) was carried out by Barbara Maertens at Cube Biotech (Monheim). Baculovirus DNA containing the gene of interest under control of very late p10 promoter was generated as described (2.2.1.2.2) and virus was replicated over two generations to produce a high titer virus stock. Cells were co-transfected at a density of 2 × 10^6 cells mL^{-1} in a volume of 3 mL suspension culture with three different ratios between Sf9 cells and virus particles (multiplicity of infection, MOI), 1, 2 and 5, respectively. Cells were incubated at 28 °C as a suspension culture until 50 h post infection. Samples of 100 µL were taken 20, 29, 44 and 50 h post infection and cells were collected by sedimentation (300 × g, 10 min.) Samples for SDS-PAGE were prepared from the cell pellet resuspended in 100 µL PBS. Expression of His-hSERT was immunodetected with α-His antibody after SDS-PAGE (2.2.2.4.2) and subsequent Western Blot transfer (2.2.2.4.2) as shown in Figure 3.7.

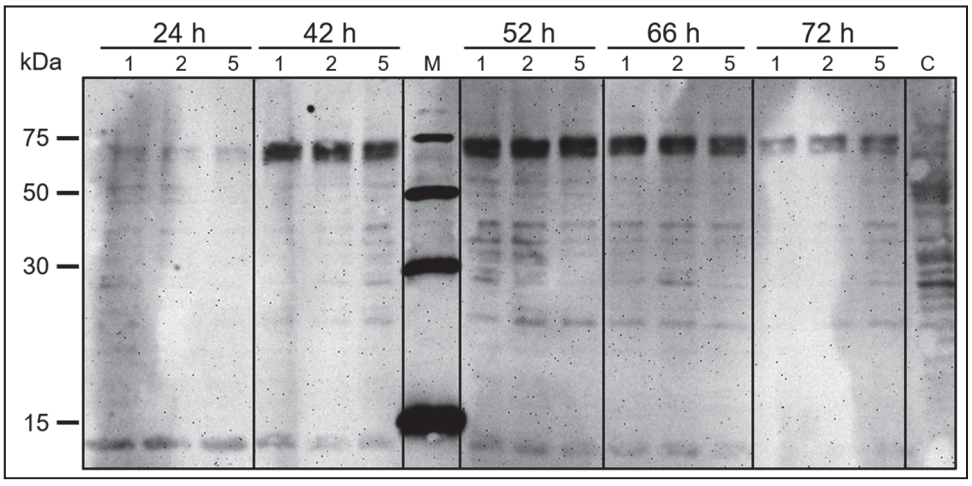

Figure 3.7: Expression analysis of C-His$_8$-hSERT in Sf9 cells. Immunodetection with α-His antibody. Cells were transfected using three different MOIs (1, 2 and 5). Non-infected cells were used as a control experiment (C). Samples were taken at indicated time points post transfection and represent the fraction after cell lysis.

Expression of His-hSERT was be observed for all tested MOIs and the intensity of expression signal among different MOIs at certain time points is similar. Considering the signal intensities among different time points, the maximum signal intensity is found 52 h post infection. Longer infection times showed a reduced signal intensity of full-length hSERT. Compared to construct p4bv-hSERT (3.2.2.1), the amount and of hSERT degradation products is higher.

3.3 Purification of *E. coli* expressed hSERT

3.3.1 Solubilization of *E. coli* expressed hSERT

3.3.1.1 Detergent screening for solubilization of N-His_8-hSERT

Membrane for solubilization screening experiments was prepared (2.2.2.2.1) from *E. coli* BL21(DE3) RP cells grown in ZY-based autoinduction medium at 18 °C (2.2.1.1.3).

First, the efficiency of different detergents to solubilize His-hSERT from E. coli derived membrane was tested. The range of screened detergents includes non-ionic detergents (LMNG, DMNG, Cymal-6, NG, DM, DDM, β-OG, OTG) as well as zwitterionic detergents (FC12, FC14, FC16, LDAO). The total protein concentration of the membrane suspension was diluted with detergent-free Solubilization buffer (Table 2.9) to 1 mg mL^{-1} and detergent was added to a final concentration of 1 % (w/v). Samples of 1 mL were incubated over night at 4 °C with gentle agitation. Supernatant after pellet sedimentation (100.000 × g; 1 h; 4 °C) was collected and the pellet was washed twice with PBS and then dissolved in the same volume of Solubilization buffer with 1 % SDS and 6 M Urea. Samples for SDS-PAGE (2.2.2.4.2) were prepared from supernatant and resolubilized pellet fraction, His_8-hSERT was immunodetected with α-His antibody following Western Blot transfer (2.2.2.4.3; Figure 3.8).

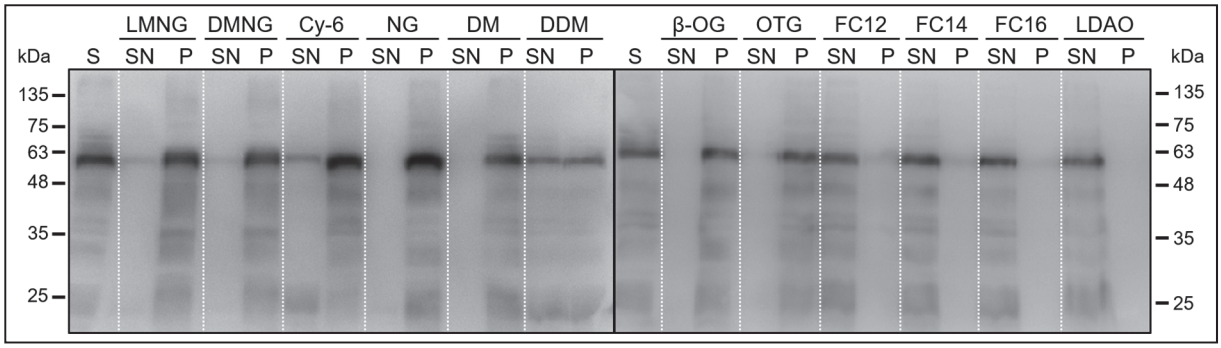

Figure 3.8: Detergent screening for solubilization of N-His_8-hSERT. Immunodetection with α-His antibody. Samples were taken from supernatant and resolubilized pellet fraction after sedimentation at 100.000 × g for 1 h. M: marker; S: membrane suspension; SN: supernatant; P: pellet; LMNG: Lauryl maltose neopentyl glycol; DMNG: Decyl maltose neopentyl glycol; Cy-6: 6-Cyclohexyl-1-hexyl-β-D-maltoside; NG: n-Nonyl-β-D-glucopyranoside; DM: n-Decyl-β-maltoside; DDM: n-Dodecyl-β-D-maltoside; ß-OG: n-Octyl-β-D-glucopyranoside; OTG: n-Octyl-β-D-thioglucopyranoside; FC12: n-Dodecyl-phosphocholine; FC14: n-Tetradecyl-phosphocholine; FC16: n-Hexadecyl-phosphocholine; LDAO: n-Dodecyl-N,N-dimethylamine

The highest efficiency for solubilization of His-hSERT is found among all tested zwitterionic detergents (FC12, FC14, FC16, LDAO), more than 95 % of the target protein is in the soluble fraction (SN) while the rest remains within the pellet fraction (P). All tested non-ionic detergents can solubilize only a small amount (LMNG, DMNG, Cy-6) or no target protein at all (NG, DM,

β-OG, OTG), except for DDM, which can solubilize up to 50 % of His_8-hSERT. All samples show a similar degradation band pattern.

Next, solubilization conditions for FC12 were further optimized by screening both the detergent concentration (0.3-1.0 % (w/v)) as well as the incubation period (1-12 h). Additionally, the total protein concentration of the membrane suspension was adjusted to 2 mg mL^{-1}, resulting in a lower micelle:protein ratio compared to the previous experiment. The suspension was incubated with either 0.3 %, 0.6 % or 1.0 % (w/v) FC12 for 12 h at 4 °C with gentle agitation and 1mL samples were taken after certain time points (1, 2, 4, 12 h). The supernatant after pellet sedimentation (100,000 × g; 1 h; 4 °C) was collected and the pellet was washed twice with PBS and then dissolved in the same volume of Solubilization buffer with 1 % (w/v) SDS and 6 M Urea. Samples for SDS-PAGE (2.2.2.4.2) were prepared from supernatant and resolubilized pellet fraction, His_8-hSERT was immunodetected with α-His antibody following Western Blot transfer (2.2.2.4.3; Figure 3.9).

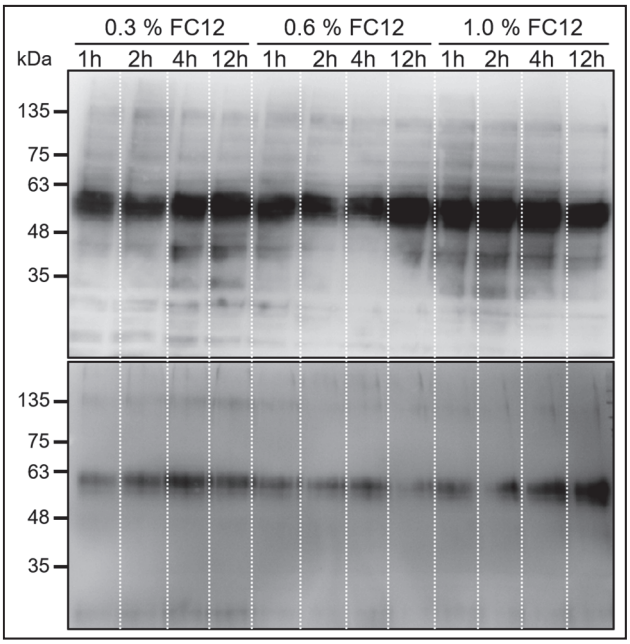

Figure 3.9: Screening for optimal solubilization condition for N-His_8-hSERT by varying duration of solubilization and FC12 concentration. Immunodetection with α-His antibody. Samples were taken after 1, 2, 4 and 12 h. After ultracentrifugation at 100.000 × g for 1 h, samples for SDS-PAGE were prepared from supernatant (top) and resolubilized pellet (bottom) fraction.

All samples contained the majority of His-hSERT within the soluble fraction, with the highest signal intensity after 2-4 h solubilization with 1 % (w/v) FC12. Nonetheless, a small amount of target protein is also found within the insoluble pellet fraction. Compared to the previous screening (Figure 3.8), the fraction of insoluble His-hSERT seems to be greater, indicating that the chosen micelle:protein ratio is not sufficient for complete solubilization.

3.3.2 Purification of N-His_8/C-Rho-hSERT with immobilized ligand affinity matrix

Target protein hSERT was expressed as either C-terminal Rho-tagged or N-terminal His-tagged fusion protein (2.2.1.1.3) in *E. coli* C43 or RP, respectively, and membrane was prepared from cells as described (2.2.2.2.1).

C-Rho-hSERT was solubilized with 1.0 % (w/v) FC12 in Solubilization buffer (126 mM NaCl; 2.7 mM KCl; 10 mM NaH_2PO_4; 1.76 mM KH_2PO_4; 10 % (v/v) Glycerol; 1x PIC; pH 7.4) for 2 h at a total membrane protein concentration of 2 mg mL^{-1}. The resulting supernatant after sedimentation (100,000 × g, 4 °C, 1 h) was incubated over night with serotonin agarose or Rho-1D4 agarose (Cube Biotech, Monheim) at a sample to resin volume ratio of 50:1. Bound resin was washed with 30 CV wash buffer (126 mM NaCl; 2.7 mM KCl; 10 mM NaH_2PO_4; 1.76 mM KH_2PO_4; 10 % (v/v) Glycerol; 1x PIC; 0.1 % (w/v) FC12; pH 7.4) and target protein was eluted with 5 CV serotonin elution buffer (100 mM Glycine; 1 mM TCEP; 10 % (w/v) Glycerol; 0.1 % (w/v) FC12; pH 2.7) or with 5 CV Rho elution buffer (126 mM NaCl; 2.7 mM KCl; 10 mM NaH_2PO_4; 1.76 mM KH_2PO_4; 10 % (v/v) Glycerol; 0.1 % (w/v) FC12; 200 µM Rho peptide; pH 7.4).

N-His_8-hSERT was solubilized with 1.0 % (w/v) FC12 in Solubilization buffer (Table 2.9) for 2 h at a total membrane protein concentration of 2 mg mL^{-1}. The resulting supernatant after sedimentation (100,000 × g, 4 °C, 1 h) was incubated over night with fluoxetine, desipramine or serotonin agarose (Cube Biotech, Monheim) at a sample to resin volume ratio of 10:1. Resin was washed with 5 CV Solubilization buffer and target protein was eluted with 5 CV Solubilization buffer at pH 2.7. The pH of elution fractions was immediately adjusted to 7.

Samples for SDS-PAGE (2.2.2.4.2) were prepared from flow through (FT), wash (W) and elution (E) fractions and hSERT was immunodetected with either α-Rho or α-His antibody following Western Blot transfer (2.2.2.4.3; Figure 3.10).

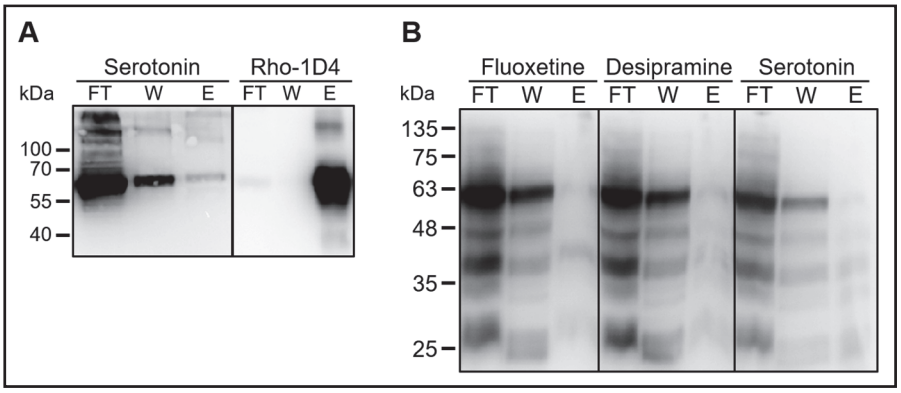

Figure 3.10: Analysis of hSERT purification with immobilized ligand affinity matrix. Immunodetection with α-Rho1D4 (A) or α-His (B) antibody. **(A)** C-Rho-hSERT purified with Serotonin or Rho-1D4 agarose. **(B)** N-His_8-hSERT purified with fluoxetine, desipramine or serotonin agarose. FT: flow through; W: wash; E: elution

A small fraction of Rho- or His-tagged hSERT is in the elution fraction of the tested ligand affinity resin, while most of the target protein is found in the flow through and wash fraction. In contrast to that, Rho-hSERT is almost exclusively found in the elution fraction and only a faint signal is found in the corresponding flow through fraction while the washing fraction appeared to be free from protein. The yield of Rho-1D4 purified hSERT was estimated as 30 µg g^{-1} cell pellet.

3.3.3 Purification of C-Rho-hSERT fusion protein

3.3.3.1 Immobilized antibody affinity purification of C-Rho-hSERT

Target protein hSERT was expressed as C-terminal Rho-tagged fusion protein (2.2.1.1.3) in *E. coli* C43. Following membrane preparation (2.2.2.2.1) and membrane solubilization (2.2.2.2.2), Rho-hSERT was purified by antibody affinity chromatography (2.2.2.2.3). Samples were taken from different stages during the purification process and analyzed by antibody immunodetection after SDS-PAGE (2.2.2.4.2) and Western blot (2.2.2.4.3; Figure 3.11).

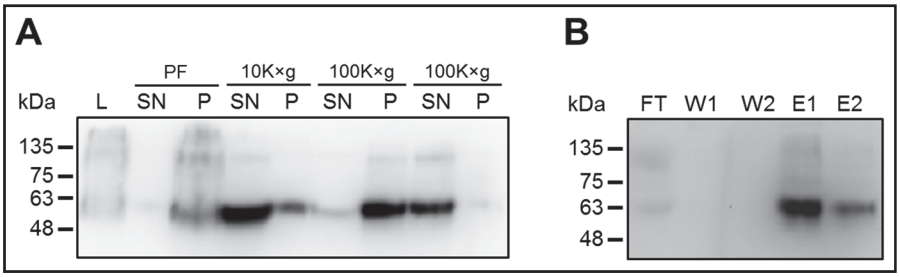

Figure 3.11: Western blot analysis of C-Rho-hSERT purification. Immunodetection with α-Rho antibody. **(A)** Samples from cell lysis, membrane preparation and solubilization. **(B)** Samples from Rho-1D4 affinity chromatography. L: lysate PF: periplasmic fraction; SN: supernatant; p: pellet; FT: flow through; W1, W2: wash; E1, E2: elution

Panel A in Figure 3.11 shows the samples taken during removal of periplasmic fraction, cell lysis, membrane preparation and membrane solubilization. After removal of periplasmic fraction (PF) and subsequent sedimentation at 100,000 × g, the target protein is predominantly found in the supernatant (SN) while a small fraction of Rho-hSERT remains within the cell pellet (P), indicating that the *E. coli* cells were not completely lysed. The membrane fraction was collected from the supernatant after centrifugation at 100,000 × g and the majority of hSERT is found in the membrane pellet, while only a small fraction of hSERT remains in the soluble fraction. Following FC12 mediated solubilization and sedimentation of membrane pellet, Rho-hSERT can be detected in the soluble fraction almost exclusively, leaving only a small fraction of membrane bound hSERT in the pellet fraction. Panel B in Figure 3.11 shows the samples taken during the antibody affinity purification. After binding over night to the

antibody matrix, only a weak signal is found in the flow through and the washing fraction appeared to be free of protein while the majority of Rho-hSERT is found in the elution fraction. No degradation products of hSERT were found through immunodetection. Protein amount of combined elution fractions was determined by UV measurement (2.2.2.4.1) and the yield of Rho-hSERT was calculated as 70 µg g^{-1} cell pellet.

3.3.3.2 Size exclusion purification of C-Rho-hSERT

Following antibody affinity purification (2.2.2.2.3), Rho-hSERT elution fraction was subjected to size exclusion chromatography (2.2.2.2.5) to separate different protein species based on their size. The protein sample was concentrated and filtered before loading to the sample loop. The sample was eluted over 1 CV (24 mL) at a flow rate of 0.25 mL min^{-1} in fractions of 0.5 mL volume. The chromatogram as well as the corresponding SDS-PAGE (2.2.2.4.2) and Western blot (2.2.2.4.3) analysis is shown in Figure 3.12.

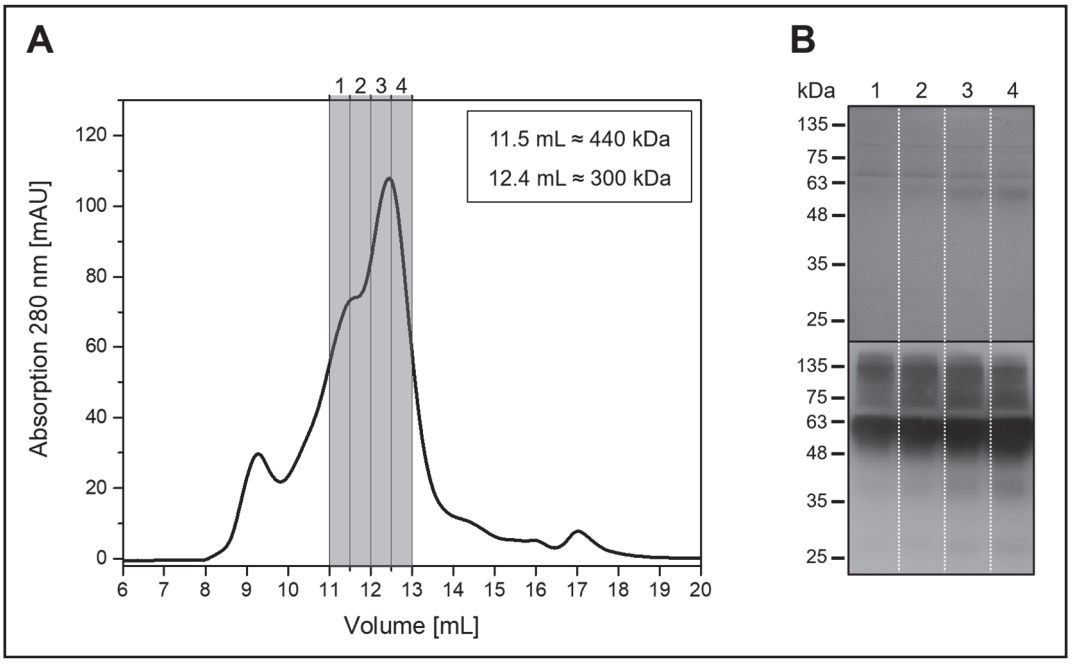

Figure 3.12: Size exclusion chromatography of Rho-hSERT with 0.1 % (w/v) FC12. **(A)** Elution profile of C-Rho-hSERT using Superdex 200 10/300 GL column. **(B)** Blue-silver stained SDS-PAGE (top) and Western blot after α-Rho immunodetection (bottom) of indicated SEC fractions (1-4).

The elution profile (Figure 3.12 A) shows two different peaks that are not very well separated. The first peak with an elution volume of 11.5 mL (Fraction 1-2) corresponds to a MW of ~440 kDa. As shown in the Western Blot (Figure 3.12 B, lower panel), this fraction contains Rho-hSERT, that runs shortly below 63 kDa as well as higher aggregated forms of hSERT. The blue-silver stained SDS-PAGE (Figure 3.12 B, upper panel) reveals a second

protein band, that runs between 75 and 63 kDa and is not detected by α-Rho antibody. This band is also found in the second peak around 12.5 mL (~300 kDa; Fraction 3-4), where the highest intensity of Rho-hSERT is detected, and it appears to co-elute with Rho-hSERT. Furthermore, degradation products of hSERT are found above 35 and 25 kDa with increasing intensity towards higher elution volumes. The protein yield for peak 1 and peak 2 was estimated as ~ 10 µg/g cell pellet and ~ 30 µg/g cell pellet, respectively.

3.3.3.3 Mass spectroscopic analysis of purified C-Rho-hSERT

Protein band after blue-silver stained SDS-PAGE was excised from gel and submitted to EBML SPC (Hamburg) for protein identification through mass spectrometry. Identified peptide fragments were compared to the provided protein sequence. A graphical representation of the results is shown in Figure 3.13.

1	METTPLNSQK	QLSACEDGED	CQENGVLQKV	VPTPGDKVES	GQISNGYSAV	PSPGAGDDTR
61	HSIPATTTTL	VAELHQGERE	TWGKKVDFLL	SVIGYAVDLG	NVWRFPYICY	QNGGGAFLLP
121	YTIMAIFGGI	PLFYMELALG	QYHRNGCISI	WRKICPIFKG	IGYAICIIAF	YIASYYNTIM
181	AWALYYLISS	FTDQLPWTSC	KNSWNTGNCT	NYFSEDNITW	TLHSTSPAEE	FYTRHVLQIH
241	RSKGLQDLGG	ISWQLALCIM	LIFTVIYFSI	WKGVKTSGKV	VWVTATFPYI	ILSVLLVRGA
301	TLPGAWRGVL	FYLKPNWQKL	LETGVWIDAA	AQIFFSLGPG	FGVLLAFASY	NKFNNNCYQD
361	ALVTSVVNCM	TSFVSGFVIF	TVLGYMAEMR	NEDVSEVAKD	AGPSLLFITY	AEAIANMPAS
421	TFFAIIFFLM	LITLGLDSTF	AGLEGVITAV	LDEFPHVWAK	RRERFVLAVV	ITCFFGSLVT
481	LTFGGAYVVK	LLEEYATGPA	VLTVALIEAV	AVSWFYGITQ	FCRDVKEMLG	FSPGWFWRIC
541	WVAISPLFLL	FIICSFLMSP	PQLRLFQYNY	PYWSIILGYC	IGTSSFICIP	TYIAYRLIIT
601	PGTFKERIIK	SITPETPTEI	PCGDIRLNAV	GSSGTETSQV	APAG	

Figure 3.13: Peptides identified by LC-MS/MS analysis of C-Rho-hSERT. Underlined: transmembrane regions; red: identified sequence.

The full-length sequence of C-terminal Rho-tagged hSERT in Figure 3.13 is represented as single-letter amino acid code. Transmembrane regions of the protein are underlined while the identified sequence is represented with red letters. The identified sequences are located towards the N-terminal and the C-terminal end of the protein and include the transmembrane domains 1, 9 and 11. The overall sequence coverage is 30.6 %.

3.3.4 Purification of N-His8-hSERT fusion protein

3.3.4.1 Immobilized metal affinity purification of N-His-hSERT

Target protein hSERT was expressed as N-terminal His_8-tagged fusion protein (2.2.1.1.3) in *E. coli* BL21(DE3) RP. Following membrane preparation (2.2.2.2.1) and membrane solubilization (2.2.2.2.2) with 0.1 % (w/v/) FC12 or 0.02 % (w/v) DDM, N-His_8-hSERT was purified by immobilized metal affinity chromatography (IMAC; 2.2.2.2.3). Samples were taken from different stages during the purification process and analyzed through antibody immunodetection after SDS-PAGE (2.2.2.4.2) and subsequent Western blot transfer (2.2.2.4.3). Results of Coomassie blue-silver stained SDS-PAGE (top panel) and α-His immunodetection Western blot (bottom panel) analysis are shown in Figure 3.14.

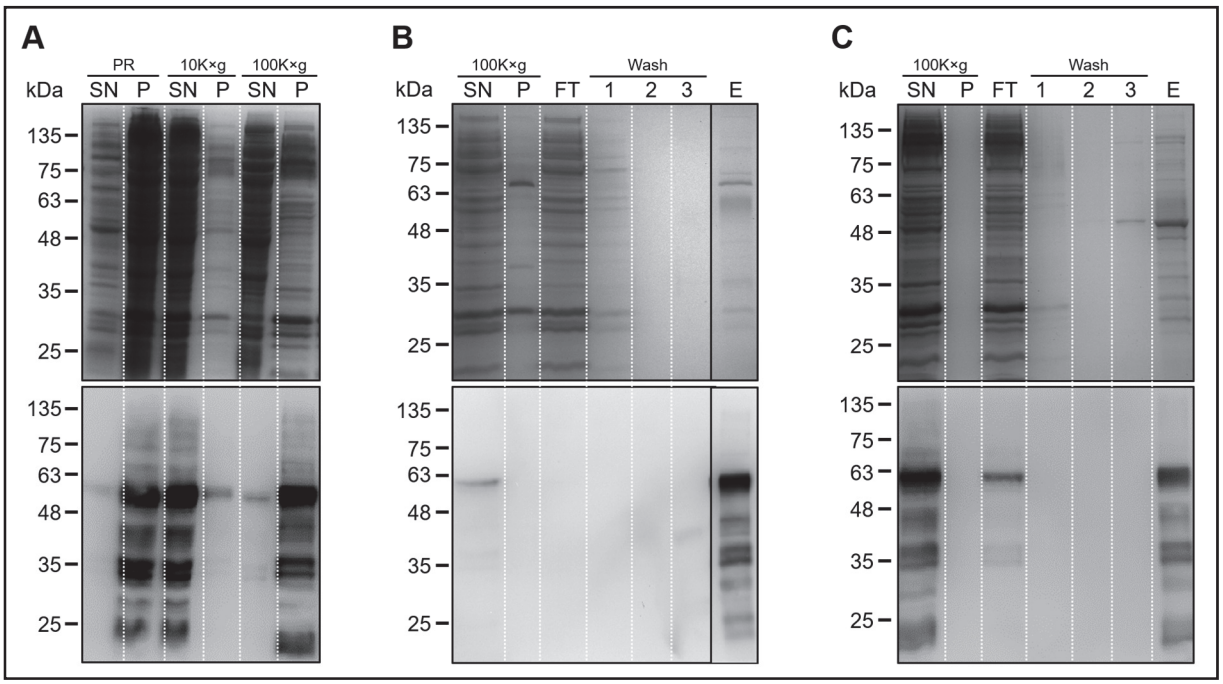

Figure 3.14: SDS-PAGE and Western blot analysis of N-His_8-hSERT IMAC purification. Top: Coomassie blue-silver stained SDS-PAGE. Bottom: Western blot with α-His antibody immunodetection. **(A)** Sample from cell lysis, membrane preparation and solubilization. **(B)** Samples from IMAC of N-His_8-hSERT with FC12. **(C)** Samples from IMAC of N-His_8-hSERT with DDM. PR: periplasmic removal; SN: supernatant; P: pellet; FT: flow through; E: elution

Panel A in Figure 3.14 shows the samples taken during periplasmic removal, cell lysis, membrane preparation and membrane solubilization. After removal of the periplasmic fraction (PR) and subsequent sedimentation of cell debris at 10,000 × g, the target protein is predominantly found in the supernatant (SN) while a small fraction of His-hSERT remains within the cell pellet (P), indicating that the *E. coli* cells were not completely lysed. The membrane fraction was collected from the supernatant after centrifugation at 100,000 × g and the majority of hSERT is found in the membrane pellet, while only a small fraction of hSERT

remains in the soluble fraction. Following FC12 (Figure 3.14 B) or DDM (Figure 3.14 C) mediated solubilization and sedimentation of membrane pellet at 100,000 × g, His-hSERT is exclusively found in the soluble fraction, and no trace of His-hSERT is detected in the remaining membrane pellet fraction. After incubation with Ni-NTA matrix, the flow through and wash fractions for FC12 purified hSERT do not contain a detectable concentration of target protein, whereas the DDM purified hSERT does not fully bind to the matrix and a fraction of hSERT is found in the flow through. Several impurities could be removed during the washing steps, but the final elution fractions still contain impurities and degradation products. Although N-His-hSERT shows a characteristic degradation band pattern, that can be immunodetected throughout the purification process, the band pattern for foreign proteins is partially different between FC12 and DDM purified hSERT. The FC12 purified sample contains a sharp band between 75 and 63 kDa which is not present in the DDM purified sample. In contrast to that, the DDM purified elution sample contains an impurity band that runs immediately below hSERT at a MW of ~50 kDa, which is not present within the FC12 purified sample. The purity of elution fractions was determined through densitometry measurement with Image Lab [169] and ranges from ~25 % (DDM) to 50 % (FC12). Protein amount of combined elution fractions was determined by UV measurement (2.2.2.4.1) and the total yield of His-hSERT was calculated as 500 µg/g cell pellet (both DDM and FC12) after IMAC.

3.3.4.2 Ion exchange purification of N-His-hSERT

Following IMAC purification (2.2.2.2.3), hSERT was further purified using ion exchange chromatography (IEC; 2.2.2.2.4). Therefore, His_8-hSERT elution fractions were combined and diluted with IEC dilution buffer (Table 2.9) to reduce the salt concentration to 50 mM NaCl (final run: 25 mM NaCl). The diluted sample was loaded onto a Q-Agarose column (Cube Biotech, Monheim) and protein fractions were eluted with a NaCl step gradient. Samples were taken from flow through, wash and elution fractions during the purification process and analyzed through antibody immunodetection after SDS-PAGE (2.2.2.4.2) and subsequent Western blot transfer (2.2.2.4.3). Results of this analysis along with the corresponding chromatogram for FC12 and DDM purified His-hSERT are shown in Figure 3.15.

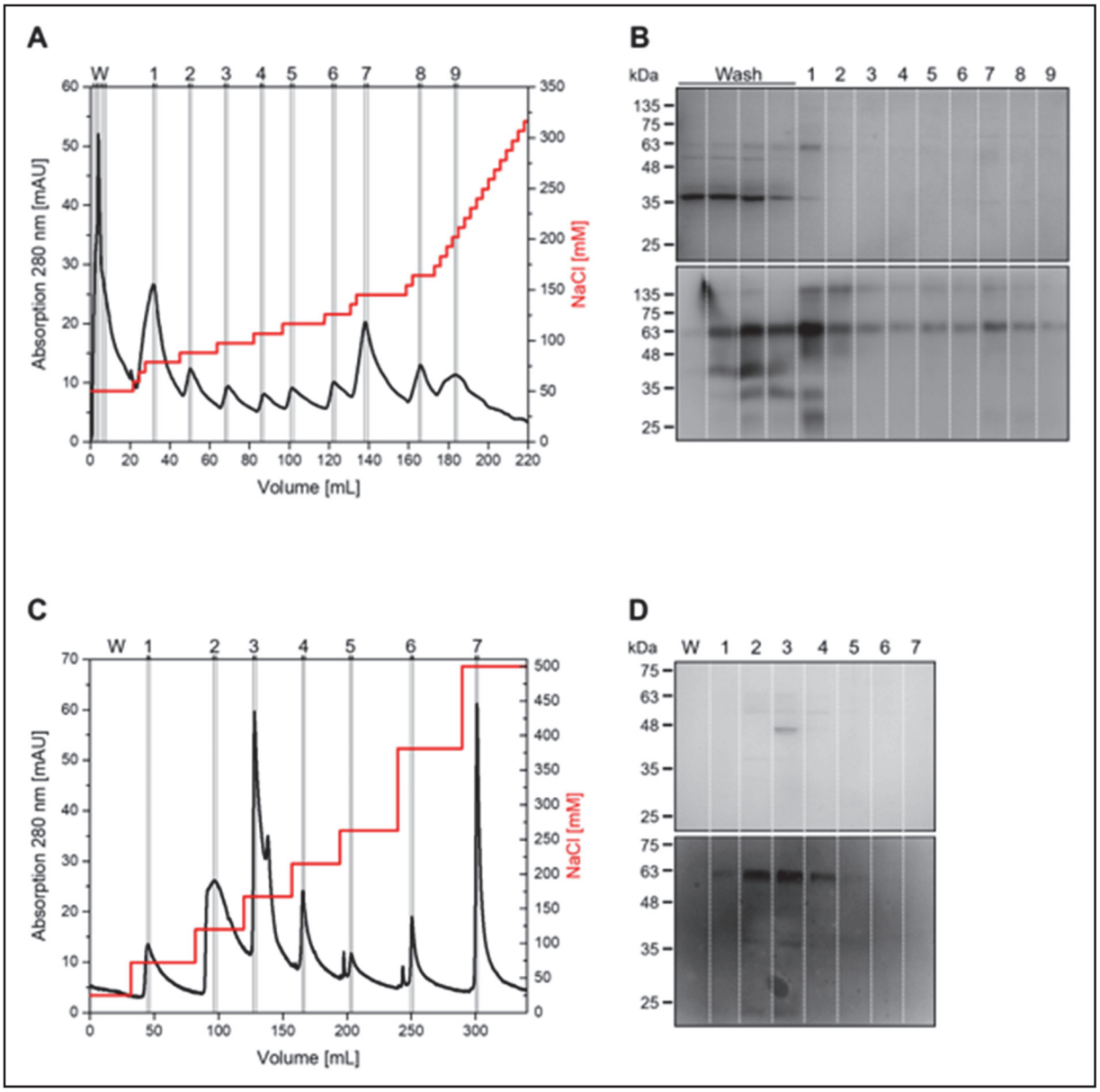

Figure 3.15: SDS-PAGE and Western blot analysis of His-hSERT IEC purification. **(A)** Elution profile of FC12 purified N-His_8-hSERT with NaCl gradient from 50 to 500 mM. **(B)** Coomassie blue-silver stained SDS-PAGE (top) and Western blot with α-His antibody immunodetection (bottom) for fractions corresponding to FC12 purified N-His_8-hSERT. **(C)** Elution profile of DDM purified hSERT with NaCl gradient from 25 to 500 mM. **(D)** Coomassie blue-silver stained SDS-PAGE (top) and Western blot with α-His antibody immunodetection (bottom) for fractions corresponding to DDM purified N-His_8-hSERT.

After binding of FC12 purified hSERT to Q-agarose, the resin was washed with the same buffer that was used during sample loading (Figure 3.15 A). This washing step led to an increased absorption at 280 nm of ~ 50 mAU. The Coomassie blue-silver stained SDS-PAGE (Figure 3.15 B, top panel) shows, that these fractions contain at least two foreign protein bands with an apparent MW of ~38 and ~50 kDa, respectively. The protein band around ~63 kDa was confirmed from the Western blot (Figure 3.15 B, bottom panel) to be His-hSERT and is also found in the washing fractions. In general, a signal for His-hSERT is found in every peak

fraction during the step gradient elution, with the highest signal intensity in fraction 1, which was eluted using 78.5 mM NaCl. This fraction still contains a contamination of a ~38 kDa protein, which could not be removed completely during the washing step. Since this fraction contains most of the target protein, it was used for further purification through SEC.

After binding of DDM purified hSERT to Q-agarose, the resin was washed with the same buffer that was used during sample loading (Figure 3.15 C). No increased absorption at 280 nm was observed and washing fraction appears to be free from unbound protein (Figure 3.15 D). The target protein is found throughout elution fractions 1-5, with the highest signal intensity in fraction 2 and 3. These fractions were eluted at a NaCl concentration of 120 mM and 167.5 mM, respectively. Both fractions also contain degradation products of hSERT shortly above 35 and below 25 kDa. The signal intensity for His-hSERT after immunodetection in these two fractions is similar, although the absorption at 280 nm for fraction 3 is more than twice as high compared to that of fraction 2. The higher absorption of fraction 3 is caused by a protein contamination, which is visible as a double band around 48 kDa in the Coomassie blue-silver stained SDS-PAGE (Figure 3.15 D, top panel). Since fraction 2 has a higher purity compared to fraction 3, it was used for further purification through SEC.

3.3.4.3 Size exclusion purification of N-His_8-hSERT

Following IMAC (2.2.2.2.3) or IEC (2.2.2.2.4) purification, His_8-hSERT elution fraction was subjected to size exclusion chromatography (2.2.2.2.5) to separate different protein species based on their hydrodynamic radius. The protein sample was concentrated and filtered before loading to the sample loop. His-hSERT purified with FC12 or DDM was eluted over 1 CV (120 mL) at a flow rate of 0.2 mL min^{-1} in fractions of 0.5 mL volume. His-hSERT purified with FC14 was eluted over 1 CV (120 mL) at a flow rate of 0.3 mL min^{-1} in fractions of 0.5 mL volume. The chromatogram as well as the corresponding SDS-PAGE and Western blot analysis is shown in Figure 3.16

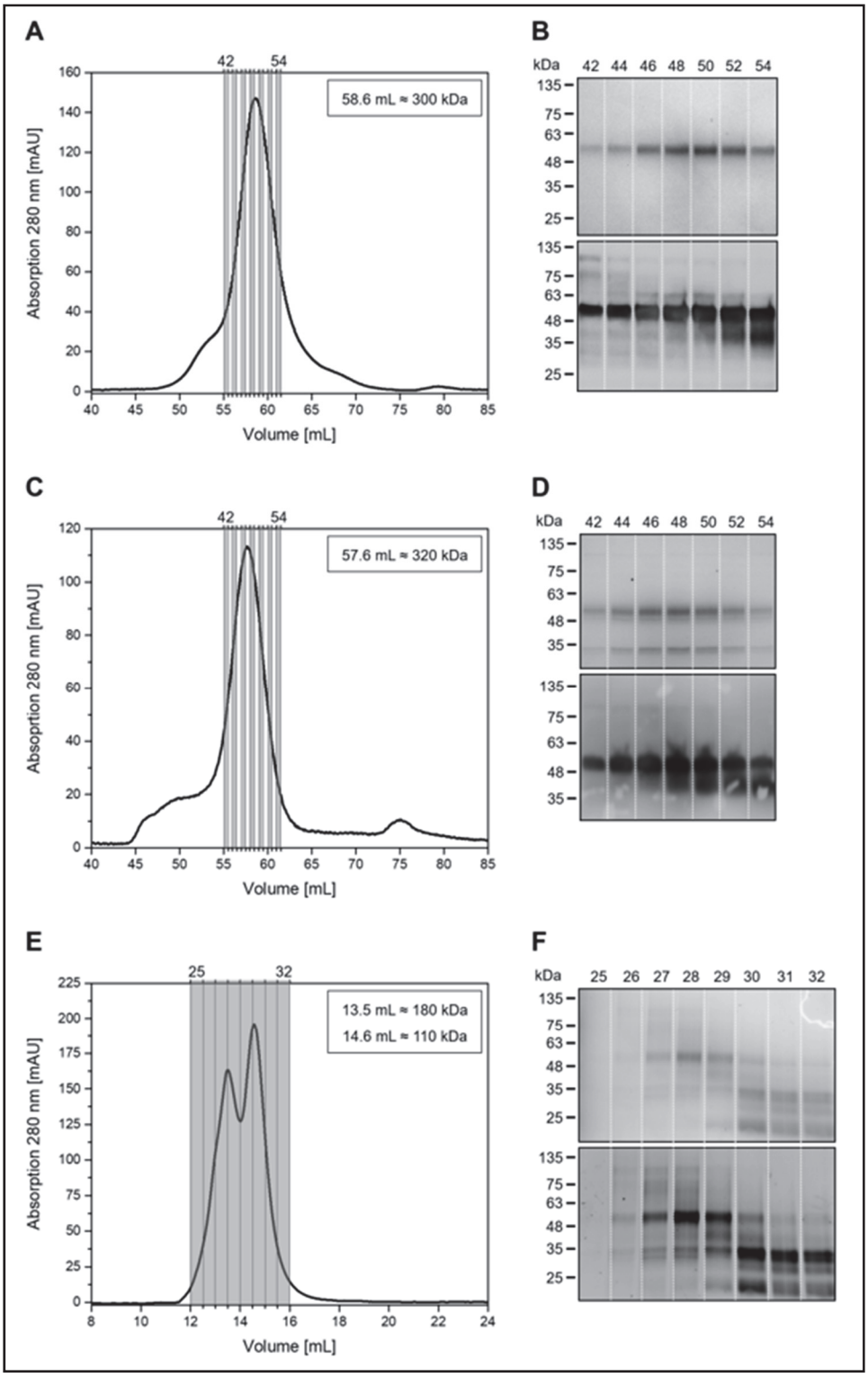

Figure 3.16: Size exclusion chromatography of N-His_8-hSERT with different detergents. **(A)** Elution profile of N-His_8-hSERT with 0.1 % FC12 using Superdex 200 16/60 PG column. **(B)** Coomassie blue-silver stained SDS-PAGE (top) and Western blot with α-His immunodetection (bottom) of N-His_8-hSERT with 0.1 % FC12 for indicated SEC fractions (42-54). **(C)** Elution profile of N-His_8-hSERT with 0.02 % DDM using Superdex 200 16/60 PG column. **(D)** Coomassie blue-silver stained SDS-PAGE (top) and Western blot with α-His immunodetection (bottom) of N-His_8-hSERT with 0.02 % DDM for indicated SEC fractions (42-54). **(E)** Elution profile of N-His_8-hSERT with 0.1 % FC14 using Superdex 200 16/60 PG column. **(F)** Coomassie blue-silver stained SDS-PAGE (top) and TGX stain-free SDS-PAGE (bottom) of N-His_8-hSERT with 0.1 % FC14 for indicated SEC fractions (25-32).

The elution profile of FC12 purified hSERT showed a single peak with an elution volume of 58.6 mL, which corresponds to an apparent MW of ~297 kDa (Figure 3.16 A). This size could be explained as the tetrameric form of hSERT along with a single FC12 micelle (MW hSERT: ~71 kDa; MW FC12 micelle: ~19 kDa). Based on the Coomassie blue-silver stained gel for the SEC fractions, the purity of hSERT in fractions 42-54 was estimated to be >95 % (Figure 3.16 B, top panel). As it is shown in the Western blot, the fractions on the right side of the peak include degradation products of His-hSERT with increasing signal intensity towards higher elution volumes (Figure 3.16 B, bottom panel). Protein amount of combined elution fractions 44-52 was determined (2.2.2.4.1) and the yield of pure His-hSERT was estimated to be 50 µg g^{-1} cell pellet.

The elution profile of DDM purified hSERT showed a single peak as well. Compared to FC12 purified hSERT, the peak elution volume is shifted by 1 mL to 57.6 mL, which corresponds to an apparent MW of ~322 kDa (Figure 3.16 C). The difference of ~25 kDa between those two detergents cannot be solely explained by the larger size of DDM micelle (MW: ~72 kDa), which would shift the elution peak by 50 kDa instead of 25 kDa. Indeed, the SEC fractions are not homogeneous as they contain at least two other proteins, that co-elute with hSERT. The Coomassie blue-silver stained gel shows one band with an apparent MW of ~50 kDa that is running immediately below hSERT, and a second band immediately below 35 kDa (Figure 3.16 D, top panel). These contaminations will affect the peak elution volume, which is therefore less reliable in terms of estimating the oligomeric state of DDM purified hSERT. The purity of hSERT in fractions 42-54 varies between 60-70 %. Like the FC12 purified hSERT, the preparation with DDM also contains degradation products of target protein on the right side of the peak. Protein amount of combined elution fractions 44-52 was determined (2.2.2.4.1) and the yield of pure His_8-hSERT was calculated as 25 µg g^{-1} cell pellet.

The elution profile of FC14 purified hSERT showed a double peak with an elution volume of 13.5 mL and 14.6 mL, respectively. These peak elution volumes correspond to an apparent MW of ~180 kDa and ~110 kDa, respectively (Figure 3.16 E). The elution fractions appear to be free from contaminating proteins (Figure 3.16 F, top panel), but they do contain hSERT degradation products of different MW, especially in the fractions 30-32 that make up the second peak, which almost exclusively contains degraded hSERT. As described before, the co-elution of impurities makes it difficult to determine the oligomeric state of hSERT. The purity of hSERT in fractions 27-29 varies between 75-80 %. Protein amount of combined elution fractions was determined (2.2.2.4.1) and the yield of pure N-His_8-hSERT was calculated as 20 µg g^{-1} cell pellet.

3.3.4.4 Mass spectroscopic analysis of purified N-His$_8$-hSERT

Protein band after blue-silver stained SDS-PAGE was excised from gel and submitted to EBML SPC (Hamburg) for protein identification through mass spectrometry. Identified peptide fragments were compared to the provided protein sequence. A graphical representation of the results is shown in Figure 3.17.

1	HHHHHHHHME	TTPLNSQKQL	SACEDGEDCQ	ENGVLQKVVP	TPGDKVESGQ	ISNGYSAVPS
61	PGAGDDTRHS	IPATTTTLVA	ELHQGERETW	GKKVDFLLSV	IGYAVDLGNV	WRFPYICYQN
121	GGGAFLLPYT	IMAIFGGIPL	FYMELALGQY	HRNGCISIWR	KICPIFKGIG	YAICIIAFYI
181	ASYYNTIMAW	ALYYLISSFT	DQLPWTSCKN	SWNTGNCTNY	FSEDNITWTL	HSTSPAEEFY
241	TRHVLQIHRS	KGLQDLGGIS	WQLALCIMLI	FTVIYFSIWK	GVKTSGKVVW	VTATFPYIIL
301	SVLLVRGATL	PGAWRGVLFY	LKPNWQKLLE	TGVWIDAAAQ	IFFSLGPGFG	VLLAFASYNK
361	FNNNCYQDAL	VTSVVNCMTS	FVSGFVIFTV	LGYMAEMRNE	DVSEVAKDAG	PSLLFITYAE
421	AIANMPASTF	FAIIFFLMLI	TLGLDSTFAG	LEGVITAVLD	EFPHVWAKRR	ERFVLAVVIT
481	CFFGSLVTLT	FGGAYVVKLL	EEYATGPAVL	TVALIEAVAV	SWFYGITQFC	RDVKEMLGFS
541	PGWFWRICWV	AISPLFLLFI	ICSFLMSPPQ	LRLFQYNYPY	WSIILGYCIG	TSSFICIPTY
601	IAYRLIITPG	TFKERIIKSI	TPETPTEIPC	GDIRLNAV		

Figure 3.17: Peptides identified by LC-MS/MS analysis of N-His$_8$-hSERT. Underlined: transmembrane regions; ted: Identified sequence.

The full-length sequence of N-terminal His$_8$-tagged hSERT in Figure 3.17 is represented as single-letter amino acid code. Transmembrane regions of the protein are underlined while the identified sequence is represented with red letters. The identified sequences are located towards the N-terminal and the C-terminal end of the protein and include the transmembrane domains 9 and 12. The overall sequence coverage is 26.1 %.

3.4 Purification of *S. frugiperda* expressed hSERT

3.4.1 Purification of C-Rho-hSERT-Sf9 with DDM and FC12

Expression of p4bv-hSERT in Sf9 cells and membrane preparation was carried out by Barbara Maertens and Jan Kubicek at Cube Biotech (Monheim). C-terminal Rho-tagged hSERT-Sf9 was purified by antibody affinity chromatography (2.2.2.2.3) and SEC (2.2.2.2.5). Samples were taken during different stages of purification and analyzed by antibody immunodetection after SDS-PAGE (2.2.2.4.2) and subsequent Western blot transfer (2.2.2.4.3; Figure 3.18).

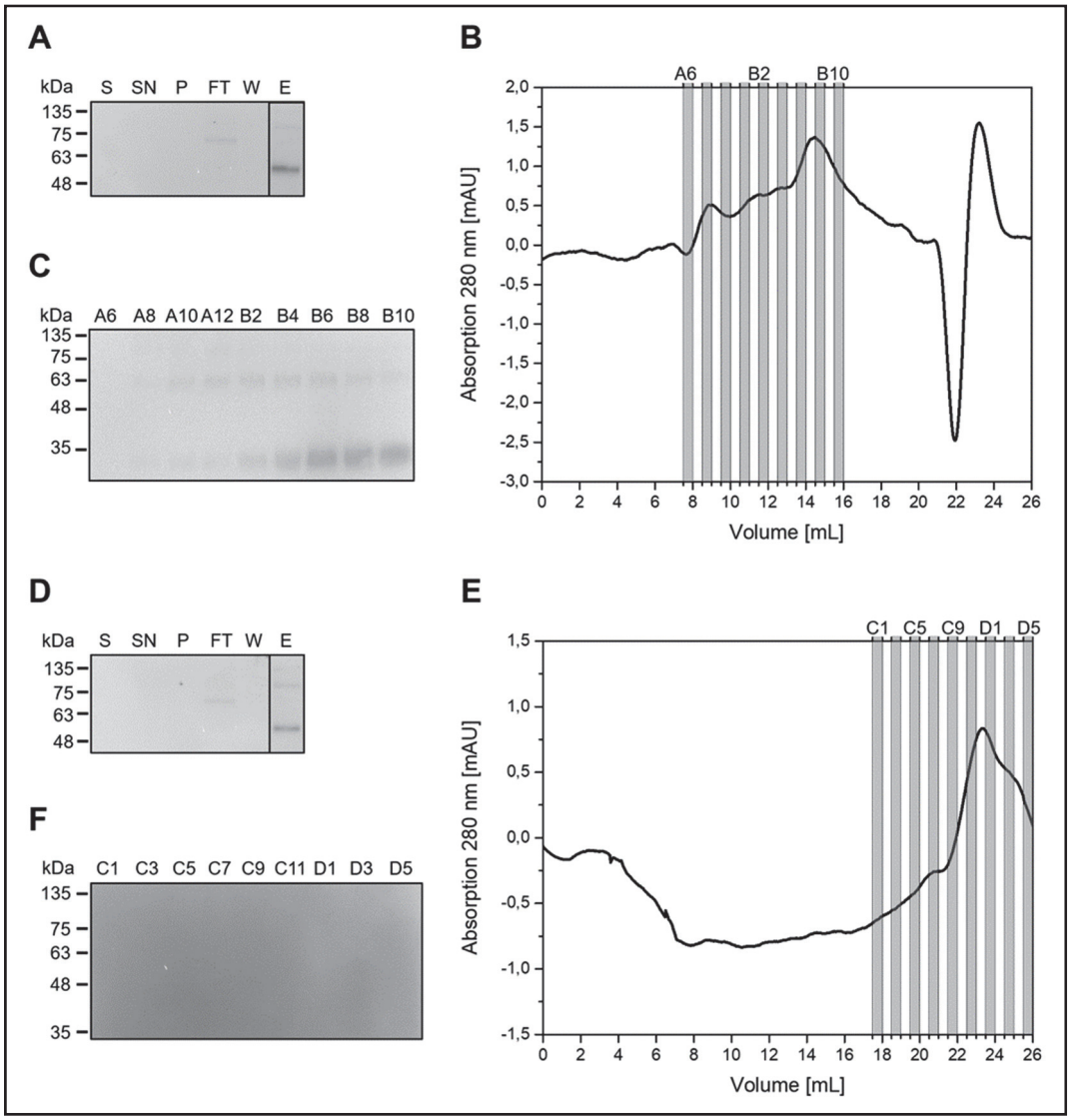

Figure 3.18: Antibody affinity purification and size exclusion chromatography of C-Rho-hSERT-Sf9 with FC12 and DDM. **(A)** Western blot with α-Rho immunodetection of Rho-hSERT with 0.1 % FC12 for antibody affinity purification. **(B)** Elution profile of Rho-hSERT-Sf9 with 0.1 % FC12 using Superdex 200 10/300 GL column. **(C)** Western blot with α-Rho immunodetection of Rho-hSERT-Sf9 with 0.1 % FC12 for SEC fractions A6-B10. **(D)** Western blot with α-Rho immunodetection of Rho-hSERT with 0.02 % DDM for antibody affinity purification. **(E)** Elution profile of Rho-hSERT-Sf9 with 0.02 % DDM using Superdex 200 16/60 PG column. **(F)** Western blot with α-Rho immunodetection of Rho-hSERT-Sf9 with 0.02 % DDM for SEC fractions C1-D5. S: membrane suspension; SN: supernatant; P: pellet; FT: flow through; W: wash; E: elution

Panel A in Figure 3.18 shows the samples from solubilization and purification of Rho-hSERT-Sf9 with FC12 after α-Rho immunodetection. Within the first three fractions, i.e. during and immediately after solubilization, no signal for Rho-hSERT was detected. A faint band with an apparent MW of ~71 kDa was found in the flow through after incubation with Rho1D4 agarose, while the washing fraction appears to be free of target protein. The elution fraction revealed a signal for Rho-hSERT with an apparent MW of ~56 kDa, which is 8 kDa lower compared to the test expression of Rho-hSERT-Sf9 (3.2.2.1). Additionally, a second band with

an apparent MW of ~78 kDa was also found in the elution fraction. Protein yield in the elution fractions was estimated as 40 µg g^{-1} cell pellet. The elution fractions were pooled, concentrated and loaded onto a Superdex 200 10/300 GL column. The SEC elution profile is shown in panel B of Figure 3.18. The elution profile displayed a poor signal-to-noise ratio, the maximum peak is around 1.5 mAU at 14.4 mL, which corresponds to a MW of ~127 kDa. Western blot immunodetection for corresponding SEC fractions (Figure 3.18 C) revealed two distinct bands with an apparent MW of ~ 63 kDa and ~ 33 kDa. The ~ 63 kDa band is in between the MW of those two bands detected in flow through and elution fraction during antibody affinity purification (Figure 3.18 A). Instead, it corresponds to the MW of the band detected during test expression (3.2.2.1). The ~ 33 kDa band is a putative degradation product of Rho-hSERT-Sf9, which could not be separated from the first band through SEC. The intensity of this band increases towards higher elution volumes.

Samples from solubilization and purification of Rho-hSERT-Sf9 with DDM after α-Rho immunodetection are shown in panel D of Figure 3.18. The band pattern was essentially the same as that for FC12 purified hSERT: a faint band with an apparent MW of ~71 kDa in the flow through and two bands with an apparent MW of ~56 kDa and ~78 kDa in the elution fraction. Protein yield in the elution fractions was estimated as 20 µg g^{-1} cell pellet The SEC elution profile of DDM purified Rho-hSERT-Sf9 (Figure 3.18 E) showed a negative absorption with a single peak around 23.5 mL, that exceeded the column's total volume (V_{total} = 22.9 mL) and corresponds to a MW of <3 kDa. No target protein was immunodetected for SEC fractions C1-D5.

3.4.2 Purification of C-His_8-hSERT-Sf9 with FC12

Expression of pTriEx-hSERT in Sf9 cells and membrane preparation was carried by Barbara Maertens and Jan Kubicek at Cube Biotech (Monheim). C-terminal His_8-tagged hSERT-Sf9 was purified through antibody affinity chromatography (2.2.2.2.3) and SEC (2.2.2.2.5). Samples were taken from different stages during the purification process and analyzed through antibody immunodetection after SDS-PAGE (2.2.2.4.2) and subsequent Western blot transfer (2.2.2.4.3) as shown in Figure 3.19.

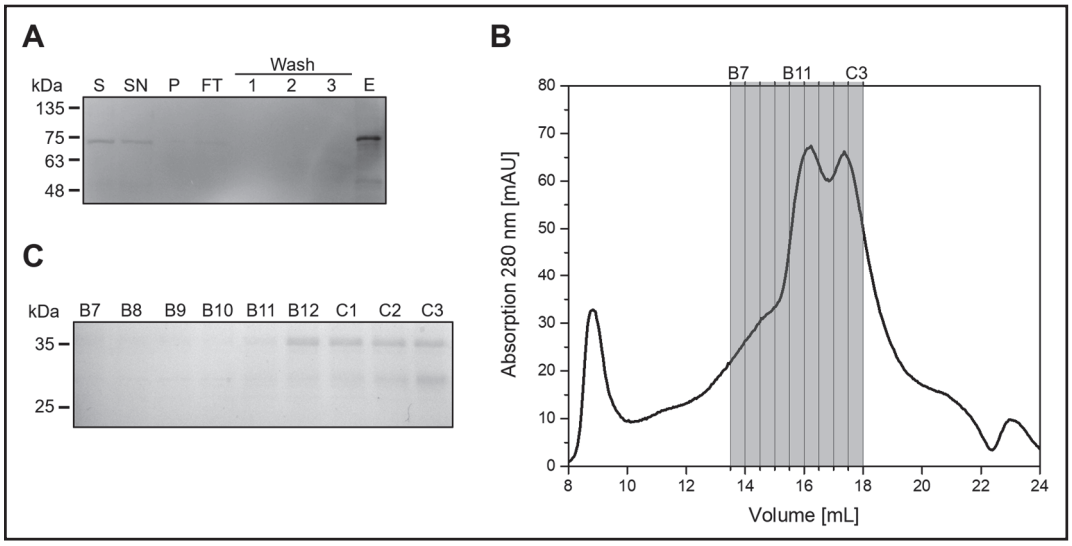

Figure 3.19: Metal affinity and size exclusion chromatography of C-His_8-hSERT-Sf9 with FC12. **(A)** Western blot with α-His immunodetection of His-hSERT-Sf9 with 0.1 % FC12 for metal affinity purification. **(B)** Elution profile of Rho-hSERT-Sf9 with 0.1 % FC12 using Superdex 200 10/300 GL column. **(C)** Coomassie blue-silver stained SDS-PAGE of His-hSERT-Sf9 with 0.1 % FC12 for SEC fractions B7-C3. S: membrane suspension; SN: supernatant; P: pellet; FT: flow through; E: elution

Samples from solubilization and IMAC purification of C-His_8-hSERT-Sf9 in FC12 after α-His immunodetection are shown in panel A of Figure 3.18. Signal for His-tagged hSERT was found in the membrane suspension and in the supernatant after sedimentation with an apparent MW of ~73 kDa. This band is also found in the IMAC elution fraction, along with smaller bands, indicating a degradation of His-hSERT-Sf9. Furthermore, the MW is in agreement with the MW observed during test expression of His-hSERT-Sf9 (3.2.2.2). The pellet and flow through fractions contain a faint band, while the washing fractions appeared to be free of target protein. The SEC elution profile (Figure 3.19 B) from Superdex 200 GL showed two peaks with an absorption of ~65 mAU at 16.2 mL and 17.3 mL. These elution volumes correspond to an apparent MW of ~ 57 kDa and ~ 35 kDa, respectively. The Coomassie blue-silver stained SDS-PAGE of SEC fractions B7-C3 (Figure 3.19 C) revealed two protein bands with an apparent MW of ~36 kDa and ~28 kDa. A band corresponding to the MW of full-length hSERT was not found.

3.5 Reconstitution of purified hSERT

3.5.1 Reconstitution of N-His_8-hSERT into liposomes

Purified N-His_8-hSERT was used for reconstitution in liposomes (2.2.2.3.1) to stabilize it in a detergent free environment. The last step in the reconstitution process is an ultracentrifugation step to separate the liposomes from the aqueous environment. Samples were taken from the supernatant and the liposome fraction as well as from the starting sample and analyzed

through Coomassie blue-silver stained SDS-PAGE (2.2.2.4.2) and subsequent Western blot transfer with immunodetection (2.2.2.4.3). Results are shown in Figure 3.20.

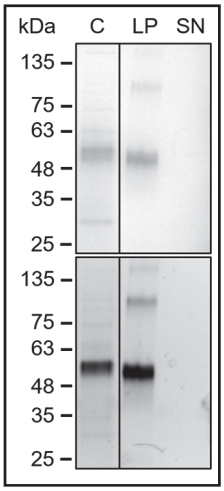

Figure 3.20: SDS-PAGE and Western blot analysis of liposome reconstituted N-His_8-hSERT. Top panel: Coomassie blue-silver stained SDS-PAGE. Bottom panel: Western blot with α-His antibody immunodetection. C: control sample; LP: liposome fraction; SN: supernatant

N-His_8-hSERT was found with an apparent MW of ~58 kDa in the liposome fraction (LP), which was collected after ultracentrifugation, while the supernatant (SN) appeared to be free of protein. This shows that the reconstitution of hSERT into liposomes was successful. Furthermore, the control sample (C) contains protein bands around 100, 75, 63 and 30 kDa, which were not found in liposome fraction. Additionally, the liposome fraction contains His-positive protein bands around ~120 and above ~135 kDa. These are probably stable oligomers of N-His_8-hSERT that cannot be separated through SDS-PAGE.

3.6 Biophysical characterization of N-His_8-hSERT

3.6.1 Secondary structure analysis of N-His_8-hSERT

3.6.1.1 Analysis of influence of various lipids on N-His_8-hSERT secondary structure by circular dichroism spectroscopy

The secondary structure of hSERT derived from *E. coli* membrane was characterized by circular dichroism spectroscopy. Target protein was purified with 0.1 % (w/v) FC12 detergent along with human neuronal lipids extract (NL; 1:10 molar ratio of protein and lipids) and/or 0.01 % (w/v) cholesteryl hemisuccinate (CHS) or a mixture of 0.01 % (w/v) CHS and 25 µM phospholipids (POPx; 1:1:1 molar ratio of POPC, POPG and POPE). As a control, hSERT purified with 0.1 % (w/v) FC12 or 0.02 % (w/v) DDM and without additional lipids was analyzed as well. Individual spectra recorded at 4 °C and normalized to the mean residue ellipticity

(MRE) are shown in Figure 3.21 A. The overall shapes of the spectra resemble the typical α-helical spectrum with minima at 208 and 222 nm.

The obtained CD spectra were deconvoluted using DichroWeb online server [181]. The determined secondary structure content was compared to the secondary structure content predicted with 'PredictProtein' [184] as well as the secondary structure known from x-ray crystal structure of paroxetine bound hSERT (PDB-ID: 5I6X). Missing secondary structure information about the N-terminal and C-terminal domain from the crystal structure was added based on the results from [125]. Obtained results are shown in Figure 3.21 B.

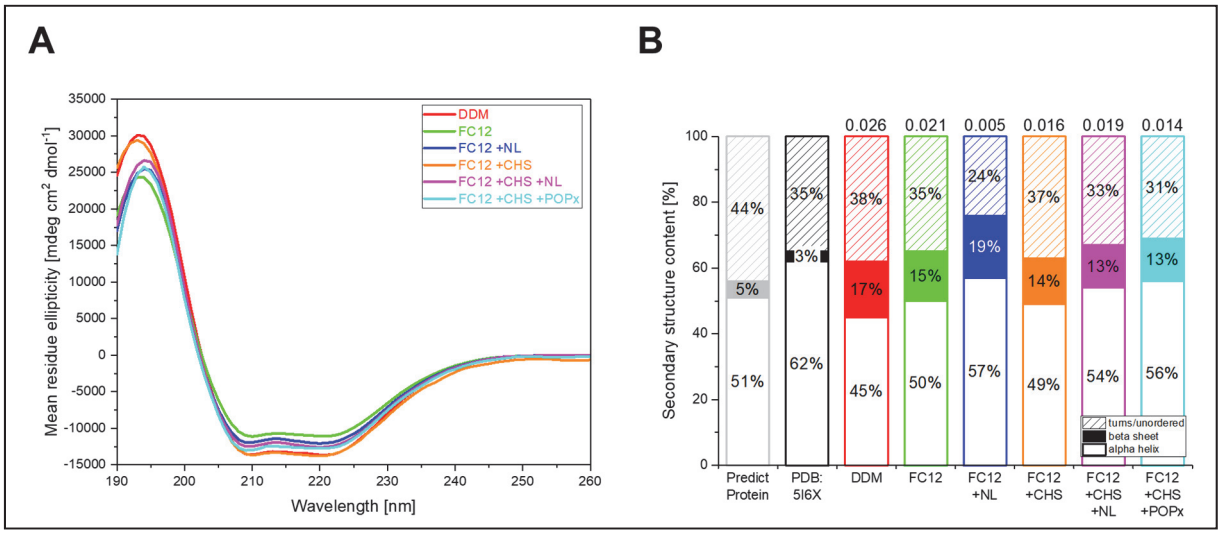

Figure 3.21: Secondary structure analysis of N-His$_8$-hSERT with different lipids. **(A)**: CD spectra of N-His-hSERT recorded at 4 °C. **(B)**: Relative amount of secondary structure elements (blank: alpha helix; solid: beta sheet; striped: turns/unordered). The normalized root-mean-square deviation for deconvoluted data is noted on top of each bar. Secondary structure prediction of hSERT (grey); secondary structure content of published crystal structure 5I6X; hSERT purified in DDM (red); FC12 (green); FC12 +NL (blue); FC12 +CHS (orange); FC12 +CHS +NL (magenta); FC12 +CHS +POPx (cyan).

The crystal structure revealed a content of 62 % α-helical structure, 3 % β-sheet and 35 % turns/unordered regions. Comparison with the predicted secondary structure content showed that the β-sheet content differs by 2 percentage points (pp) while the estimates for α-helix and turns/unordered region differ by almost 10 pp.

Among all analyzed samples, hSERT purified with DDM showed the lowest α-helical content (45 %) with 17 % β-sheets and 38 % content of turns/unordered regions. Using FC12 for purification increased the α-helical content to 50 % while the content of β-sheet and turns/unordered regions decreased to 15 % and 35 %, respectively. Addition of NL to FC12 purified hSERT increased the α-helical content to 57 % while at the same time the β-sheet content increased to 19 %. The increase of these structural elements is compensated by a decrease of turns/unordered region to as low as 24 %. In contrast to that, the addition of CHS

alone has only a small impact on the structural content as it alters the content of each element by 1-2 pp only. The combination of NL and CHS together increased the α-helical content to 54 % while the β-sheet content remained at 13 %, the lowest determined value for this structural element. The inclusion of CHS and POPx for FC12 purified hSERT led to a further increase of α-helical structure to 56 % and a decrease of turns/unordered regions content to 31 %. None of the analyzed samples showed a low β-sheet content as expected from the structure content prediction and crystal structure. The determined values showed a 10-16 pp higher content for this structure, while the content of α-helical structure is 5-17 pp lower than expected. Except for one sample (FC12 +NL; 24 %), the values for turns and unordered regions are relatively close to the expected value of 35 % (± 3 pp). The combination of cholesterol and NL or POPx showed the highest α-helical content, and, at the same time, the lowest β-sheet content among the analyzed samples.

3.6.1.2 Analysis of influence of inhibitors on N-His$_8$-hSERT secondary structure by circular dichroism spectroscopy

The influence of functional inhibitors citalopram, desipramine and fluoxetine at a molar ratio of 1:10 (protein:inhibitor) on the secondary structure content of hSERT was analyzed using CD spectroscopy. All samples were purified in 0.1 % (w/v) FC12 supplemented with 0.01 % (w/v) CHS and 25 µM POPx. Samples were incubated with inhibitor for 30 min on ice. The CD spectra of individual samples at 4 °C is shown in Figure 3.22 A.

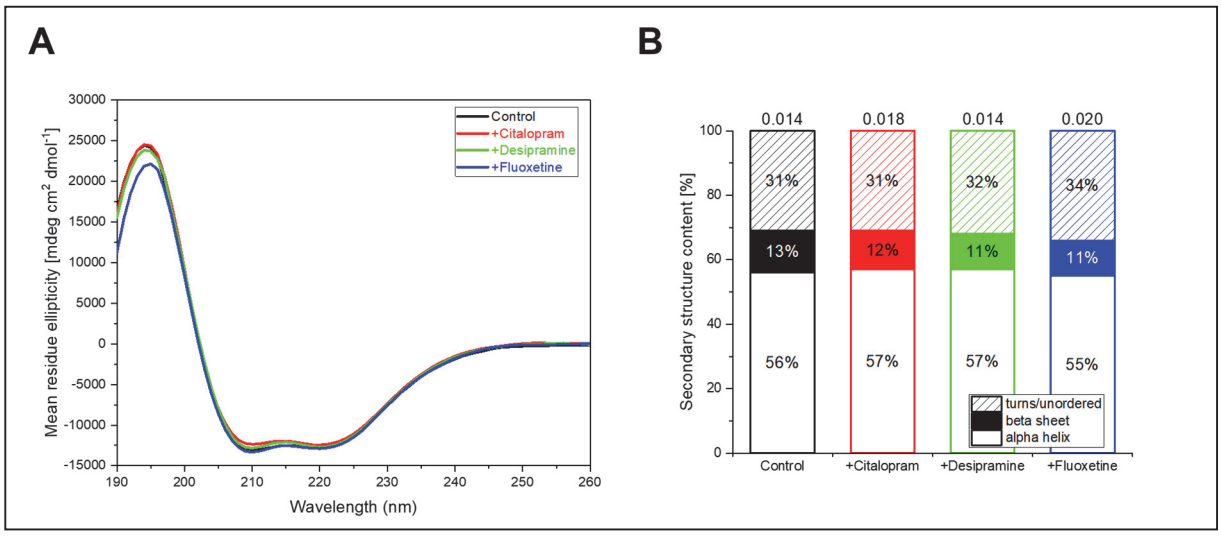

Figure 3.22: Secondary structure analysis of N-His$_8$-hSERT with functional inhibitors. **(A)**: CD spectra of N-His-hSERT recorded at 4 °C. **(B)**: Relative amount of secondary structure elements (blank: alpha helix; solid: beta sheet; striped: turns/unordered). The NRMSD of the best solution is noted on top of each bar. Human SERT without inhibitor (control; black); with citalopram (red); with desipramine (green); with fluoxetine (blue).

The overall influence of functional inhibitors appeared to be small, as they alter the content of structural elements by 1-3 pp compared to the control. For citalopram and desipramine, a decrease in β-sheet content by 1-2 pp can be observed, while the α-helical content increased by 1 pp. A decreasing effect on the β-sheet and α-helical content was seen for fluoxetine. Compared to the control sample, the content for turns/unordered regions increased by 1-3 pp.

3.6.2 Thermostability of N-His_8-hSERT

3.6.2.1 Differential scanning fluorimetry of N-His_8-hSERT

Thermostability of N-His_8-hSERT purified with either 0.1 % (w/v) FC12 or 0.02 % (w/v) DDM was analyzed by differential scanning fluorimetry (DSF) using the fluorescent dyes CPM or ANS. Protein samples were incubated individually with the respective dye for 10 min and the fluorescence signal was recorded while heating the samples from 5 to 95 °C. Figures 3.23 A and B show the relative fluorescence intensity of CPM-labeled and ANS-labeled hSERT, respectively, in FC12 and DDM as a function of temperature. The corresponding melting temperatures (Tm) were derived from the maxima and minima of the first derivative; that is the temperature where the strongest change of fluorescence intensity appears (Figures 3.23 C and D). Two melting temperatures could be determined for every sample. The first Tm for CPM-labeled hSERT in FC12 or DDM was determined as 26 °C and 27 °C, respectively (Figure 3.23 C). The first Tm for ANS-labeled hSERT (Figure 3.23 D) is lower compared to CPM-labeled hSERT and was determined as 23 °C for both samples. The second Tm was determined for CPM-labeled hSERT in FC12 or DDM with 43 °C and 54 °C, respectively, and for ANS-labeled hSERT in FC12 or DDM with 67 °C and 71 °C, respectively. The results obtained from DSF and CD spectroscopy (3.6.2.2) are summarized in Table 3.1

Table 3.1: Melting temperatures of N-His8-hSERT

	CPM	ANS	CD_{222}
FC12	26 °C / 43 °C	23 °C / 71 °C	46 °C
DDM	27 °C / 54 °C	23 °C / 67 °C	57 °C

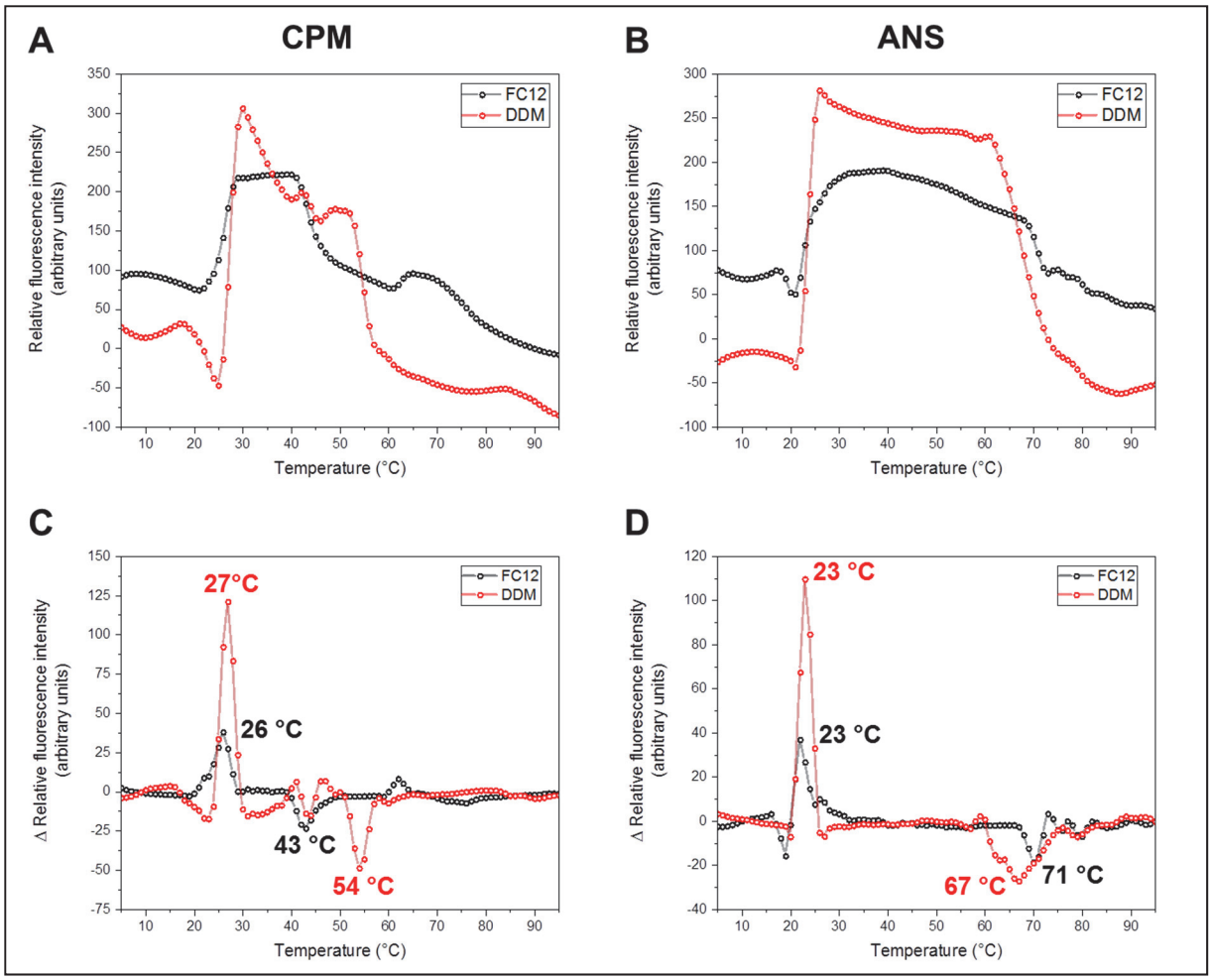

Figure 3.23: Differential scanning fluorimetry of N-His$_8$-hSERT in presence of FC12 or DDM. Human SERT was purified with either FC12 (black) or DDM (red). Protein samples were labeled using either CPM (left panel) or ANS (right panel) as fluorescent dye. **(A)**: Fluorescence intensity of hSERT-CPM as a function of temperature. **(B)** Change of fluorescence intensity of hSERT-CPM as a function of temperature. **(C)** Fluorescence intensity of hSERT-ANS as a function of temperature. **(D)** Change of fluorescence intensity of hSERT-ANS as a function of temperature. Corresponding melting temperatures (Tm) are indicated.

3.6.2.2 Analysis of influence of lipids on N-His$_8$-hSERT thermal stability by circular dichroism spectroscopy

The influence of various lipid mixtures on the thermostability of hSERT was investigated by CD spectroscopy. Target protein was purified with FC12 detergent along with NL (1:10 molar ratio protein:lipid) and/or 0.01 % (w/v) CHS or a mixture of 0.01 % (w/v) CHS and 25 µM POPx. As a control, hSERT purified in 0.1 % (w/v) FC12 or 0.02 % (w/v) DDM without additional lipids was analyzed as well. Samples were heated from 5 to 95 °C and the CD signal at 222 nm was recorded. The fraction of unfolded protein was calculated from the data and plotted as a function of temperature (Figure 3.24 A). A two-state transition model was used for nonlinear

regression analysis and a comparison of the obtained melting temperatures is shown in Figure 3.24 B.

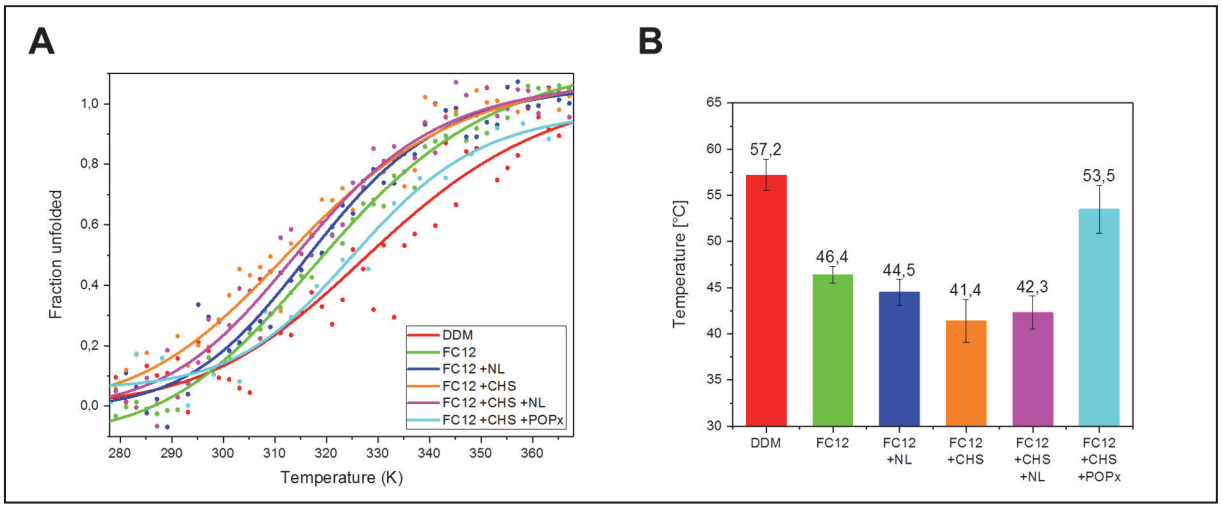

Figure 3.24: Circular dichroism thermal shift assay of N-His$_8$-hSERT with different lipids. **(A)** Fraction of unfolded hSERT at 222 nm as a function of temperature. Data were fitted using a two-state transition model. **(B)** Comparison of melting temperatures. N-His$_8$-hSERT purified in DDM (red); FC12 (green); FC12 +NL (blue); FC12 +CHS (orange); FC12 +CHS +NL (magenta); FC12 +CHS +POPx (cyan).

The highest Tm was found for hSERT purified with DDM and was determined as 57.2 °C, while the Tm obtained for hSERT with FC12 was more than ten degrees lower (46.4 °C). Addition of NL or CHS or a combination of both compounds led to a further decrease of the Tm down to 41.4 °C. Compared to the protein with FC12 only, the addition of CHS and POPx increased the Tm by ~ 7 °C to 53.5 °C.

3.6.2.3 Analysis of influence of inhibitors on N-His$_8$-hSERT thermal stability by circular dichroism spectroscopy

The influence of functional inhibitors citalopram, desipramine and fluoxetine at a 1:10 molar ratio (protein:inhibitor) on the thermostability of 0.1 % (w/v) FC12 purified hSERT supplemented with 0.01 % (w/v) CHS and 25 µM POPx was analyzed by CD spectroscopy. Samples were incubated with inhibitors for 30 min on ice before starting the measurement. Samples were heated from 5 to 95 °C and the CD signal at 222 nm was recorded. The fraction of unfolded protein was calculated from the CD data and plotted as a function of temperature (Figure 3.25 A). A comparison of the obtained melting temperatures is shown in Figure 3.25 B.

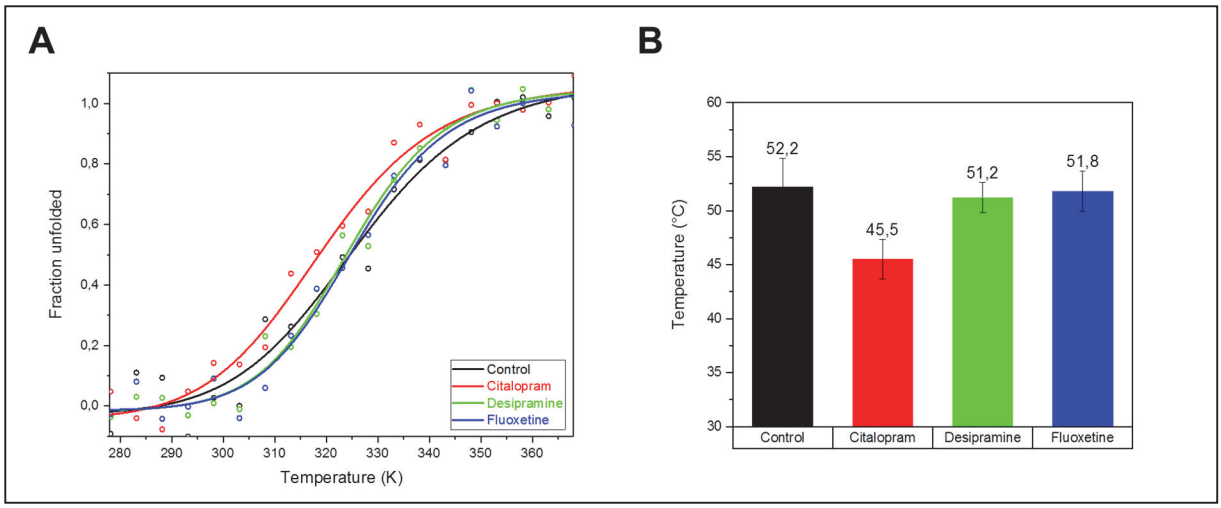

Figure 3.25: Circular dichroism thermal shift assay of N-His$_8$-hSERT in presence of different inhibitors. **(A)** Fraction of unfolded hSERT at 222 nm as a function of temperature. Data were fitted to a two-state transition model. **(B)** Comparison of melting temperatures obtained at 222 nm. N-His8-hSERT without inhibitor (control; black); with citalopram (red); with desipramine (green); with fluoxetine (blue).

The melting curve of hSERT observed at 222 nm is exhibiting a two-state transition denaturation (Figure 3.25 A). Therefore, melting temperatures were obtained by nonlinear regression analysis based on a two-state transition model. Compared to the control sample without inhibitor, all assayed inhibitors decreased the thermostability of hSERT (Figure 3.25 B). While the observed decrease for desipramine and fluoxetine is within a range from ~ 0.5 to 1 °C, the extent of citalopram's destabilizing effect is larger (~ 7 °C).

3.6.2.4 Analysis of influence of inhibitors on N-His$_8$-hSERT thermal stability by intrinsic tryptophan fluorescence

The influence of functional inhibitors citalopram, desipramine and fluoxetine at a 1:10 molar ratio (protein:inhibitor) on the thermostability of 0.1 % (w/v) FC12 purified hSERT supplemented with 0.01 % (w/v) CHS and 25 µM POPx was analyzed using intrinsic tryptophan fluorescence. The same samples as in section 3.5.2.3 were used for this analysis. Samples were incubated with inhibitors for 30 min on ice before starting the measurement. Samples were heated from 5 to 95 °C and emission spectra between 400 and 275 nm after excitation at 295 nm was recorded. The fraction of unfolded protein was calculated from the fluorescence data at 335 nm and plotted as a function of temperature (Figure 3.26 A). A comparison of the obtained melting temperatures is shown in Figure 3.26 B.

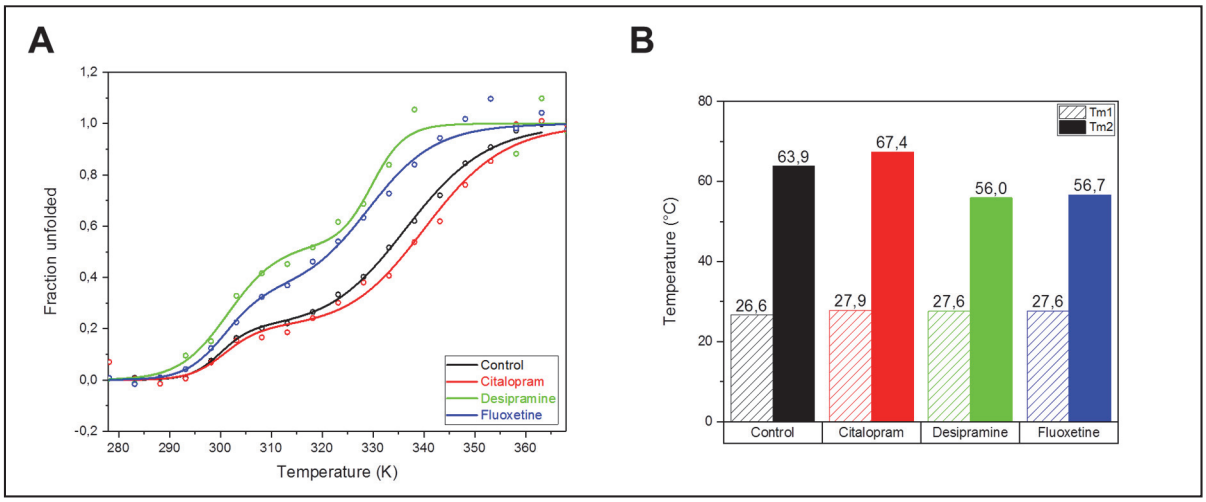

Figure 3.26: Tryptophan fluorescence thermal shift assay of N-His$_8$-hSERT in presence of different inhibitors. **(A)** Fraction of unfolded hSERT at 335 nm as a function of temperature. Data were fitted to a three-state transition model. **(B)** Comparison of melting temperatures Tm1 (striped) and Tm2 (solid) obtained at 335 nm. Human SERT without inhibitor (control; black); with citalopram (red); with desipramine (green); with fluoxetine (blue).

The melting curve of hSERT observed at 335 nm is showing a three-state transition (Figure 3.25 C). Therefore, melting temperatures were obtained by nonlinear regression analysis using a three-state transition model yielding two melting temperatures (Tm1 and Tm2). Among all samples, the value for Tm1 is within a range from 26.6 to 27.9 °C, with the control sample of hSERT having the lowest value (Figure 3.25 D). The Tm2 for the control sample was 63.9 °C and addition of citalopram increased this value by 3.5 °C to 67.4 °C. For desipramine and fluoxetine, an opposing effect was observed, reducing the value of Tm2 to 56.0 and 56.7 °C, respectively.

3.6.3 Binding affinity of N-His$_8$-hSERT for functional inhibitors

3.6.3.1 Analysis of binding affinity by microscale thermophoresis

NT-647 labeled hSERT purified with 0.1 % (w/v) FC12, 0.01 % (w/v) CHS and 25 µM POPx was incubated with citalopram, desipramine or fluoxetine over a concentration range of 20 pM-20 mM (Figure 3.27 A). The observed signal for all inhibitors remains at a stable baseline over a broad range of concentrations. The signal showed an increase around 0.1-1 mM without reaching a plateau, indicating nonspecific binding between hSERT and inhibitor. Furthermore, hSERT was reconstituted in POPx liposomes and incubated with 0.3 nM-1 mM fluoxetine (Figure 3.27 B). No specific interaction could be observed. Compared to FC12 purified hSERT, the variation of signal intensity appears to be greater for both, sample and control.

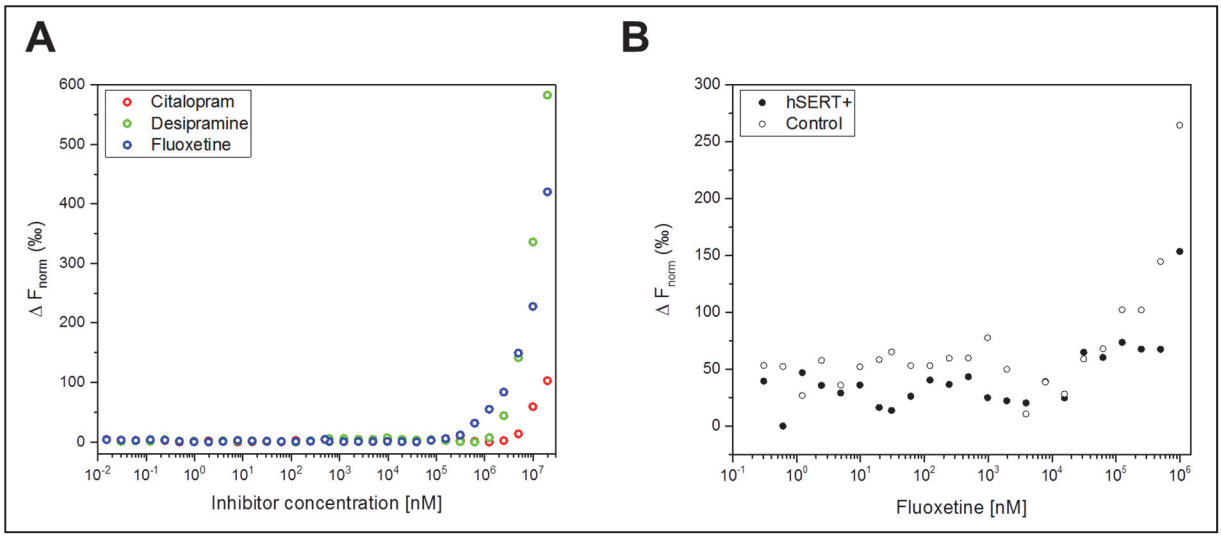

Figure 3.27: Saturation binding curve for N-His_8-hSERT and functional inhibitors. **(A)** NT-647 labeled hSERT with citalopram (red), desipramine (green) or fluoxetine (blue). **(B)** Liposome reconstituted hSERT (black) or empty liposomes (white) with fluoxetine. Normalized fluorescence difference signal was plotted as a function of inhibitor concentration.

3.6.3.2 Analysis of binding affinity by surface plasmon resonance

Binding affinity between hSERT from *E. coli* membrane and functional inhibitors citalopram, desipramine and fluoxetine was measured using surface plasmon resonance (SPR). Initial binding experiments were done with a Reichert SR7500DC instrument with the ligand (hSERT) captured on a NiHC1000 sensor chip. Citalopram and desipramine were assayed over a concentration range from 50 pM-5 µM. Data was adjusted after referencing to exclude injection spikes. For both experiments, association and dissociation of analyte to ligand could be observed. Data from citalopram binding showed a decrease of the maximum binding signal at equilibrium with increasing analyte concentration and was therefore excluded from equilibrium and kinetic analysis.

For initial analysis by equilibrium data, normalized RUs from desipramine binding to hSERT at the equilibrium phase were plotted as a function of analyte concentration (Figure 3.28 A). Estimation of the equilibrium dissociation constant k_D from this plot was not possible as the lowest concentration shows a fractional occupation of 0.65 and the inflection could not be determined. Furthermore, data was plotted as Scatchard plot (Figure 3.28 B) and Hill plot (Figure 3.28 C). The concave up curve of the Scatchard plot indicates non-specific binding, negative cooperativity or multiple classes of binding sites while the linear regression analysis of the Hill plot revealed a slope of 0.084 which indicates negative cooperativity binding.

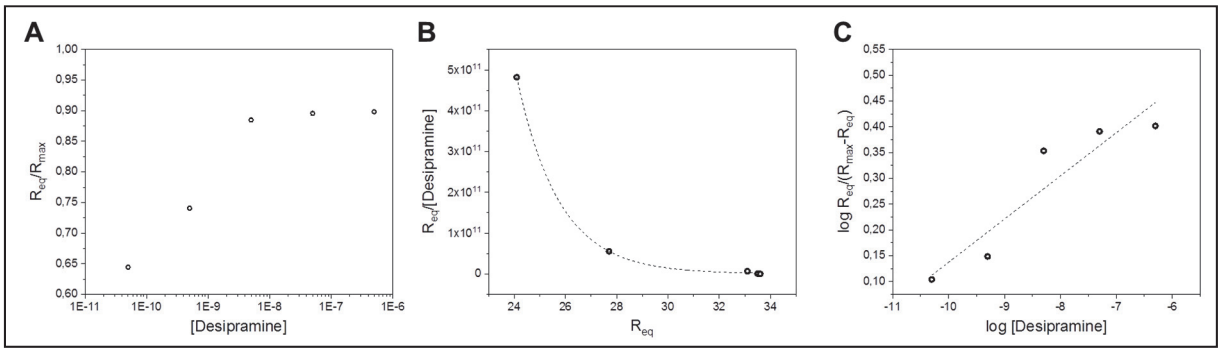

Figure 3.28: Analysis of equilibrium binding data. **(A)** Normalized response units at equilibrium as a function of desipramine concentration (Klotz plot). The inflection point (k_D) could not be determined. **(B)** Scatchard plot of equilibrium binding data. The concave-up curve may indicate non-specific binding, negative cooperativity or multiple classes of binding sites. **(C)** Hill plot of equilibrium binding data. The slope of the Hill plot (0.084) indicates negative cooperativity.

Non-linear regression analysis of SPR sensorgrams was done using different binding models and the results are shown in Figure 3.29 A-E and Table 3.2. Global fitting of a 1:1 binding model to the data from five different analyte concentrations revealed a global dissociation rate constant k_d of 0.03 s^{-1} (± 4.7 × 10^{-5}) and a global association rate constant k_a of 10848 M^{-1} s^{-1} (± 220). The kinetic dissociation constant k_D was determined as 2.8 µM (± 0.05).

Since hSERT has two binding sites, a model of a heterogeneous ligand was used to fit the data (Figure 3.29 B). This model describes the binding of an analyte molecule to two independent binding sites as the sum of two exponential equations. Global fitting of the dissociation phase reveals two different rate constants: a fast k_{d1} (0.026 s^{-1}), which is similar to the k_d obtained with the 1:1 binding model, and a slow k_{d2} (0.008 s^{-1}). In contrast to the previous model, a global fit of a 1:1 association model was not possible. Local fitting of association rate constant k_a with a globally constrained k_{d1} and k_{d2} reveals values for k_{a1} and k_{a2} that are directly dependent on the analyte concentration: increasing the analyte concentration by one order of magnitude decreases the apparent k_a by the same order of magnitude.

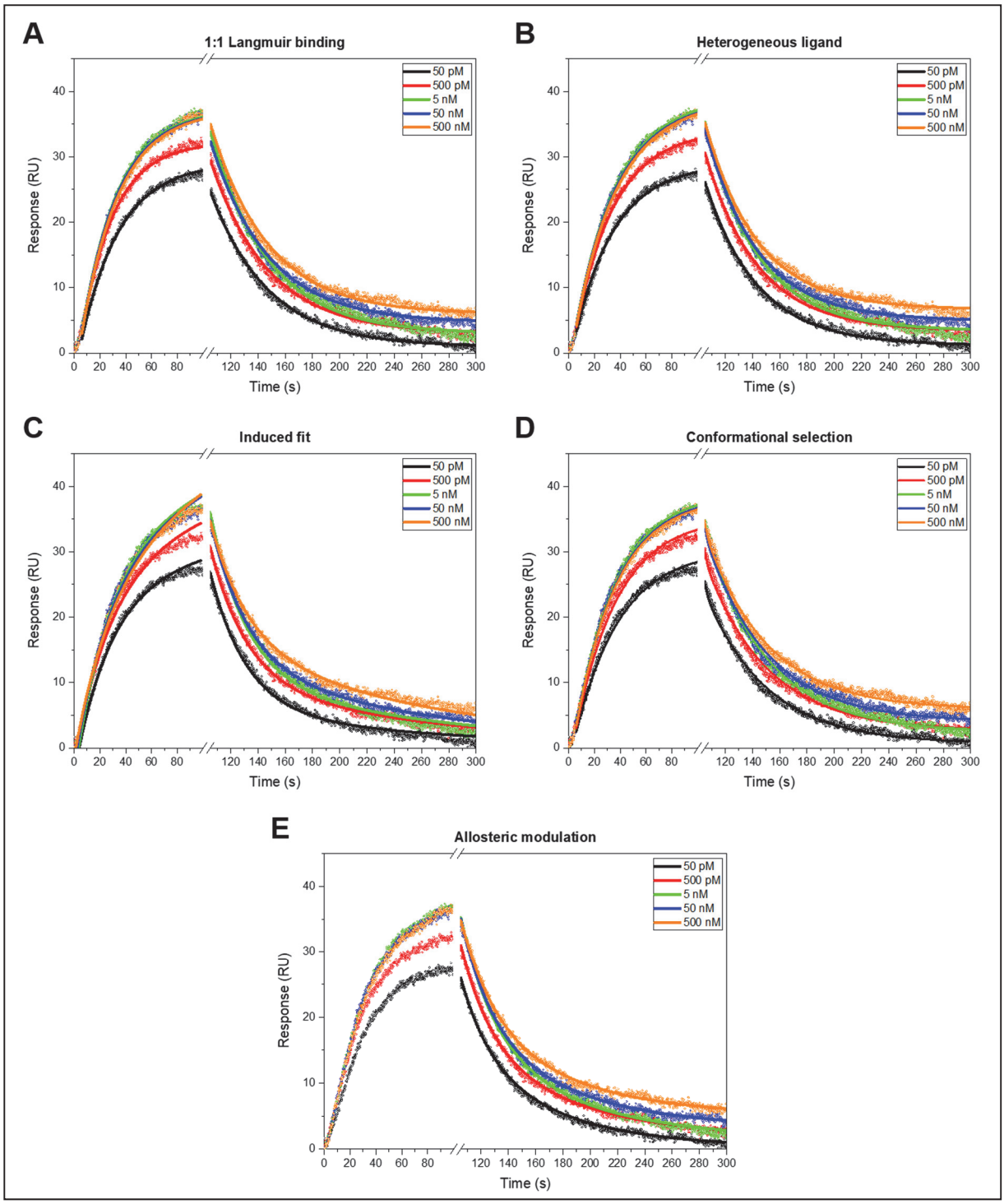

Figure 3.29: Sensorgrams of desipramine binding to N-His_8-hSERT captured on NiHC1000 chip. **(A)** 1:1 Langmuir binding model. **(B)** Heterogeneous ligand model. **(C)** Induced fit model. **(D)** Conformational selection model. **(E)** Allosteric modulation model. Dots: experimental observation. Line: best fit solution. Desipramine concentrations: 50 pM (black); 500 pM (red); 5 nM (green); 50 nM (blue); 500 nm (orange).

Table 3.2: Apparent rate constants of hSERT:desipramine interaction determined from different models.

	k_{a1} [$M^{-1}s^{-1}$]	k_{d1} [s^{-1}]	-	-	[Desipramine]	Chi²	R²
1:1 Langmuir	1.1E+04	0.0305			5.0E-11 5.0E-10 5.0E-09 5.0E-08 5.0E-07	k_a: 0.34 k_d: 0.55	Ka: 0.996 Kd: 0.989

	k_{a1} [$M^{-1}s^{-1}$]	k_{d1} [s^{-1}]	k_{a2} [$M^{-1}s^{-1}$]	k_{d2} [s^{-1}]	[Desipramine]	Chi²	R²
Heterogeneous ligand	2.5E+08 2.3E+07 2.8E+06 2.5E+05 2.8E+04	0.0267	4.4E+08 4.7E+07 3.7E+06 3.9E+05 3.6E+04	0.0084	5.0E-11 5.0E-10 5.0E-09 5.0E-08 5.0E-07	0.29	0.9951

	k_{a1} [$M^{-1}s^{-1}$]	k_{d1} [s^{-1}]	k_{a2} [$M^{-1}s^{-1}$]	k_{d2} [s^{-1}]	[Desipramine]	Chi²	R²
Induced fit	4.2E+04 4.5E+03 5.3E+02 5.0E+01 4.7E+00	0.0349	2.1E-03 3.7E-03 3.3E-03 4.3E-03 5.9E-03	0.0078	5.0E-11 5.0E-10 5.0E-09 5.0E-08 5.0E-07	0.42	na

	k_{a1} [$M^{-1}s^{-1}$]	k_{d1} [s^{-1}]	k_{a2} [$M^{-1}s^{-1}$]	k_{d2} [s^{-1}]	[Desipramine]	Chi²	R²
Conformational selection	1.4E+08 1.7E+07 1.9E+06 1.9E+05 1.9E+04	0.0222	9.8E+00	0.5800	5.0E-11 5.0E-10 5.0E-09 5.0E-08 5.0E-07	0.36	0.9942

	k_{d1} [s^{-1}]	k_{d2} [s^{-1}]	k_{d3} [s^{-1}]	-	[Desipramine]	Chi²	R²
Allosteric modulation	0.1021	0.0132	0.0304		5.0E-11 5.0E-10 5.0E-09 5.0E-08 5.0E-07	0.20	0.9962

Next, two different biphasic models were used that account for a conformational change of the protein. In the first model, the conformational change appears after binding of analyte to the ligand (induced fit; Figure 3.29 C), whereas the second model assumes an equilibrium between two different conformational states of the ligand, and only one of the two states is able to bind to an analyte molecule (conformational selection; Figure 3.29 D) [204]. Both models employ two sets of rate constants, where the first set (k_{a1}, k_{d1}) describes association and dissociation of analyte to ligand and the second set (k_{a2}, k_{d2}) describes the conformational

change. The k_d values obtained from the heterogeneous ligand model were used as starting values for the fitting procedure. For both models, a global fit for the first association rate constant is not possible. Instead, a local fit for k_{a1} was calculated, which revealed a direct dependency for on the analyte concentration as observed before. In the induced fit model, the values for k_{a2} are within the same order of magnitude but show an increasing trend with increasing analyte concentration. Furthermore, these values are close to the corresponding dissociation constant of 0.008 s^{-1}. In contrast to that, the k_{a2} in the conformational selection model was globally fitted with 9.8 M^{-1} s^{-1} and the corresponding dissociation rate constant is almost 20-fold smaller (0.58 s^{-1}). To further discriminate between heterogenous ligand, induced fit and conformational selection, two observed rate constants $\sigma 1$ and $\sigma 2$ were determined using a bi-exponential equation and their dependency on the analyte concentration $[c]$ was analyzed [220] (Figure 3.30). The individual values of $\sigma 1$ and $\sigma 2$ as well as their sums and products were found to be non-linear in $[c]$. The inverse hyperbolic curve suggests the conformational selection model as the underlying mechanism [204], although it was not possible to fit this model to the data.

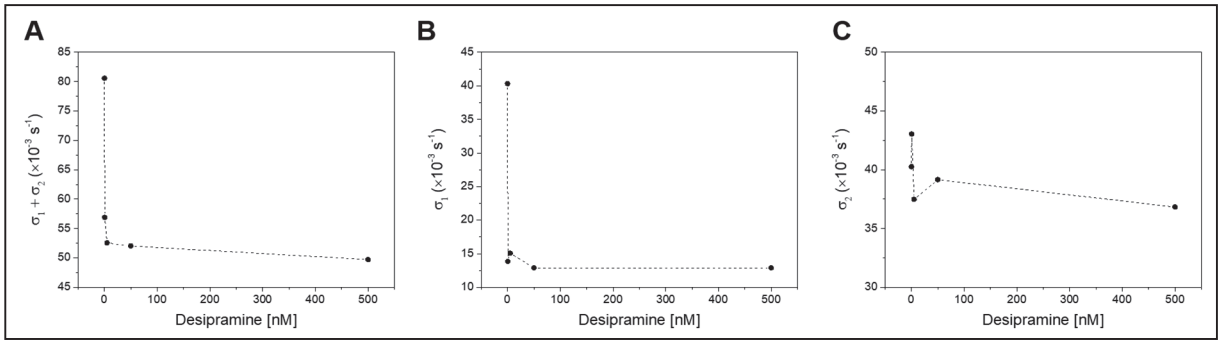

Figure 3.30: Dependency of σ_1 and σ_2 on the analyte concentration**. (A)** Sum of σ_1 and σ_2 as a function of desipramine concentration. **(B)** σ_1 as a function of desipramine concentration. **(C)** σ_2 as a function of desipramine concentration.

Furthermore, a model was developed that accounts for allosteric modulation during association and dissociation phase (Figure 3.29 E). This model uses three different dissociation and association rate constants to describe binding and unbinding of analyte to two different binding sites (k_1, k_2), where dissociation from the central binding site is modulated (k_3) in presence of analyte molecule bound to the allosteric site. A fitting equation for each phase was derived from the model. Fitting the model to the dissociation phase obtained the following rate constants: k_{d1}: 0.102 s^{-1}; k_{d2}: 0.013 s^{-1}; k_{d3}: 0.031 s^{-1}. Due to the length of the association phase equation and software restrictions, it was not possible to run this equation in Origin or GraphPad. Therefore, no association rate constants could be determined with this model.

Finally, the number of exponential functions required for a model to describe the experimental observation was analyzed by fitting a series of simple mono- or multiphasic exponential functions to the data (Table 3.3). Considering the quality of the fit, both the bi- and triphasic dissociation model have similar Chi² values, with the triphasic model being the best-fit model. Both models have two distinct rate constants with similar values, though the triphasic model fits two rate constants that are virtually identical and show a relatively high SD of > 30 %. For the association phase, the tetraphasic model shows the lowest Chi² value. Although three out of four rate constants have similar values, their SD remains low (~ 0.3 %).

Table 3.3: Fitting of rate constants with a series of simple mono- or multiphasic exponential functions

Dissociation

	1 Exp			
	obs	SD	Chi²	R²
k1	41.4	± 0.05	0.3024	0.9942
	2 Exp			
	obs	SD	Chi²	R²
k1	45.6	± 0.07	0.2554	0.9951
k2	16.1	± 0.17		
	3 Exp			
	obs	SD	Chi²	R²
k1	45.7	± 17.7	0.2480	0.9952
k2	45.8	± 17.9		
k3	15.6	± 0.2		
	4 Exp			
	obs	SD	Chi²	R²
k1	51.1	± 1.2	0.3238	0.9938
k2	42.9	± 1.4		
k3	16.7	± 0.23		
k4	44.9	± 1.5		

Association

	1 Exp			
	obs	SD	Chi²	R²
k1	30.0	± 0.03	0.2341	0.9969
	2 Exp			
	obs	SD	Chi²	R²
k1	30.0	± 0.05	0.2341	0.9969
k2	30.0	± 0.05		
	3 Exp			
	obs	SD	Chi²	R²
k1	30.0	± 0.08	0.2343	0.9969
k2	30.0	± 0.08		
k3	30.0	± 0.08		
	4 Exp			
	obs	SD	Chi²	R²
k1	29.1	± 0.09	0.1677	0.9978
k2	26.1	± 0.08		
k3	28.9	± 0.09		
k4	38.8	± 0.09		

Further experiments were carried out using a Biacore T200 and NTA sensor chip with different protein preparations (± IEC; ± CHS and POPx), different detergents (FC12, FC14, DDM) and different SPR running buffers (TRIS, NaH_2PO_4, PBS). Only non-specific binding at micromolar concentrations could be observed during this experiments.

3.7 Crystallization of hSERT

Crystallization conditions for N-His-hSERT were screened using commercially available screening kits. Purified protein with 0.1 % (w/v) FC12 was supplemented with either neuronal lipids (1:2 molar ratio) or brain polar lipids (1:2 molar ratio). Purified protein with 0.1 % (w/v)

FC12, 0.01 % (w/v) CHS, 25 µM POPx was used for crystallization setups in presence or absence of citalopram or desipramine (1:2 molar ratio). Crystallization trials were setup using *in surfo*, CIMP or Bicelle method and plates were incubated at 4 °C, 16 °C or 21 °C (2.2.4.1). Various dilutions of reservoir solution used during CIMP crystallization were tested to influence the evaporation rate. Different molar ratios of DMPC:CHAPSO have been tested for Bicelle experiments. So far, no crystals have been observed with *in surfo* or Bicelle method. Sharp fluorescent signal upon UV illumination have been observed in several conditions using the CIMP crystallization method and Cubic Phase or MbClass screening solutions. Three different examples are shown in Figure 3.31 A-F. These strong fluorescing materials were harvested and used for diffraction experiments at PETRA III beam line (DESY, Hamburg). No diffraction was observed for any of the tested material.

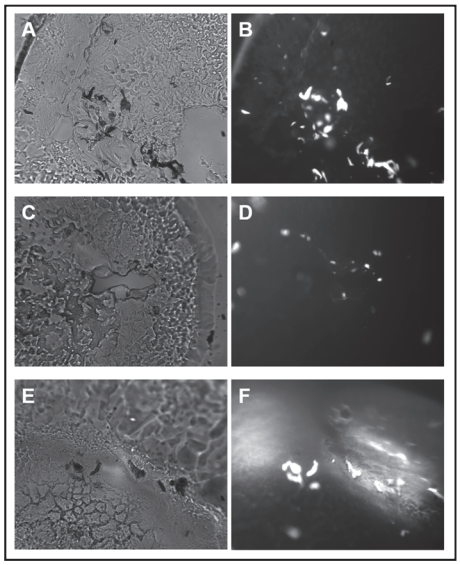

Figure 3.31: Crystallization screening of N-His_8-hSERT using CIMP method. **(A)** VIS light and **(B)** UV light microscope pictures of experiments with Cubic Phase I – E4 (1.2 M Na/K phosphate; pH 7.0) **(C)** VIS light and **(D)** UV light microscope pictures of experiments with Cubic Phase II – B12 (10 mM $MgCl_2$; 10 mM $CaCl_2$; 100 mM TRIS pH 8.2; 20 % (w/v) PEG 550 MME). **(E)** VIS light and **(F)** UV light microscope pictures of experiments with MbClass – H12 (1 M Trisodium citrate).

4 Discussion

4.1 Expression, purification and crystallization of hSERT

4.1.1 Expression in the bacterial system, purification, reconstitution and crystallization of hSERT

Expression of C-Rho-hSERT in the bacterial system (3.2.1.1) showed low overall expression levels together with a weak basal expression. Prolonged expression times (> 4 h) were found to increase the amount of aggregated protein, which could be due to the accumulation of misfolded hSERT as inclusion bodies. The presence of proteolytic digestion products could also indicate the toxicity of the expressed protein for the host cell.

Purification of C-Rho-hSERT with a customized serotonin resin (3.3.2) showed that the majority of protein did not bind to the resin. Only a small amount of hSERT was found in the elution fraction. Prior to the development of the custom resin, the length of the permeation pathway (i.e. the distance from the extracellular surface to the central binding site) was estimated based on the available LeuT structure. A PEG spacer was included between the bead and the serotonin molecule to avoid steric hindrance. A possible explanation for this result could be, that only a small fraction of protein is in a functional conformation and able to bind to the serotonin molecule. Alternatively, it is possible that the protein is simply retarded through non-specific interactions with the resin and elutes with the liquid flow.

The SEC elution profile after antibody affinity purification (3.3.3.) revealed three peaks where the first peak is close to the exclusion volume of the column indicating a highly aggregated state of C-Rho-hSERT. The remaining two peaks were not well separated with elution volumes corresponding to a MW of ~ 440 kDa and ~ 300 kDa, respectively. Due to the presence of contaminating bands the estimated molecular weights based on the elution volume cannot be assigned to the respective oligomeric state of Rho-hSERT. The identity of purified C-Rho-hSERT was confirmed by mass spectroscopic analysis, but the overall purity was too low for biophysical characterization or crystallization of C-Rho-hSERT.

Expression of N-His_8-hSERT in the bacterial system (3.2.1.2) was analyzed using different *E. coli* BL21(DE3) strains, different media, different expression temperatures and in presence or absence of chemical chaperones sorbitol and betaine. When using TB medium, expression was only found for the strains RP and Lemo21. In contrast to that, expression in all tested strains was observed when auto-induction medium was used. This result indicates that the expression of hSERT is rather dependent on the medium composition than the cell strain.

The expression of the gene encoding the target protein in BL21(DE3) strains is under the control of the T7 promoter, which is recognized by T7 RNA polymerase (RNAP). The RNAP

gene is located in the chromosome and its expression is under control of the non-titratable, IPTG-inducible lacUV5 promoter. Addition of IPTG to the expression medium induces expression of RNAP, which in turn is needed for the expression of target protein. The strain Lemo21 is a BL21(DE3) derivative that contains a plasmid encoding T7 lysozyme, an inhibitor of T7 RNA polymerase, which is under control of the well-titratable rhamnose promoter. Therefore, activity of T7 RNAP can be modulated in presence of L-rhamnose and was found to be the key for optimizing the ratio of membrane proteins properly inserted in the membrane to non-inserted proteins. Furthermore, adverse effects (e.g. toxicity) of membrane protein expression in *E. coli* are reduced [221]. Expression level of Lemo21 with 0 or 100 µM L-rhamnose is comparable to that obtained with RP. The maximum expression level was reached 4 h post induction in the absence of L-rhamnose, while the presence of 100 µM L-rhamnose appears to shift the maximum expression level towards later stages (Figure 3.4). Concentrations above 100 µM were found to abolish target protein expression.

Published data regarding expression of rat SERT in the bacterial system revealed that the target protein is found in the form of insoluble aggregates and is susceptible to in vivo truncation due to proteolysis [219]. Improvements were made by decreasing expression temperature and by growing E. coli in presence of chemical chaperones sorbitol and betaine, which led to an increased expression level and a reduced proteolysis level [219]. Therefore, expression of hSERT in presence or absence or chemical chaperones was analyzed (3.2.1.3). In this study, the results showed a decreased expression level or abolished expression in presence of chemical chaperones compared to that of the control experiment. Furthermore, a reduction of proteolytic degradation in presence of sorbitol and betaine was not observed as all the analyzed samples showed degradation of the target protein. These results are in contrary to the published results, which might be due to different expression vectors and cell strains used in this study. Interestingly a positive effect on protein solubilization was observed for these additives, which are small compared to detergents. Among the control experiments, the highest expression level for hSERT was found for the combination of *E. coli* RP with ZY-based auto-induction medium and was therefore used as the standard expression protocol. Surprisingly, no expression was observed for Lemo21 and C43 when using auto-induction medium, which is in contrast to the previous dot blot expression analysis. A possible explanation for this contrary observation could be a proteolytic degradation of target protein that leads to the cleavage of the N-terminal His-tag, which will be separated by SDS-PAGE but remains present in the dot blot.

The detergent screen for N-His_8-hSERT (3.3.1.1) with a range of nonionic and zwitterionic detergents revealed, that all analyzed zwitterionic detergents are able to completely solubilize the target protein. Among the nonionic detergents, only DDM was able to solubilize at least ~ 50 % of hSERT from the membrane. Nonionic detergents disrupt protein-lipid and lipid-lipid

interactions rather than protein-protein interactions and are known to be mild and nondenaturing, whereas ionic detergents disrupt protein-protein interactions. Ionic detergents are considered as harsh and tend do denature the protein. Zwitterionic detergents like Fos-cholines are intermediates between nonionic and ionic detergents in their mildness. They are electrically neutral like nonionic detergents but can disrupt protein-protein interactions like ionic detergents [222,223]. The finding, that only zwitterionic detergents are able to completely solubilize the protein might be due to strong protein-lipid interactions in the membrane. The preference of hSERT for the Fos-choline group detergents might be due to the lipid-mimicking effect from these detergents which assist in retaining a proper folding of the transmembrane domains of hSERT [224]. Among the Fos-cholines, FC14 revealed a greater fraction of degraded hSERT compared to FC12 (Figure 3.16), therefore solubilization only with FC12 was further optimized. It could be shown that a solubilization duration of 2 h is sufficient to completely solubilize hSERT.

Previously obtained experimental data indicated that hSERT is an oligomer in the membrane [225]. It was suggested, that hSERT forms a dimer with functional interactions between subunits and that dimers can associate to a higher order complex, most possibly a tetramer. These oligomeric complexes were stable in detergent solutions even under conditions that abolished the transporter's ability to bind high affinity ligands [226]. More recent research found that hSERT is a monomer in detergents [118]. In the present study, the final purification step by SEC revealed a single elution peak for both FC12 and DDM purified hSERT that corresponds to an apparent MW of ~300 and ~320 kDa, respectively. The apparent MW of ~300 kDa indicates indeed a tetrameric form of hSERT within a single FC12 micelle. An estimation of the oligomeric state of DDM purified hSERT was not possible due to contaminations but considering the size of a DDM micelle (~72 kDa), it seems reasonable that hSERT in DDM is an oligomer rather than a monomer. SEC purification of hSERT in FC14 revealed two peaks that are poorly separated. The elution volumes correspond to an apparent MW of ~ 180 and ~ 110 kDa, respectively. The apparent MW of the second peak would ideally correspond to the monomeric form of hSERT, but analysis of the peak fraction showed that most of the protein has been degraded and only a small fraction represents the full-length protein. The present data shows that hSERT in FC12 is an oligomer, though it seems possible that the order of the oligomeric state depends on the nature of the detergent. Human SERT could probably exist as monomer in FC14, though the proteolytic degradation suggests detergent induced denaturation. Due to the relatively high yield and a high purity, purification of hSERT with FC12 was selected as the standard protocol.

Even though it was possible to improve the thermostability of purified hSERT to minimize temperature dependent aggregation of the protein during crystallization, it was not possible to obtain diffracting crystals from any of the screened crystallization conditions. The reason for

this could be a structural inhomogeneity of the purified sample which prevents crystallization of the protein. During the experimental phase of this study, the first x-ray crystal structure of hSERT was published by Coleman et al [118].

4.1.2 Expression in the insect cell system and purification of hSERT

Expression analysis of C-Rho-hSERT and C-His_8-hSERT in the insect cell system vector was carried out by Cube Biotech (Monheim). In both cases, the multiplicity of infection (MOI) was varied between 1 and 5 to optimize the expression level, which should positively correlate with the MOI. In this study, the expression levels were found to be independent of the MOI. This effect has been observed, when cells were transfected at an early growth phase [227]. Both proteins were successfully solubilized and purified using affinity chromatography, but both proteins degraded during the SEC run irrespective of the used detergent.

4.2 Secondary structure of *E. coli* expressed hSERT

Initially, the secondary structure content of hSERT purified with DDM or FC12 was analyzed by CD spectroscopy. The obtained spectra were deconvoluted using Dichroweb [181] and BeStSel [228] webserver. Using BeStSel, the estimated α-helical content is 20 pp lower (~30 %) and the content for turns and unordered regions is 20 pp higher (~55 %) compared to Dichroweb. The estimated β-sheet content is within the same magnitude (~15 %) for both methods. Indeed, the deconvolution algorithm of BeStSel is optimized for β-sheet-rich proteins (e.g. amyloid fibrils) and allows the precise determination and distinction of different β-structures such as parallel, antiparallel and twisted β-sheets. In contrast to that, the SERT is a membrane protein with a relatively high content of α-helical structures that make up to 60 % of the protein's total secondary structure [118,141]. The reference data set SMP180 [182] used for deconvolution with Dichroweb contains the spectra of 30 membrane proteins that covers the secondary structure and fold space of all known membrane proteins as of June 2011. While both methods appear to be equivalent in terms of β-sheet structure estimation for hSERT, the BeStSel method seems to underestimate α-helical content and overestimate turns and unordered regions, respectively, and was therefore not considered for further analysis. Based on the results obtained with Dichroweb, the FC12 purified hSERT has the determined secondary structural content close to that of the published crystal structure. The DDM purified hSERT showed relatively a lower content for α-helical structure and a higher content for β-sheets and turn regions. In case of the DDM purified hSERT, this result could indicate an aggregation induced α-helix to β-sheet transition [229].

The influence of lipids on the secondary structure of FC12 purified hSERT was analyzed to optimize the secondary structure content. The neuronal lipid extract resembles the native lipid environment of neuronal membranes. Addition of NL during the final purification step improved the α-helical content, but simultaneously it aggravated the structural content of β-sheet and turn region. In contrast, the effect of cholesterol, which is known to affect conformation and transport activity [230,231], on the secondary structure is relatively small. The overall shift of 2 pp from α-helix and β-sheet structures towards turn regions affects ~12 residues. The combination of both compounds, CHS and NL, leads to an improvement in both α-helical and β-sheet structure. A similar effect was observed when CHS was combined with a mixture of phospholipids (POPx) that have been successfully used to stabilize SERT during crystallization [118]. Here, further improvement in α-helical content is followed by a further reduction in turn region content. Even though the combination of cholesterol and lipids could improve the secondary structure content of hSERT, the α-helix and β-sheet content is up to 10 pp higher than expected from the solved crystal structure. It is known that the protein-to-lipid ratio affects the α-helix and β-sheet content and it might be necessary to increase the lipid concentration in order to improve the secondary structure [232]. Furthermore, one has to bear in mind that the method of CD spectroscopy measures the average ellipticity of all protein molecules present in the sample. For example, a measured β-sheet content of 10 % does not necessarily mean that all protein molecules contain 10 % of β-sheet. Instead, this is the average number and the results can be interpreted with the reasonable assumption that a certain fraction of the molecules contains more than 10 % β-sheet, while the remaining fraction contains a lower β-sheet content that is closer to the expected values. This would suggest that at least a fraction of the purified protein is misfolded and probably impaired in its functionality.

The influence of two SSRIs (citalopram, fluoxetine) and one TCA (desipramine) on the secondary structure of hSERT was analyzed. Differences between samples were relatively small and within the range of 1-3 pp, which affect approximately 6-20 residues. The underlying mechanism of substrate transport predicts large conformational changes between the outward-open and inward-open state, which was confirmed for the leucine transporter (LeuT) [233], a bacterial homologue of hSERT. The large conformational change of the tertiary structure is accompanied by a relatively small change of the secondary structure: comparing the LeuT secondary structure content based on DSSP annotation [234] between substrate unbound outward-open (PDB: 3TT1) and substrate unbound inward-open (PDB: 3TT3) conformation shows that indeed only 9 residues were affected in their secondary structure contribution leading to a shift of 1 pp between α-helix and turn structure. Changes in the secondary structure of hSERT between unbound (PDB: 5I6Z) and SSRI-bound (PDB: 5I6X, 5I71, 5I73, 6AWN, 6AWO, 6AWP) state is within the range of 1-4 pp between α-helix and turns structure and affects 6-24 residues. While the magnitude of overall secondary structure change is in

close agreement with the observed values in this study, this could not be confirmed for the direction of change. For example, binding of (S)-citalopram induced an increase of α-helical structure, while the crystal structure indicates a loss in α-helical residues. The solved crystal structures are missing a part of the C- and N-terminal domain, and the latter one is known to contain several α-helical residues [125]. It is possible, that the loss of a-helical structure reported in the crystal structure is compensated by an increase of α-helical residues in the missing termini, which would explain the discrepancy between published and observed values.

4.3 Thermostability of *E. coli* expressed hSERT

Thermostability of hSERT and the influence of detergents, lipids and SERT specific inhibitors was analyzed using different methods. The thermostability of FC12 or DDM purified hSERT was assayed using DSF (3.5.2.1) and CD spectroscopy (3.5.2.2) and both assays are sensitive for different orders of protein structure. The DSF assay is based on a fluorescent dye that binds to specific solvent accessible residues. Upon heating, the protein starts to unfold, and previously buried residues get exposed to the solvent, allowing newly exposed residues to bind dye molecules, thus leading to an increase in the fluorescence intensity. This method is therefore sensitive to changes in the protein's tertiary structure. In contrast to that, the method of CD spectroscopy measures the ellipticity at 222 nm, which is sensitive to changes in the α-helical secondary structure. In both methods the measured signal is plotted as a function of temperature. For the DSF assay, the inflection point of corresponding transitions can be extracted from the first derivative plot. The first melting temperature (T_{m1}) for hSERT with FC12 and DDM using CPM was determined as 26 °C and 27 °C, respectively, while the T_{m1} using ANS dye was 23 °C for both samples. The strong fluorescence increase usually suggests a significant fraction of folded protein. As the transporter is known to exist in two different conformations depending on the occupancy of ion and substrate binding sites (1.2.1.2), it seems possible that the observed transition temperature describes a structural rearrangement from outward-open to inward-open conformation. Usually binding of substrate decreases the activation energy to switch from one state to the other, but it can alternatively be induced through heating. Another possible explanation could be due to heat-induced disaggregation of tetrameric hSERT into protein monomers and thereby changing the quaternary structure. Interestingly, the second melting point (T_{m2}) for hSERT with FC12 and DDM using CPM, which was determined as 43 °C and 54 °C, respectively, is in close agreement with the T_m values of 46 °C and 57 °C, respectively, obtained from CD spectroscopy at 222 nm. This shows that changes in the secondary structure as well as in the tertiary structure of hSERT are closely related and the obtained melting temperatures in presence of DDM or FC12 have been validated with two independent methods. In contrast to that, the T_{m2} obtained from DSF using

ANS dye shows a higher T_m for FC12 (71 °C) over DDM (67 °C) and these values are ~10-25 °C higher compared to those obtained from CD spectroscopy. The different results between CPM and ANS can be explained with the different dye binding properties: CPM binds to the solvent accessible thiol group of free cysteines [188], which will be exposed during protein unfolding, while ANS binds to the hydrophobic region of the protein [189,235], which is masked by detergent molecules, or to the detergent micelles itself. This suggests that ANS is not suitable for a reliable determination of the transporter's melting temperature in detergent solutions.

Based on the results obtained from CD spectroscopy, DDM purified hSERT revealed a higher T_m compared to FC12 purified hSERT, while the latter showed better secondary structure content (3.5.1.1) and was selected for further optimization of thermostability (3.5.2.2). Surprisingly, inclusion of NL or CHS or both during the final purification step reduced the thermostability. A combination of CHS and POPx finally increased the thermostability by ~7 °C, yielding a T_m of ~54 °C, which is close to the T_m determined for DDM purified hSERT (57 °C). This condition was considered as the gold standard for crystallization and binding experiments. Compared to previously published melting temperatures for mammalian expressed hSERT of 28 °C [236] and 40 °C [237], respectively, *E. coli* expressed hSERT has a higher stability, especially in presence of CHS and POPx. The published lower melting temperatures are probably due to the different assay method used for T_m determination. In both cases, the reported melting temperature is based on the ability of hSERT to bind inhibitor molecules. This ability is not directly reflected by fluorescence or CD spectroscopy used in this study.

Finally, the influence of inhibitors on the thermostability was analyzed using CD (3.5.2.3) and intrinsic Trp fluorescence (3.5.2.4) spectroscopy. Based on the results obtained from CD spectroscopy, all inhibitors revealed a tendency to destabilize hSERT. The destabilizing influence of desipramine and fluoxetine on T_m obtained from secondary structure was marginal, while citalopram showed a substantial decrease of the T_m by ~7 C. The melting curve obtained from intrinsic Trp fluorescence showed a biphasic behavior, indicating the presence of a three-state melting transition. The values for T_{m1} among different samples are relatively close to each other and within the range of ~27-28 °C. As initially discussed in this section for the DSF assay, the first T_m could be related to either conformational switching from outward-open to inward-open state or the disaggregation of hSERT oligomers. The separation into monomers as a stable intermediate exposes Trp residues that have been previously buried within the tetramer. Regarding the fitting function described in equation 7 (2.2.3.2), the hSERT oligomer or outward-open conformation, respectively, is considered as structural element E_1, while the monomer or inward-open conformation, respectively, is considered to be structural element E_2. The second T_m corresponds to the protein's tertiary structure unfolding but compared to the

secondary structure melting temperatures obtained from CD experiments, the values for T_{m2} are generally higher (~5-10 °C) and the destabilizing effect of desipramine and fluoxetine in regard to the control sample is stronger (~8 °C). This means that changes in the secondary structure occur prior to changes in the tertiary structure that can be observed with intrinsic Trp fluorescence. The close relation between melting temperatures obtained from CD spectroscopy and extrinsic fluorescence could not be confirmed for CD spectroscopy and intrinsic Trp fluorescence. This difference might be due to local quenching effects of Trp residues.

In contrast to desipramine and fluoxetine, a small stabilizing effect on the protein structure (~3 °C) was observed for citalopram using intrinsic Trp fluorescence experiments. It has been shown that proteins can be stabilized or destabilized by different ligands and one explanation for this phenomenon is the preference of a ligand to bind to a specific folding state of a protein [238,239]. Apparently, desipramine as well as fluoxetine preferentially bind to the partially unfolded, non-native state of hSERT, probably by non-specific hydrophobic interactions, and thereby stabilize the non-native state, which results in a decreased thermostability as shown in two different assays. Citalopram, on the other hand, preferentially binds to the folded native state of hSERT and stabilizes this state resulting in an increased thermostability. Another explanation in regard to the destabilizing effect of desipramine and fluoxetine is that binding of a ligand in one region of the protein triggers unfolding of the protein in another region. Either way, both inhibitors act as a catalyst that reduces the activation energy required for protein unfolding. This is surprising as most pharmaceutical ligands stabilize the native state and increase thermostability compared to the ligand unbound state [238,240].

4.4 Functionality of *E. coli* expressed hSERT

Binding of inhibitors to detergent purified N-His8-hSERT expressed in *E. coli* was analyzed using microscale thermophoresis (MST; 3.5.3.1) and surface plasmon resonance (SPR; 3.5.3.2). A broad concentration range (20 pM-20 mM) of citalopram, desipramine and fluoxetine was assayed using MST. No specific binding was observed during these experiments and higher concentrations of inhibitor (> 100 µM) led to unspecific binding. For future *in vitro* substrate uptake assays in a near-native environment, hSERT was reconstituted into liposomes and ligand binding measurements using intrinsic Trp fluorescence were performed. The reconstituted sample as well as the control sample (empty liposomes) showed only an unspecific binding for the analyzed inhibitor concentrations (300 pM-1 mM) suggesting a low affinity folding state of hSERT or a wrongly oriented lipid-bilayer-insertion of the protein. Many proteins prefer a unidirectional insertion [164] and in this regard it is possible that hSERT was unidirectionally inserted into the liposomes but in the wrong orientation, i.e. the outward-

open conformation facing the liposome's lumen and therefore preventing access to the binding site for inhibitor molecules that are present in the outside medium. Moreover, though the western blot analysis after liposome reconstitution experiment confirmed the presence of hSERT as full-length protein without any degradation products (3.4.1), it was not possible to discriminate between peripherally associated protein and bilayer-embedded protein.

Binding of desipramine (50 pM-500 nM) to *E. coli* expressed hSERT in FC12 detergent was observed during SPR spectroscopy measurements (3.5.3.2). Kinetic rate constants were determined using the Langmuir 1:1 binding model for non-linear regression analysis of sensorgrams. To the author's best knowledge, the present study is the first report of kinetic binding constants obtained from detergent purified hSERT using SPR spectroscopy. Compared to desipramine binding to hSERT expressed in human embryonic kidney (HEK-293) cells [241], the obtained association rate constant k_a is reduced by two orders of magnitude (1.1×10^4 vs. 6.1×10^6 $M^{-1}s^{-1}$) while the dissociation rate constant k_d is reduced by one order of magnitude (0.03 vs. 0.5 s^{-1}). The equilibrium dissociation constant k_D as the ratio of k_d and k_a was determined as ~2.8 µM. The affinity of *E. coli* expressed hSERT towards inhibitors is therefore up to three orders of magnitude lower compared to HEK-293 expressed hSERT, which is known to be in the nanomolar range [241–243]. The present result is in agreement with the previously reported dissociation constant of ~1 µM for *E. coli* expressed hSERT binding to imipramine and paroxetine [219]. This shows that detergent mediated isolation of hSERT affects the binding kinetics only to a small extent. The lower affinity compared to the native hSERT is more likely the result of missing lipids and cholesterol, that would keep the transporter in a high-affinity state. Addition of lipids and cholesterol improved the secondary structure, but due to high unspecific binding of both substances on the NTA sensor chip surface, the SPR experiments had to be carried out in absence of these compounds. It has been shown that depletion of the cholesterol level in membranes derived from HEK-293 cells stably expressing rat SERT (rSERT) reduced the binding affinity for substrate and inhibitors as well as the maximum transport rate [231,244]. This effect was found to be reversible as restoration of cholesterol levels in depleted membranes correlated with a reversal of the depletion-mediated affinity decrease and restored the previous high-affinity binding state. It was therefore concluded, that cholesterol is needed to stabilize the transporter in its optimally active form. It seems reasonable that inclusion of cholesterol could turn *E. coli* expressed hSERT into its high-affinity state with rate constants comparable to those obtained from HEK-293 cells. Microscale thermophoresis is a method that is compatible with the presence of lipids and cholesterol, but results based on this method did not indicate specific binding. To overcome the limitations imposed by the sensor chip surface, it appears advisable to reconstitute hSERT in cholesterol supplemented liposomes and immobilize the reconstituted

liposomes on an L1 sensor chip. This would eliminate the need of lipids and cholesterol to be present in the SPR running buffer. Furthermore, two different crystal structures of hSERT (PDB: 5I74; 5I6X) show presence of DDM or its dodecane chain, respectively, at the allosteric binding site. Both DDM and FC12 are structurally similar in this respect that they share the same dodecane chain and it seems reasonable that also FC12 can occupy the allosteric site, thereby preventing access for desipramine to the allosteric site at concentrations below 500 nM. This further supports the need of liposomes to avoid the presence of detergents. It is also possible that the lipids used in this study are not suitable to keep hSERT in a high-affinity conformation and that other lipid mixtures need to be tested, e.g. a mixture of phospholipids, galactolipids and cholesterol [245].

Furthermore, the response at equilibrium across different inhibitor concentrations was analyzed to verify the k_D obtained by kinetic evaluation. This attempt did not allow a conclusive evaluation as the number of different concentrations is not sufficient, and the maximum analyte concentration is well below the obtained k_D. For the same reason, it is not possible to exploit linearization methods for a reliable determination of the equilibrium constant k_D. The curve shape of the Scatchard plot indicates non-specific binding, negative cooperativity or multiple classes of binding sites with differing k_D values [246]. The Hill plot analysis (Figure 4.1 C) allows differentiating cooperativity and multiple binding sites and in this case indicates a negative cooperativity binding mode, although the linearity of data points is highly questionable. Additionally, the observed Rmax (37 RUs) was found to be almost twice the theoretical Rmax (19 RUs), which suggests the existence of additional binding sites. Therefore, three biphasic models have been developed and applied for non-linear regression analysis of SPR sensorgrams. These models accounted for two binding sites (heterogeneous ligand) or conformational changes (induced fit, conformational selection) that are expected to appear during binding of analyte molecules. With none of these models it was possible to determine a global association rate constant k_a. Instead, association rate constant and analyte concentration were found to be anticorrelated indicating that the number of fitting parameters is not sufficient, and the underlying model might be more complex. However, increasing the number of parameters also increases the chance to obtain several possible fitting solutions rather than one single valid solution, as several parameters have to be fitted simultaneously. Using starting values for the fitting parameters that are as close as possible to the real values can minimize this risk, but this attempt requires good estimates of the parameters.

According to the current knowledge, it is not clear whether desipramine would bind to the allosteric site in hSERT. Initially, it was found that 5-HT, but neither fluoxetine nor desipramine have an allosteric effect on the dissociation rate [123]. Later on, a weak allosteric effect was confirmed for fluoxetine [247], but results from competitive binding experiments with desipramine are not available. So far, structural evidence of desipramine being located at the

allosteric site was only found with LeuT [248] where it acts as a negative allosteric modulator and inhibits substrate binding, release and transport [248,249]. The SSRI S-citalopram was identified at the allosteric site in a recent hSERT crystal structure [118]. Besides the similarity between LeuT and hSERT of 40-45 %, structural or experimental evidence for the presence or absence of desipramine at the allosteric binding site in hSERT remains to be presented. Molecular docking simulations using SwissDock [250] based on the available x-ray structure with S-citalopram occupying both sites (PDB: 5I73) showed that desipramine can bind to both sites without steric hindrance (Figure 4.1). Based on the structural and experimental evidence of a low-affinity allosteric binding site, a model was developed that accounts for allosteric modulation between binding sites during association and dissociation. For the dissociation phase, three k_d values could be globally determined with a very low Chi² indicating a good fit of the model to the experimental data. Existence of a triphasic dissociation phase is further supported by the results obtained by fitting a series of simple mono- or multiphasic exponential functions to the data of the dissociation phase. However, due to the complexity of the association phase equation with six different rate constants ($3 \times k_a$; $3 \times k_d$), it was not possible to execute this equation in Origin or GraphPad Prism and k_a values could not be determined. Even with dedicated software that is capable of calculating complex equations, the obtained results remain unreliable. As previously mentioned, an increasing number of fitting parameters simultaneously increases the chance to obtain several possible fitting solutions. The complexity of models that can be used for a reliable kinetic evaluation is therefore limited. The best-fit solution for simple mono- or multiphasic exponential association suggests a tetraphasic association process, in which binding to either site is allosterically modulated through occupancy of the respective other binding site. The allosteric site is located in the permeation pathway above the central binding site and occupancy of the allosteric site can prevent association to and dissociation from the central binding site through steric hindrance, thereby reducing the respective rate constants. Conversely, it remains unclear how occupancy of the central site could modulate association (but not dissociation) for the allosteric site, which would give rise to a fourth association rate constant.

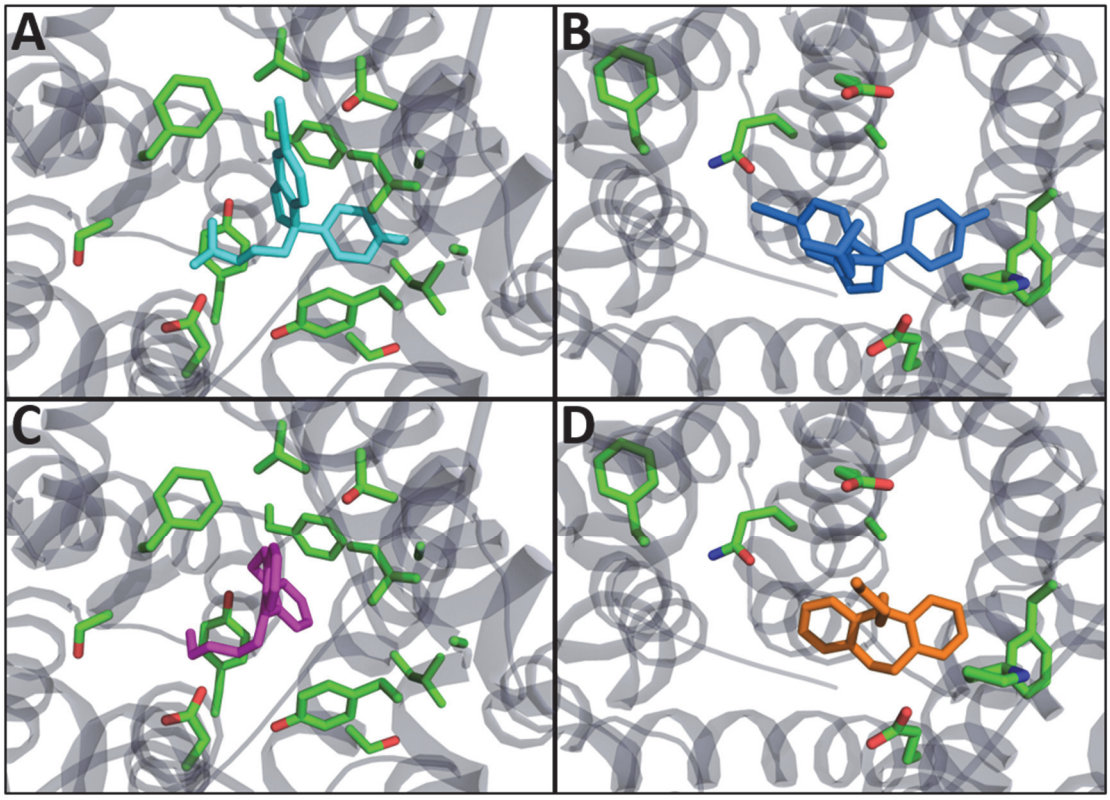

Figure 4.1: Citalopram and desipramine located at the central and allosteric site of hSERT. **(A)** S-citalopram (cyan) located at the central binding site (PDB: 5I73). **(B)** S-citalopram (blue) located at the allosteric binding site (PDB: 5I73). **(C)** Best solution for molecular docking simulation of desipramine (magenta) located at the central binding site. **(D)** Best solution for molecular docking simulation of desipramine (orange) located at the allosteric binding site. Residues forming the respective binding site are shown as green stick model.

Based on the results presented in this study, the observed Rmax cannot be explained with a model that contains only two binding sites. This also would require 99% of the captured protein molecules to be in a functional conformation. Instead, the observed Rmax could be related to additional unspecific binding sites. However, kinetic rate constants could be determined using a single site model suggesting that desipramine binds only to the primary S1 site. The relatively high Rmax can be explained by the binding of analyte molecule to hSERT in oligomeric state. Dynamic light scattering analysis of desipramine showed that the analyte molecules indeed exist in several oligomeric states, which makes it difficult to determine the amount of bound analyte. This means that binding of analyte oligomers increases the apparent SPR response without affecting the intrinsic binding kinetics.

Summary

Serotonin is a neurotransmitter and paracrine hormone that regulates a wide range of biological processes in humans through interaction with specific receptors. It affects the cardiovascular system, the nervous system and the gastrointestinal tract. The serotonin transporter translocate serotonin molecules from the synaptic cleft into the neuron, thereby terminating the serotonin induced signal transmission. Depression in humans can be related to an imbalanced serotonin household and is currently treated with selective serotonin reuptake inhibitors. Information about the transporter's structural data may guide the development of new antidepressants, that are superior in terms of efficacy, onset and adverse effects compared to currently available pharmaceuticals, by structure-based drug design. X-ray diffraction of protein crystals allows the determination of the structure with high resolution. However, this attempt requires a high amount of homogenous purified protein, and expression in bacterial system is much faster and less cost intensive compared to mammalian expression systems.

In this study, the human serotonin transporter was recombinantly expressed from bacterial or insect cell expression system. Protein expressed in insect cells could not be stabilized during purification. Overall yield and purity of C-terminal rho-tagged hSERT expressed in *E. coli* was found to be low. Large-scale protein production was established for the N-terminal his-tagged human SERT in *E. coli*. Optimized expression conditions, solubilization and purification protocols were developed that allowed to obtain moderate yields (~1.2 mg L^{-1} cell culture) of high purity protein that is suitable for downstream applications. Identity of target protein was confirmed by immunoblot and mass spectroscopy.

The secondary structure of FC12 purified hSERT was found to be in good agreement with known literature and could be further optimized by addition of cholesterol and a mixture of phospholipids. These additives also improved the thermal stability of *E. coli* expressed hSERT by ~7 °C. Results from fluorescence-based experiments were in close agreement with the results obtained from CD spectroscopy. Interaction with SSRIs or TCA led to small changes in the secondary structure content and in general to a lower thermal stability.

Binding of desipramine to FC12 purified hSERT was observed during SPR spectroscopy measurements in absence of cholesterol and phospholipids. The equilibrium dissociation constant k_D was determined as ~2.8 µM, showing that detergent mediated purification does not affect binding kinetics. The dissociation constant was determined assuming a 1:1 binding model, but data indicates a different stoichiometry. Fitting models that account for multiple binding sites or allosteric effects cannot describe the experimental data sufficiently. Alternatively, this can also be explained with binding of oligomeric analyte molecules.

Zusammenfassung

Serotonin ist ein Neurotransmitter und parakrines Hormon, das eine große Bandbreite von biologischen Prozessen im Menschen durch Interaktion mit spezifischen Rezeptoren reguliert. Es beeinflusst das kardiovaskuläre System, das Nervensystem sowie den Magen-Darm-Trakt. Der Serotonintransporter translociert Serotoninmoleküle über die Membran aus dem synaptischen Spalt ins Innere des Neurons und beendet damit die serotonininduzierte Signalübertragung. Depression beim Menschen wird in Verbindung mit einem unausgeglichenen Serotoninhaushalt in Verbindung gebracht und lässt sich unterstützend mit Hilfe von selektiven Serotonin-Wiederaufnahmehemmern therapieren. Informationen über die Struktur des Serotonintransporters könnte die Entwicklung neuer Medikamente ermöglichen, die den herkömmlichen Therapeutika in Bezug auf Wirksamkeit, Wirkungseintritt und unerwünschten Nebenwirkungen überlegen sind. Röntgenstrukturanalytische Untersuchungen von Proteinkristallen des Transporters ermöglichen die Bestimmung der Proteinstruktur mit hoher Auflösung. Diese Vorgehensweise benötigt allerdings verhältnismäßig große Mengen des homogen aufgereinigten Proteins und die Expression im bakteriellen System ist deutlich schneller und weniger kostenintensiv im Vergleich zur Expression mittels Säugetierzellen.

In der vorliegenden Studie wurde der humane Serotonintransporter im bakteriellen System sowie in Insektenzellen rekombinant exprimiert. In Insektenzellen exprimiertes Protein konnte während der Aufreinigung nicht ausreichend stabilisiert werden. Ausbeute und Reinheit des C-Terminal rho-markierten hSERT exprimiert in *E. coli* waren zu gering. Die Proteinproduktion mittels E. coli im Litermaßstab wurde für N-Terminal his-markiertes hSERT etabliert. Optimierte Protokolle für Expression, Solubilisierung und Aufreinigung wurden entwickelt. Diese ermöglichten eine moderate Ausbeute an hochreinem Protein welches geeignet für nachfolgende Experimente ist. Die Identität des Zielproteins wurde mittels Immunblot und Massenspektroskopie bestätigt.

Die mittels CD-Spektroskopie bestimmte Sekundärstruktur von aufgereinigtem hSERT passt gut zu den bisher bekannten Daten und konnte durch Zugabe von Cholesterol und Phospholipiden weiter verbessert werden. Diese Additive konnten auch die Thermostabilität von E. coli exprimiertem hSERT um ~7 °C verbessern. Die Ergebnisse der fluoreszene-basierten Experimente stimmen mit den Ergebnissen der CD-Spektroskopie sehr gut überein. Interaktion mit SSRIs oder TCA führt zu kleinen Änderungen der Sekundärstruktur und allgemein zu einer niedrigeren Thermostabilität.

Interaktion zwischen Desipramin und FC12 aufgereinigtem hSERT in Abwesenheit von Cholesterol und Phospholipiden konnte bei SPR-spektroskopischen Messungen beobachtet werden. Die Dissoziationskonstante k_D wurde mit 2.8 µM bestimmt, was darauf hindeutet, dass

die Bindungskinetik nicht durch Detergens beeinflusst wird. Die Dissoziationskonstante wurde unter Annahme eines 1:1 Bindungsmodells ermittelt, wobei die vorliegenden Daten eine andere Stöchiometrie vermuten lassen. Entsprechende Regressionsmodelle, welche mehrere Bindestellen sowie allosterische Effekte berücksichtigen, können die gemessenen Daten nicht hinreichend erklären. Alternativ kann dies durch Bindung oligomerer Analytmoleküle erklärt werden.

Bibliography

[1] SIEGEL GJ (1999) Basic neurochemistry. Molecular, cellular and medical aspects. 6th ed. Philadelphia, Pa.: Lippincott Williams & Wilkins.

[2] YOUNG SN, LEYTON M (2002) The role of serotonin in human mood and social interaction. *Pharmacol Biochem Behav* **71**, 857–865.

[3] MANN J (1999) Role of the Serotonergic System in the Pathogenesis of Major Depression and Suicidal Behavior. *Neuropsychopharmacology* **21**, 99S-105S.

[4] SODHI MSK, SANDERS-BUSH E (2004) Serotonin and brain development. In: SMYTHIES J *Disorders of Synaptic Plasticity and Schizophrenia*, 111–174. 1st ed. s.l.: Elsevier textbooks.

[5] RAPPORT MM, GREEN AA, PAGE IH (1948) Crystalline Serotonin. *Science* **108**, 329–330.

[6] HAMLIN KE, FISCHER FE (1951) The synthesis of 5-hydroxytryptamine. *J Am Chem Soc* **73**, 5007–5008.

[7] TURLEJSKI K (1996) Evolutionary ancient roles of serotonin. Long-lasting regulation of activity and development. *Acta Neurobiol Exp (Wars)* **56**, 619–636.

[8] NICHOLS DE, NICHOLS CD (2008) Serotonin receptors. *Chem Rev* **108**, 1614–1641.

[9] PARK S, KANG K, LEE SW, AHN M-J, BAE J-M, BACK K (2011) Production of serotonin by dual expression of tryptophan decarboxylase and tryptamine 5-hydroxylase in Escherichia coli. *Appl Microbio Biotechno* **89**, 1387–1394.

[10] PEROUTKA SJ, HOWELL TA (1994) The molecular evolution of G protein-coupled receptors. Focus on 5-hydroxytryptamine receptors. *Neuropharmacology* **33**, 319–324.

[11] GERSHON MD, TACK J (2007) The serotonin signaling system. From basic understanding to drug development for functional GI disorders. *Gastroenterology* **132**, 397–414.

[12] LESURTEL M, SOLL C, GRAF R, CLAVIEN P-A (2008) Role of serotonin in the hepato-gastroIntestinal tract. An old molecule for new perspectives. *Cell Mol Life Sci* **65**, 940–952.

[13] BERGER M, GRAY JA, ROTH BL (2009) The expanded biology of serotonin. *Annu Rev Med* **60**, 355–366.

[14] DIKSIC M, YOUNG SN (2001) Study of the brain serotonergic system with labeled α-methyl-l-tryptophan. *J Neurochem* **78**, 1185–1200.

[15] WILLIAMS WJ (2006) Williams hematology. 7th ed. New York, London: McGraw-Hill.

[16] MARIEB EN (2009) Essentials of human anatomy & physiology. 9th ed. San Francisco, Calif., London: Pearson Benjamin Cummings.

[17] LIU Q, YANG Q, SUN W, VOGEL P, HEYDORN W, YU X-Q, et al. (2008) Discovery and characterization of novel tryptophan hydroxylase inhibitors that selectively inhibit serotonin synthesis in the gastrointestinal tract. *J Pharmacol Exp Ther* **325**, 47–55.

[18] CÔTÉ F, THÉVENOT E, FLIGNY C, FROMES Y, DARMON M, RIPOCHE M-A, et al. (2003) Disruption of the nonneuronal tph1 gene demonstrates the importance of peripheral serotonin in cardiac function. *Proc Natl Acad Sci U S A* **100**, 13525–13530.

[19] HJORTH S, BENGTSSON HJ, KULLBERG A, CARLZON D, PEILOT H, AUERBACH SB (2000) Serotonin autoreceptor function and antidepressant drug action. *J Psychopharmacol (Oxford)* **14**, 177–185.

BOROWSKY B, HOFFMAN BJ (1995) Neurotransmitter Transporters. Molecular Biology, Function, and Regulation. In: BRADLEY RJ, HARRIS RA *International Review of Neurobiology*, 139–199. 1st ed. s.l.: Elsevier textbooks.

[21] AAN HET ROT M, MATHEW SJ, CHARNEY DS (2009) Neurobiological mechanisms in major depressive disorder. *CMAJ* **180**, 305–313.

[22] CULPEPPER L (2012) The use of monoamine oxidase inhibitors in primary care. *J Clin Psychiatry* **73 Suppl 1**, 37–41.

[23] KALGUTKAR AS, DALVIE DK, CASTAGNOLI N, TAYLOR TJ (2001) Interactions of Nitrogen-Containing Xenobiotics with Monoamine Oxidase (MAO) Isozymes A and B. SAR Studies on MAO Substrates and Inhibitors. *Chem Res Toxicol* **14**, 1139–1162.

[24] KLEIN DC (2007) Arylalkylamine N-acetyltransferase. "the Timezyme". *J Biol Chem* **282**, 4233–4237.

[25] The Neuron. Available: http://what-when-how.com/neuroscience/neurotransmitters-the-neuron-part-4/.

[26] HOYER D, CLARKE DE, FOZARD JR, HARTIG PR, MARTIN GR, MYLECHARANE EJ, et al. (1994) International Union of Pharmacology classification of receptors for 5-hydroxytryptamine (Serotonin). *Pharmacol Rev* **46**, 157.

[27] FREDRIKSSON R, LAGERSTRÖM MC, LUNDIN L-G, SCHIÖTH HB (2003) The G-protein-coupled receptors in the human genome form five main families. Phylogenetic analysis, paralogon groups, and fingerprints. *Mol Pharmacol* **63**, 1256–1272.

[28] TRZASKOWSKI B, LATEK D, YUAN S, GHOSHDASTIDER U, DEBINSKI A, FILIPEK S (2012) Action of molecular switches in GPCRs--theoretical and experimental studies. *Curr Med Chem* **19**, 1090–1109.

[29] DIGBY GJ, LOBER RM, SETHI PR, LAMBERT NA (2006) Some G protein heterotrimers physically dissociate in living cells. *Proc Natl Acad Sci U S A* **103**, 17789–17794.

[30] GILMAN AG (1987) G proteins. Transducers of receptor-generated signals. *Annu Rev Biochem* **56**, 615–649.

[31] MICHELL RH, KIRK CK, JONES LM, DOWNES CP, CREBA JA (1981) The Stimulation of Inositol Lipid Metabolism that Accompanies Calcium Mobilization in Stimulated Cells. Defined Characteristics and Unanswered Questions. *Philos Trans R Soc Lond, B, Biol Sci* **296**, 123–138.

[32] JORNAYVAZ FR, SHULMAN GI (2012) Diacylglycerol activation of protein kinase Cε and hepatic insulin resistance. *Cell Metab* **15**, 574–584.

[33] MILLAN MJ, MARIN P, BOCKAERT J, LA MANNOURY COUR C (2008) Signaling at G-protein-coupled serotonin receptors. Recent advances and future research directions. *Trends Pharmacol Sci* **29**, 454–464.

[34] THOMPSON A, R. LUMMIS S (2006) 5-HT3 Receptors. *CPD* **12**, 3615–3630.

[35] BARNES NM, HALES TG, LUMMIS SCR, PETERS JA (2009) The 5-HT3 receptor--the relationship between structure and function. *Neuropharmacology* **56**, 273–284.

[36] CAREY RJ, DEPALMA G, DAMIANOPOULOS E, SHANAHAN A, MÜLLER CP, HUSTON JP (2005) Evidence that the 5-HT1A autoreceptor is an important pharmacological target for the modulation of cocaine behavioral stimulant effects. *Brain Res* **1034**, 162–171.

[37] KENNETT GA, DOURISH CT, CURZON G (1987) Antidepressant-like action of 5-HT1A agonists and conventional antidepressants in an animal model of depression. *Eur J Pharmacol* **134**, 265–274.

[38] OOTSUKA Y, BLESSING WW (2006) Activation of 5-HT1A receptors in rostral medullary raphé inhibits cutaneous vasoconstriction elicited by cold exposure in rabbits. *Brain Res* **1073-1074**, 252–261.

[39] PARKS CL, ROBINSON PS, SIBILLE E, SHENK T, TOTH M (1998) Increased anxiety of mice lacking the serotonin1A receptor. *Proc Natl Acad Sci U S A* **95**, 10734–10739.

[40] POPOVA NK, AMSTISLAVSKAYA TG (2002) 5-HT2A and 5-HT2C serotonin receptors differentially modulate mouse sexual arousal and the hypothalamo-pituitary-testicular response to the presence of a female. *Neuroendocrinology* **76**, 28–34.

[41] POPA D, LÉNA C, FABRE V, PRENAT C, GINGRICH J, ESCOURROU P, et al. (2005) Contribution of 5-HT2 receptor subtypes to sleep-wakefulness and respiratory control, and functional adaptations in knock-out mice lacking 5-HT2A receptors. *J Neurosci* **25**, 11231–11238.

[42] MILLAN MJ, BROCCO M, GOBERT A, DEKEYNE A (2005) Anxiolytic properties of agomelatine, an antidepressant with melatoninergic and serotonergic properties. Role of 5-HT2C receptor blockade. *Psychopharmacology* **177**, 448–458.

[43] HEDLUND PB, HUITRON-RESENDIZ S, HENRIKSEN SJ, SUTCLIFFE JG (2005) 5-HT7 receptor inhibition and inactivation induce antidepressantlike behavior and sleep pattern. *Biol Psychiatry* **58**, 831–837.

[44] PEREZ-GARCÍA G, MENESES A (2005) Oral administration of the 5-HT6 receptor antagonists SB-357134 and SB-399885 improves memory formation in an autoshaping learning task. *Pharmacol Biochem Behav* **81**, 673–682.

[45] WESOŁOWSKA A, NIKIFORUK A (2007) Effects of the brain-penetrant and selective 5-HT6 receptor antagonist SB-399885 in animal models of anxiety and depression. *Neuropharmacology* **52**, 1274–1283.

[46] GOLDENBERG MM (2013) Pharmaceutical Approval Update. *Pharm Ther* **38**, 705–707.

[47] NELSON DL, LUCAITES VL, WAINSCOTT DB, GLENNON RA (1999) Comparisons of hallucinogenic phenylisopropylamine binding affinities at cloned human 5-HT2A, 5-HT2B and 5-HT2C receptors. *Naunyn-Schmiedeberg's Arch Pharmacol* **359**, 1–6.

[48] ODAGAKI Y, TOYOSHIMA R, YAMAUCHI T (2005) Trazodone and its active metabolite m-chlorophenylpiperazine as partial agonists at 5-HT1A receptors assessed by 35SGTP-gammaS binding. *J Psychopharmacol (Oxford)* **19**, 235–241.

[49] BOER SF de, KOOLHAAS JM (2005) 5-HT1A and 5-HT1B receptor agonists and aggression. A pharmacological challenge of the serotonin deficiency hypothesis. *Eur J Pharmacol* **526**, 125–139.

[50] HARRISON AA, PARSONS LH, KOOB GF, MARKOU A (1999) RU 24969, a 5-HT 1A/1B agonist, elevates brain stimulation reward thresholds. An effect reversed by GR 127935, a 5-HT 1B/1D antagonist. *Psychopharmacology* **141**, 242–250.

[51] KENNETT GA, AINSWORTH K, TRAIL B, BLACKBURN TP (1997) BW 723C86, a 5-HT2B Receptor Agonist, Causes Hyperphagia and Reduced Grooming in Rats. *Neuropharmacology* **36**, 233–239.

[52] MCCREARY AC, BANKSON MG, CUNNINGHAM KA (1999) Pharmacological Studies of the Acute and Chronic Effects of (+)-3,4-Methylenedioxymethamphetamine on Locomotor Activity. Role of 5-Hydroxytryptamine_{1A} and 5-Hydroxytryptamine_{1B/1D} Receptors. *J Pharmacol Exp Ther* **290**, 965.

[53] POPOVA NK, AMSTISLAVSKAYA TG (2002) Involvement of the 5-HT1A and 5-HT1B serotonergic receptor subtypes in sexual arousal in male mice. *Psychoneuroendocrinology* **27**, 609–618.

[54] TATARCZYNSKA E, KLODZINSKA A, STACHOWICZ K, CHOJNACKA-WOJCIK E (2004) Effects of a selective 5-HT1B receptor agonist and antagonists in animal models of anxiety and depression. *Behav Pharmacol* **15**, 523–534.

[55] ANTONACI F, GHIOTTO N, WU S, PUCCI E, COSTA A (2016) Recent advances in migraine therapy. *Springerplus* **5**, 637.

[56] DIAMOND S (2015) Headache and Migraine Biology and Management. Burlington: Elsevier Science.

[57] PITSIKAS N, BRAMBILLA A, BORSINI F (1994) Effect of DAU 6215, a novel 5-HT3 receptor antagonist, on scopolamine-induced amnesia in the rat in a spatial learning task. *Pharmacol Biochem Behav* **47**, 95–99.

[58] MICHEL K, ZELLER F, LANGER R, NEKARDA H, KRUGER D, DOVER TJ, et al. (2005) Serotonin Excites Neurons in the Human Submucous Plexus via 5-HT3 Receptors. *Gastroenterology* **128**, 1317–1326.

[59] WIT R de, AAPRO M, BLOWER PR (2005) Is there a pharmacological basis for differences in 5-HT3-receptor antagonist efficacy in refractory patients. *Cancer Chemother Pharmacol* **56**, 231–238.

[60] MENESES A, HONG E (1997) Effects of 5-HT4 Receptor Agonists and Antagonists in Learning. *Pharmacol Biochem Behav* **56**, 347–351.

[61] SMRIGA M, TORII K (2003) L-Lysine acts like a partial serotonin receptor 4 antagonist and inhibits serotonin-mediated intestinal pathologies and anxiety in rats. *Proc Natl Acad Sci U S A* **100**, 15370–15375.

[62] DICKSON EJ, HEREDIA DJ, SMITH TK (2010) Critical role of 5-HT1A, 5-HT3, and 5-HT7 receptor subtypes in the initiation, generation, and propagation of the murine colonic migrating motor complex. *Am J Physiol Gastrointest Liver Physiol* **299**, G144-57.

[63] BUNNEY WE, DAVIS JM (1965) Norepinephrine in depressive reactions. A review. *Arch Gen Psychiatry* **13**, 483–494.

[64] DELGADO PL (2000) Depression. The case for a monoamine deficiency. *J Clin Psychiatry* **61 Suppl 6**, 7–11.

[65] HIRSCHFELD RM (2000) History and evolution of the monoamine hypothesis of depression. *J Clin Psychiatry* **61 Suppl 6**, 4–6.

[66] SCHILDKRAUT JJ (1965) The catecholamine hypothesis of affective disorders. A review of supporting evidence. *Am J Psychiatry* **122**, 509–522.

[67] COPPEN AJ (1969) Biochemical aspects of depression. *Int Psychiatry Clin* **6**, 53–81.

[68] LAPIN IP, OXENKRUG GF (1969) Intensification of the central serotoninergic processes as a possible determinant of the thymoleptic effect. *Lancet* **1**, 132–136.

[69] DENCKER SJ, MALM U, ROOS BE, WERDINIUS B (1966) Acid monoamine metabolites of cerebrospinal fluid in mental depression and mania. *J Neurochem* **13**, 1545–1548.

[70] MENDELS J, FRAZER A, FITZGERALD RG, RAMSEY TA, STOKES JW (1972) Biogenic amine metabolites in cerebrospinal fluid of depressed and manic patients. *Science* **175**, 1380–1382.

[71] SHAW DM, CAMPS FE, ECCLESTON EG (1967) 5-Hydroxytryptamine in the hind-brain of depressive suicides. *Br J Psychiatry* **113**, 1407–1411.

[72] SHOPSIN B, FRIEDMAN E, GERSHON S (1976) Parachlorophenylalanine reversal of tranylcypromine effects in depressed patients. *Arch Gen Psychiatry* **33**, 811–819.

[73] SCHLOSS P, WILLIAMS DC (1998) The serotonin transporter. A primary target for antidepressant drugs. *J Psychopharmacol (Oxford)* **12**, 115–121.

[74] LUCKI I (1998) The spectrum of behaviors influenced by serotonin. *Biol Psychiatry* **44**, 151–162.

[75] DELAY J, LAINE B, BUISSON JF (1952) Note concernant l'action de l'isonicotinyl-hydrazide utilisé dans le traitement des états dépressifs. *Ann Med Psychol (Paris)* **110**, 689–692.

[76] ZELLER EA, BARSKY J (1952) In vivo Inhibition of Liver and Brain Monoamine Oxidase by 1-Isonicotinyl-2-Isopropyl Hydrazine. *P Soc Exp Biol Med* **81**, 459–461.

[77] HILLHOUSE TM, PORTER JH (2015) A brief history of the development of antidepressant drugs. From monoamines to glutamate. *Exp Clin Psychopharmacol* **23**, 1–21.

[78] WIMBISCUS M, KOSTENKO O, MALONE D (2010) MAO inhibitors. Risks, benefits, and lore. *Cleve Clin J Med* **77**, 859–882.

[79] KALUDERCIC N, CARPI A, MENABÒ R, DI LISA F, PAOLOCCI N (2011) Monoamine oxidases (MAO) in the pathogenesis of heart failure and ischemia/reperfusion injury. *BBA - Mol Cell Res* **1813**, 1323–1332.

[80] LEMKE TL (2008) Foye's principles of medicinal chemistry. 6th ed. Philadelphia, Pennsylvania: Lippincott Williams & Wilkins.

[81] OWENS MJ, MORGAN WN, PLOTT SJ, NEMEROFF CB (1997) Neurotransmitter receptor and transporter binding profile of antidepressants and their metabolites. *J Pharmacol Exp Ther* **283**, 1305–1322.

[82] THOMAS DR, NELSON DR, JOHNSON AM (1987) Biochemical effects of the antidepressant paroxetine, a specific 5-hydroxytryptamine uptake inhibitor. *Psychopharmacology* **93**, 193–200.

[83] CIRAULO DA, SHADER RI, GREENBLATT DJ (2011) Clinical Pharmacology and Therapeuticsof Antidepressants. In: CIRAULO DA, SHADER RI *Pharmacotherapy of depression*, 33–124. 2nd ed. New York: Humana Press.

[84]. FOYE WO, LEMKE TL, WILLIAMS DA (2013) Foye's principles of medicinal chemistry. 7th ed. Philadelphia: Wolters Kluwer Health/Lippincott Williams & Wilkins.

[85] PARDRIDGE WM (1979) The role of blood-brain barrier transport of tryptophan and other neutral amino acids in the regulation of substrate-limited pathways of brain amino acid metabolism. *J Neural Transm Suppl*, 43–54.

[86] HAWKINS RA, O'KANE RL, SIMPSON IA, VIÑA JR (2006) Structure of the blood-brain barrier and its role in the transport of amino acids. *J Nutr* **136**, 218S-26S.

[87] SHAW KA, TURNER J, MAR CD (2002) Tryptophan and 5-Hydroxytryptophan for depression. *Cochrane DB Syst Rev*.

[88] RICHARD DM, DAWES MA, MATHIAS CW, ACHESON A, HILL-KAPTURCZAK N, DOUGHERTY DM (2009) L-Tryptophan. Basic Metabolic Functions, Behavioral Research and Therapeutic Indications. *Int J Tryptophan Res* **2**, 45–60.

[89] VOLPI-ABADIE J, KAYE AM, KAYE AD (2013) Serotonin Syndrome. *Ochsner J* **13**, 533–540.

[90] FERRI FF (2016) Ferri's Clinical Advisor 2017. 5 Books in 1. 1st ed. s.l.: Elsevier Health Care - Major Reference Works.

[91] OLFSON M, MARCUS SC (2009) National patterns in antidepressant medication treatment. *Arch Gen Psychiatry* **66**, 848–856.

[92] MOJTABAI R, OLFSON M (2011) Proportion of antidepressants prescribed without a psychiatric diagnosis is growing. *Health Aff (Millwood)* **30**, 1434–1442.

[93] BYMASTER FP, ZHANG W, CARTER PA, SHAW J, CHERNET E, PHEBUS L, et al. (2002) Fluoxetine, but not other selective serotonin uptake inhibitors, increases norepinephrine and dopamine extracellular levels in prefrontal cortex. *Psychopharmacology* **160**, 353–361.

[94] RUTTER JJ, AUERBACH SB (1993) Acute uptake inhibition increases extracellular serotonin in the rat forebrain. *J Pharmacol Exp Ther* **265**, 1319–1324.

[95] CHARNEY DS (1981) Receptor Sensitivity and the Mechanism of Action of Antidepressant Treatment. *Arch Gen Psychiatry* **38**, 1160.

[96] OSWALD I, BREZINOVA V, DUNLEAVY DLF (1972) On the Slowness of Action of Tricyclic Antidepressant Drugs. *Br J Psychiatry* **120**, 673–677.

[97] ANDREWS PW, THOMSON JA (2009) The bright side of being blue. Depression as an adaptation for analyzing complex problems. *Psychol Rev* **116**, 620–654.

[98] PETTY F, KRAMER G, WILSON L, JORDAN S (1994) In vivo Serotonin release and learned helplessness. *Psychiat Res* **52**, 285–293.

[99] ZANGEN A, OVERSTREET DH, YADID G (1997) High serotonin and 5-hydroxyindoleacetic acid levels in limbic brain regions in a rat model of depression. Normalization by chronic antidepressant treatment. *J Neurochem* **69**, 2477–2483.

[100] ALBERT PR, BENKELFAT C, DESCARRIES L (2012) The neurobiology of depression--revisiting the serotonin hypothesis. I. Cellular and molecular mechanisms. *Philos Trans R Soc Lond, B, Biol Sci* **367**, 2378–2381.

[101] MAHAR I, BAMBICO FR, MECHAWAR N, NOBREGA JN (2014) Stress, serotonin, and hippocampal neurogenesis in relation to depression and antidepressant effects. *Neurosci Biobehav Rev* **38**, 173–192.

[102] POPOLI M, YAN Z, MCEWEN BS, SANACORA G (2011) The stressed synapse. The impact of stress and glucocorticoids on glutamate transmission. *Nat Rev Neurosci* **13**, 22–37.

[103] ANDREWS PW, BHARWANI A, LEE KR, FOX M, THOMSON JA (2015) Is serotonin an upper or a downer? The evolution of the serotonergic system and its role in depression and the antidepressant response. *Neurosci Biobehav Rev* **51**, 164–188.

[104] RUDNICK G, KRÄMER R, BLAKELY RD, MURPHY DL, VERREY F (2014) The SLC6 transporters. Perspectives on structure, functions, regulation, and models for transporter dysfunction. *Pflugers Arch* **466**, 25–42.

[105] LILL H, NELSON N (1998) [28] Homologies and family relationships among Na+/Cl− neurotransmitter transporters. In: AMARA SG *Neurotransmitter transporters*, 425–436. San Diego, Calif.: Acad. Press.

[106] AGGARWAL S, MORTENSEN OV (2017) Overview of Monoamine Transporters. *Curr Protoc Pharmacol* **79**, 12.16.1-12.16.17.

[107] BLAKELY RD, FELICE LJ de, HARTZELL HC (1994) Molecular physiology of norepinephrine and serotonin transporters. *J Exp Biol* **196**, 263–281.

[108] LESCH KP (2001) Serotonergic gene expression and depression. Implications for developing novel antidepressants. *J Affect Disord* **62**, 57–76.

[109] NAKAMURA M, UENO S, SANO A, TANABE H (2000) The human serotonin transporter gene linked polymorphism (5-HTTLPR) shows ten novel allelic variants. *Mol Psychiatry* **5**, 32–38.

[110] HEILS A, TEUFEL A, PETRI S, SEEMANN M, BENGEL D, BALLING U, et al. (1995) Functional promoter and polyadenylation site mapping of the human serotonin (5-HT) transporter gene. *J Neural Transmission* **102**, 247–254.

[111] HEILS A, TEUFEL A, PETRI S, STÖBER G, RIEDERER P, BENGEL D, et al. (1996) Allelic Variation of Human Serotonin Transporter Gene Expression. *J Neurochem* **66**, 2621–2624.

[112] LESCH K-P, BENGEL D, HEILS A, SABOL SZ, GREENBERG BD, PETRI S, et al. (1996) Association of Anxiety-Related Traits with a Polymorphism in the Serotonin Transporter Gene Regulatory Region. *Science* **274**, 1527–1531.

[113] PEZAWAS L, MEYER-LINDENBERG A, DRABANT EM, VERCHINSKI BA, MUNOZ KE, KOLACHANA BS, et al. (2005) 5-HTTLPR polymorphism impacts human cingulate-amygdala interactions. A genetic susceptibility mechanism for depression. *Nat Neurosci* **8**, 828–834.

[114] CRADDOCK N, OWEN MJ (1996) Candidate gene association studies in psychiatric genetics. A SERTain future. *Mol Psychiatry* **1**, 434–436.

[115] MENDLEWICZ J, MASSAT I, SOUERY D, DEL-FAVERO J, ORUC L, NÖTHEN MM, et al. (2004) Serotonin transporter 5HTTLPR polymorphism and affective disorders. No evidence of association in a large European multicenter study. *Eur J Hum Genet* **12**, 377–382.

[116] DURHAM LK, WEBB SM, MILOS PM, CLARY CM, SEYMOUR AB (2004) The serotonin transporter polymorphism, 5HTTLPR, is associated with a faster response time to sertraline in an elderly population with major depressive disorder. *Psychopharmacology* **174**, 525–529.

[117] KRAFT JB, PETERS EJ, SLAGER SL, JENKINS GD, REINALDA MS, MCGRATH PJ, et al. (2007) Analysis of association between the serotonin transporter and antidepressant response in a large clinical sample. *Biol Psychiatry* **61**, 734–742.

[118] COLEMAN JA, GREEN EM, GOUAUX E (2016) X-ray structures and mechanism of the human serotonin transporter. *Nature* **532**, 334–339.

[119] PENMATSA A, WANG KH, GOUAUX E (2013) X-ray structure of dopamine transporter elucidates antidepressant mechanism. *Nature* **503**, 85–90.

[120] YAMASHITA A, SINGH SK, KAWATE T, JIN Y, GOUAUX E (2005) Crystal structure of a bacterial homologue of Na+/Cl--dependent neurotransmitter transporters. *Nature* **437**, 215–223.

[121] CHEN F, LARSEN MB, NEUBAUER HA, SÁNCHEZ C, PLENGE P, WIBORG O (2005) Characterization of an allosteric citalopram-binding site at the serotonin transporter. *J Neurochem* **92**, 21–28.

[122] PLENGE P, SHI L, BEUMING T, TE J, NEWMAN AH, WEINSTEIN H, et al. (2012) Steric hindrance mutagenesis in the conserved extracellular vestibule impedes allosteric binding of antidepressants to the serotonin transporter. *J Biol Chem* **287**, 39316–39326.

[123] WENNOGLE LP, MEYERSON LR (1982) Serotonin modulates the dissociation of 3Himipramine from human platelet recognition sites. *Eur J Pharmacol* **86**, 303–307.

[124] TORRES GE, AMARA SG (2007) Glutamate and monoamine transporters. New visions of form and function. *Curr Opin Neurobiol* **17**, 304–312.

[125] FENOLLAR-FERRER C, STOCKNER T, SCHWARZ TC, PAL A, GOTOVINA J, HOFMAIER T, et al. (2014) Structure and regulatory interactions of the cytoplasmic terminal domains of serotonin transporter. *Biochemistry* **53**, 5444–5460.

[126] OMASITS U, AHRENS CH, MÜLLER S, WOLLSCHEID B (2014) Protter. Interactive protein feature visualization and integration with experimental proteomic data. *Bioinformatics* **30**, 884–886.

[127] RUDNICK G (2006) Structure/function relationships in serotonin transporter. New insights from the structure of a bacterial transporter. *Handb Exp Pharmacol*, 59–73.

[128] NELSON PJ, RUDNICK G (1979) Coupling between platelet 5-hydroxytryptamine and potassium transport. *J Biol Chem* **254**, 10084–10089.

[129] RUDNICK G (1998) Bioenergetics of neurotransmitter transport. *J Bioenerg Biomembr* **30**, 173–185.

[130] RUDNICK G, NELSON PJ (1978) Platelet 5-hydroxytryptamine transport, an electroneutral mechanism coupled to potassium. *Biochemistry* **17**, 4739–4742.

[131] TALVENHEIMO J, FISHKES H, NELSON PJ, RUDNICK G (1983) The serotonin transporter-imipramine "receptor": different sodium requirements for imipramine binding and serotonin translocation. *J Biol Chem* **258**, 6115–6119.

[132] RASMUSSEN SG, CARROLL FI, MARESCH MJ, JENSEN AD, TATE CG, GETHER U (2001) Biophysical characterization of the cocaine binding pocket in the serotonin transporter using a fluorescent cocaine analogue as a molecular reporter. *J Biol Chem* **276**, 4717–4723.

[133] RUDNICK G (2002) Mechanisms of Biogenic Amine Neurotransmitter Transporters. In: REITH MEA *Neurotransmitter Transporters: Structure, Function, and Regulation*, 25–52. Totowa, NJ: Humana Press.

[134] KAHLIG KM, BINDA F, KHOSHBOUEI H, BLAKELY RD, MCMAHON DG, JAVITCH JA, et al. (2005) Amphetamine induces dopamine efflux through a dopamine transporter channel. *Proc Natl Acad Sci U S A* **102**, 3495–3500.

[135] UHL GR, LIN Z (2003) The top 20 dopamine transporter mutants. Structure–function relationships and cocaine actions. *Eur J Pharmacol* **479**, 71–82.

[136] VOLZ TJ, SCHENK JO (2005) A comprehensive atlas of the topography of functional groups of the dopamine transporter. *Synapse* **58**, 72–94.

[137] NEUBAUER HA, HANSEN CG, WIBORG O (2006) Dissection of an allosteric mechanism on the serotonin transporter. A cross-species study. *Mol Pharmacol* **69**, 1242–1250.

[138] LIN Z, WANG W, UHL GR (2000) Dopamine Transporter Tryptophan Mutants Highlight Candidate Dopamine- and Cocaine-Selective Domains. *Mol Pharmacol* **58**, 1581–1592.

[139] LIN Z (2002) Dopamine Transporter Mutants with Cocaine Resistance and Normal Dopamine Uptake Provide Targets for Cocaine Antagonism. *Mol Pharmacol* **61**, 885–891.

[140] LOLAND CJ (2015) The use of LeuT as a model in elucidating binding sites for substrates and inhibitors in neurotransmitter transporters. *Biochim Biophys Acta* **1850**, 500–510.

[141] COLEMAN JA, GOUAUX E (2018) Structural basis for recognition of diverse antidepressants by the human serotonin transporter. *Nat Struct Mol Biol* **25**, 170–175.

[142] ANDERSEN J, TABOUREAU O, HANSEN KB, OLSEN L, EGEBJERG J, STRØMGAARD K, et al. (2009) Location of the antidepressant binding site in the serotonin transporter. Importance of Ser-438 in recognition of citalopram and tricyclic antidepressants. *J Biol Chem* **284**, 10276–10284.

[143] CELIK L, SINNING S, SEVERINSEN K, HANSEN CG, MØLLER MS, BOLS M, et al. (2008) Binding of serotonin to the human serotonin transporter. Molecular modeling and experimental validation. *J Am Chem Soc* **130**, 3853–3865.

[144] SCHUMANN-GILLETT A, BLYTH MT, O'MARA ML (2018) Is protein structure enough? A review of the role of lipids in SLC6 transporter function. *Neurosci Lett*.

[145] SHI L, QUICK M, ZHAO Y, WEINSTEIN H, JAVITCH JA (2008) The Mechanism of a Neurotransmitter:Sodium Symporter—Inward Release of Na+ and Substrate Is Triggered by Substrate in a Second Binding Site. *Mol Cell* **30**, 667–677.

[146] ZHEN J, REITH MEA (2016) Impact of disruption of secondary binding site S2 on dopamine transporter function. *J Neurochem* **138**, 694–699.

[147] ZHU R, SINWEL D, HASENHUETL PS, SAHA K, KUMAR V, ZHANG P, et al. (2016) Nanopharmacological Force Sensing to Reveal Allosteric Coupling in Transporter Binding Sites. *Angew Chem Int Ed Engl* **55**, 1719–1722.

[148] CHEN F, LARSEN MB, SÁNCHEZ C, WIBORG O (2005) The S-enantiomer of R,S-citalopram, increases inhibitor binding to the human serotonin transporter by an allosteric mechanism. Comparison with other serotonin transporter inhibitors. *Eur Neuropsychopharmacol* **15**, 193–198.

[149] EL MANSARI M, SÁNCHEZ C, CHOUVET G, RENAUD B, HADDJERI N (2005) Effects of acute and long-term administration of escitalopram and citalopram on serotonin neurotransmission. An in vivo electrophysiological study in rat brain. *Neuropsychopharmacology* **30**, 1269–1277.

[150] MANSARI ME, WIBORG O, MNIE-FILALI O, BENTURQUIA N, SÁNCHEZ C, HADDJERI N (2007) Allosteric modulation of the effect of escitalopram, paroxetine and fluoxetine. In-vitro and in-vivo studies. *Int J Neuropsychopharmacol* **10**, 31–40.

[151] ZHONG H, HANSEN KB, BOYLE NJ, HAN K, MUSKE G, HUANG X, et al. (2009) An allosteric binding site at the human serotonin transporter mediates the inhibition of escitalopram by R-citalopram. Kinetic binding studies with the ALI/VFL-SI/TT mutant. *Neurosci Lett* **462**, 207–212.

[152] PLENGE P, GETHER U, RASMUSSEN SG (2007) Allosteric effects of R- and S-citalopram on the human 5-HT transporter. Evidence for distinct high- and low-affinity binding sites. *Eur J Pharmacol* **567**, 1–9.

[153] JACOBSEN JPR, PLENGE P, SACHS BD, PEHRSON AL, CAJINA M, DU Y, et al. (2014) The interaction of escitalopram and R-citalopram at the human serotonin transporter investigated in the mouse. *Psychopharmacology* **231**, 4527–4540.

[154] Genome Compiler Corporation Genome Compiler: Twist Bioscience.

[155] STUDIER FW (2005) Protein production by auto-induction in high-density shaking cultures. *Protein Expres Purif* **41**, 207–234.

[156] AVERY OT (1944) Studies on the chemical nature of the substance inducing transformation of pneumococcal types. Induction of transformation by a desoxyribonucleic acid fraction isolated from pneumococcus type III. *J Exp Med* **79**, 137–158.

[157] DAGERT M, EHRLICH SD (1979) Prolonged incubation in calcium chloride improves the competence of Escherichia coli cells. *Gene* **6**, 23–28.

[158] HANAHAN D (1983) Studies on transformation of Escherichia coli with plasmids. *J Mol Biol* **166**, 557–580.

[159] BERTANI G (1951) Studies on Lysogenesis I. The Mode of Phage Liberation by Lysogenic Escherichia coli. *J Bacteriol* **62**, 293–300.

[160] BIRNBOIM HC, DOLY J (1979) A rapid alkaline extraction procedure for screening recombinant plasmid DNA. *Nucleic Acids Res* **7**, 1513–1523.

[161] MAGNUSDOTTIR A, JOHANSSON I, DAHLGREN L-G, NORDLUND P, BERGLUND H (2009) Enabling IMAC purification of low abundance recombinant proteins from E. coli lysates. *Nat Methods* **6**, 477–478.

[162] HODGES RS, HEATON RJ, PARKER JM, MOLDAY L, MOLDAY RS (1988) Antigen-antibody interaction. Synthetic peptides define linear antigenic determinants recognized by monoclonal antibodies directed to the cytoplasmic carboxyl terminus of rhodopsin. *J Biol Chem* **263**, 11768–11775.

[163] RIGAUD J-L, LÉVY D (2003) Reconstitution of Membrane Proteins into Liposomes. In: DÜZGÜNEŞ N *Liposomes*. *Part B*, 65–86. San Diego, London: Elsevier Academic Press.

[164] GEERTSMA ER, NIK MAHMOOD NAB, SCHUURMAN-WOLTERS GK, POOLMAN B (2008) Membrane reconstitution of ABC transporters and assays of translocator function. *Nat Protoc* **3**, 256–266.

[165] Gasteiger E., Hoogland C., Gattiker A., Duvaud S., Wilkins M.R., Appel R.D., Bairoch A Protein Identification and Analysis Tools on the ExPASy Server. *John M. Walker (ed): The Proteomics Protocols Handbook, Humana Press (2005).*, 571–607.

[166] BRADFORD MM (1976) A rapid and sensitive method for the quantitation of microgram quantities of protein utilizing the principle of protein-dye binding. *Anal Biochem* **72**, 248–254.

[167] LAEMMLI UK (1970) Cleavage of Structural Proteins during the Assembly of the Head of Bacteriophage T4. *Nature* **227**, 680–685.

[168] LADNER CL, YANG J, TURNER RJ, EDWARDS RA (2004) Visible fluorescent detection of proteins in polyacrylamide gels without staining. *Anal Biochem* **326**, 13–20.

[169] Image Lab: Bio-Rad.

[170] TOWBIN H, STAEHELIN T, GORDON J (1979) Electrophoretic transfer of proteins from polyacrylamide gels to nitrocellulose sheets: procedure and some applications. *Proc Natl Acad Sci U S A* **76**, 4350–4354.

[171] BURNETTE WN (1981) "Western blotting": electrophoretic transfer of proteins from sodium dodecyl sulfate--polyacrylamide gels to unmodified nitrocellulose and radiographic detection with antibody and radioiodinated protein A. *Anal Biochem* **112**, 195–203.

[172] HEINICKE E, KUMAR U, MUNOZ DG (1992) Quantitative dot-blot assay for proteins using enhanced chemiluminescence. *J Immunol Methods* **152**, 227–236.

[173] BOIVIN S, KOZAK S, RASMUSSEN G, NEMTANU IM, VIEIRA V, MEIJERS R (2016) An integrated pipeline for sample preparation and characterization at the EMBL@PETRA3 synchrotron facilities. *Methods* **95**, 70–77.

[174] KELLY SM, JESS TJ, PRICE NC (2005) How to study proteins by circular dichroism. *Biochim Biophys Acta* **1751**, 119–139.

[175] KELLY S, PRICE N (2000) The Use of Circular Dichroism in the Investigation of Protein Structure and Function. *CPPS* **1**, 349–384.

[176] GREENFIELD NJ (2006) Using circular dichroism spectra to estimate protein secondary structure. *Nat Protoc* **1**, 2876–2890.

[177] GREENFIELD NJ (2006) Using circular dichroism collected as a function of temperature to determine the thermodynamics of protein unfolding and binding interactions. *Nat Protoc* **1**, 2527–2535.

[178] BENJWAL S, VERMA S, ROHM K-H, GURSKY O (2006) Monitoring protein aggregation during thermal unfolding in circular dichroism experiments. *Protein Sci* **15**, 635–639.

[179] GREENFIELD NJ, FASMAN GD (1969) Computed circular dichroism spectra for the evaluation of protein conformation. *Biochemistry* **8**, 4108–4116.

[180] JOHNSON WC (1999) Analyzing protein circular dichroism spectra for accurate secondary structures. *Proteins* **35**, 307–312.

[181] WHITMORE L, WALLACE BA (2008) Protein secondary structure analyses from circular dichroism spectroscopy: methods and reference databases. *Biopolymers* **89**, 392–400.

[182] ABDUL-GADER A, MILES AJ, WALLACE BA (2011) A reference dataset for the analyses of membrane protein secondary structures and transmembrane residues using circular dichroism spectroscopy. *Bioinformatics* **27**, 1630–1636.

[183] YACHDAV G, KLOPPMANN E, KAJAN L, HECHT M, GOLDBERG T, HAMP T, et al. (2014) PredictProtein--an open resource for online prediction of protein structural and functional features. *Nucleic Acids Res* **42**, W337-43.

[184] KROGH A, LARSSON B, HEIJNE G von, SONNHAMMER EL (2001) Predicting transmembrane protein topology with a hidden Markov model. Application to complete genomes. *J Mol Biol* **305**, 567–580.

[185] SANTORO MM, BOLEN DW (1988) Unfolding free energy changes determined by the linear extrapolation method. 1. Unfolding of phenylmethanesulfonyl .alpha.-chymotrypsin using different denaturants. *Biochemistry* **27**, 8063–8068.

[186] KIRBY EP, STEINER RF (1970) Influence of solvent and temperature upon the fluorescence of indole derivatives. *J Phys Chem* **74**, 4480–4490.

[187] BINSHENG Y (2011) The Stability of a Three-State Unfolding Protein. In: RASTOGI A, GHOSH AK, SURESH SJ *Hydrogen Bond Interactions Between Water Molecules in Bulk Liquid, Near Electrode Surfaces and Around Ions:* INTECH Open Access Publisher.

[188] ALEXANDROV AI, MILENI M, CHIEN EYT, HANSON MA, STEVENS RC (2008) Microscale fluorescent thermal stability assay for membrane proteins. *Structure* **16**, 351–359.

[189] SEMISOTNOV GV, RODIONOVA NA, RAZGULYAEV OI, UVERSKY VN, GRIPAS' AF, GILMANSHIN RI (1991) Study of the "molten globule" intermediate state in protein folding by a hydrophobic fluorescent probe. *Biopolymers* **31**, 119–128.

[190] WIENKEN CJ, BAASKE P, ROTHBAUER U, BRAUN D, DUHR S (2010) Protein-binding assays in biological liquids using microscale thermophoresis. *Nat Commun* **1**, 100.

[191] DUHR S, BRAUN D (2006) Why molecules move along a temperature gradient. *Proc Natl Acad Sci U S A* **103**, 19678–19682.

[192] SEIDEL SAI, DIJKMAN PM, LEA WA, VAN DEN BOGAART G, JERABEK-WILLEMSEN M, LAZIC A, et al. (2013) Microscale thermophoresis quantifies biomolecular interactions under previously challenging conditions. *Methods* **59**, 301–315.

[193] JERABEK-WILLEMSEN M, ANDRÉ T, WANNER R, ROTH HM, DUHR S, BAASKE P, et al. (2014) MicroScale Thermophoresis. Interaction analysis and beyond. *J Mol Struct* **1077**, 101–113.

[194] BAASKE P, WIENKEN CJ, REINECK P, DUHR S, BRAUN D (2010) Optical thermophoresis for quantifying the buffer dependence of aptamer binding. *Angew Chem Int Ed Engl* **49**, 2238–2241.

[195] PATCHING SG (2014) Surface plasmon resonance spectroscopy for characterisation of membrane protein-ligand interactions and its potential for drug discovery. *Biochim Biophys Acta* **1838**, 43–55.

[196] FEE CJ (2013) Label-free, real-time interaction and adsorption analysis 1: surface plasmon resonance. *Methods Mol Biol* **996**, 287–312.

[197] KLOTZ IM (1982) Numbers of receptor sites from Scatchard graphs. Facts and fantasies. *Science* **217**, 1247–1249.

[198] SCATCHARD G (1949) The attractions of proteins for small molecules and ions. *Annals of the New York Academy of Sciences* **51**, 660–672.

[199] HILL AV (1910) The possible effects of the aggregation of the molecules of hæmoglobin on its dissociation curves. January 22, 1910. *J Physiol* **40**, i–vii.

[200] TraceDrawer: Ridgeview Instruments AB.

[201] BIAevaluation: GE Healthcare.

[202] Origin. Northampton, MA: OriginLab.

[203] LANGMUIR I (1918) The asorption of gases on plane surfaces of glass, mica and platinum. *J Am Chem Soc* **40**, 1361–1403.

[204] VOGT AD, DI CERA E (2012) Conformational selection or induced fit? A critical appraisal of the kinetic mechanism. *Biochemistry* **51**, 5894–5902.

[205] KOSHLAND DE, NÉMETHY G, FILMER D (1966) Comparison of Experimental Binding Data and Theoretical Models in Proteins Containing Subunits. *Biochemistry* **5**, 365–385.

[206] KOSHLAND DE (1958) Application of a Theory of Enzyme Specificity to Protein Synthesis. *Proc Natl Acad Sci U S A* **44**, 98–104.

[207] MONOD J, WYMAN J, CHANGEUX JP (1965) On The Nature Of Allosteric Transitions. A Plausible Model. *J Mol Biol* **12**, 88–118.

[208] WOLFRAM RESEARCH I (2018) Mathematica. Champaign, Illinois: Wolfram Research, Inc.

[209] RHODES G (2006) Crystallography made crystal clear. A guide for users of macromolecular models. 3rd ed. Amsterdam: Acad. Press.

[210] MICHEL H (1983) Crystallization of membrane proteins. *Trends Biochem Sci* **8**, 56–59.

[211] RUSSO KRAUSS I, MERLINO A, VERGARA A, SICA F (2013) An overview of biological macromolecule crystallization. *Int J Mol Sci* **14**, 11643–11691.

[212] UJWAL R, BOWIE JU (2011) Crystallizing membrane proteins using lipidic bicelles. *Methods* **55**, 337–341.

[213] LANDAU EM, ROSENBUSCH JP (1996) Lipidic cubic phases: a novel concept for the crystallization of membrane proteins. *Proc Natl Acad Sci U S A* **93**, 14532–14535.

[214] CAFFREY M, CHEREZOV V (2009) Crystallizing membrane proteins using lipidic mesophases. *Nat Protoc* **4**, 706–731.

[215] CAFFREY M (2011) Crystallizing membrane proteins for structure-function studies using lipidic mesophases. *Biochem Soc Trans* **39**, 725–732.

[216] KUBICEK J, SCHLESINGER R, BAEKEN C, BULDT G, SCHAFER F, LABAHN J (2012) Controlled in meso phase crystallization--a method for the structural investigation of membrane proteins. *PLoS One* **7**, e35458.

[217] GARMAN EF, SCHNEIDER TR (1997) Macromolecular Cryocrystallography. *J Appl Crystallogr* **30**, 211–237.

[218] BLACKWELL JR, HORGAN R (1991) A novel strategy for production of a highly expressed recombinant protein in an active form. *FEBS Lett* **295**, 10–12.

[219] TATE CG, HAASE J, BAKER C, BOORSMA M, MAGNANI F, VALLIS Y, et al. (2003) Comparison of seven different heterologous protein expression systems for the production of the serotonin transporter. *BBA - Biomembranes* **1610**, 141–153.

[220] TIWARI PB, WANG X, HE J, DARICI Y (2015) Analyzing surface plasmon resonance data. Choosing a correct biphasic model for interpretation. *Rev Sci Instrum* **86**, 35001.

[221] SCHLEGEL S, LÖFBLOM J, LEE C, HJELM A, KLEPSCH M, STROUS M, et al. (2012) Optimizing membrane protein overexpression in the Escherichia coli strain Lemo21(DE3). *J Mol Biol* **423**, 648–659.

[222] LE MAIRE M, CHAMPEIL P, MOLLER JV (2000) Interaction of membrane proteins and lipids with solubilizing detergents. *Biochim Biophys Acta* **1508**, 86–111.

[223] SEDDON AM, CURNOW P, BOOTH PJ (2004) Membrane proteins, lipids and detergents. Not just a soap opera. *Biochim Biophys Acta* **1666**, 105–117.

[224]. IWATA S (2003) Methods and results in crystallization of membrane proteins. La Jolla Calif.: Internat. Univ. Line.

[225] KILIC F, RUDNICK G (2000) Oligomerization of serotonin transporter and its functional consequences. *Proc Natl Acad Sci U S A* **97**, 3106–3111.

[226] TALVENHEIMO J, RUDNICK G (1980) Solubilization of the platelet plasma membrane serotonin transporter in an active form. *J Biol Chem* **255**, 8606–8611.

[227] LICARI P, BAILEY JE (1991) Factors influencing recombinant protein yields in an insect cell-bacuiovirus expression system. Multiplicity of infection and intracellular protein degradation. *Biotechnol Bioeng* **37**, 238–246.

[228] MICSONAI A, WIEN F, KERNYA L, LEE Y-H, GOTO Y, RÉFRÉGIERS M, et al. (2015) Accurate secondary structure prediction and fold recognition for circular dichroism spectroscopy. *Proc Natl Acad Sci U S A* **112**, E3095-103.

[229] DING F, BORREGUERO JM, BULDYREY SV, STANLEY HE, DOKHOLYAN NV (2003) Mechanism for the alpha-helix to beta-hairpin transition. *Proteins* **53**, 220–228.

[230] LAURSEN L, SEVERINSEN K, KRISTENSEN KB, PERIOLE X, OVERBY M, MÜLLER HK, et al. (2018) Cholesterol binding to a conserved site modulates the conformation, pharmacology, and transport kinetics of the human serotonin transporter. *J Biol Chem* **293**, 3510–3523.

[231] SCANLON SM, WILLIAMS DC, SCHLOSS P (2001) Membrane Cholesterol Modulates Serotonin Transporter Activity. *Biochemistry* **40**, 10507–10513.

[232] YASSINE W, TAIB N, FEDERMAN S, MILOCHAU A, CASTANO S, SBI W, et al. (2009) Reversible transition between alpha-helix and beta-sheet conformation of a transmembrane domain. *Biochim Biophys Acta* **1788**, 1722–1730.

[233] KRISHNAMURTHY H, GOUAUX E (2012) X-ray structures of LeuT in substrate-free outward-open and apo inward-open states. *Nature* **481**, 469–474.

[234] KABSCH W, SANDER C (1983) Dictionary of protein secondary structure. Pattern recognition of hydrogen-bonded and geometrical features. *Biopolymers* **22**, 2577–2637.

[235] MALNASI-CSIZMADIA A, HEGYI G, TOLGYESI F, SZENT-GYORGYI AG, NYITRAY L (1999) Fluorescence measurements detect changes in scallop myosin regulatory domain. *Eur J Biochem* **261**, 452–458.

[236] ABDUL-HUSSEIN S, ANDRÉLL J, TATE CG (2013) Thermostabilisation of the serotonin transporter in a cocaine-bound conformation. *J Mol Biol* **425**, 2198–2207.

[237] GREEN EM, COLEMAN JA, GOUAUX E (2015) Thermostabilization of the Human Serotonin Transporter in an Antidepressant-Bound Conformation. *PLoS One* **10**, e0145688.

[238] CIMMPERMAN P, BARANAUSKIENE L, JACHIMOVICIŪTE S, JACHNO J, TORRESAN J, MICHAILOVIENE V, et al. (2008) A quantitative model of thermal stabilization and destabilization of proteins by ligands. *Biophys J* **95**, 3222–3231.

[239] KABIR A, HONDA RP, KAMATARI YO, ENDO S, FUKUOKA M, KUWATA K (2016) Effects of ligand binding on the stability of aldo-keto reductases. Implications for stabilizer or destabilizer chaperones. *Protein Sci* **25**, 2132–2141.

[240] MATULIS D, KRANZ JK, SALEMME FR, TODD MJ (2005) Thermodynamic stability of carbonic anhydrase. Measurements of binding affinity and stoichiometry using ThermoFluor. *Biochemistry* **44**, 5258–5266.

[241] HASENHUETL PS, SCHICKER K, KOENIG X, LI Y, SARKER S, STOCKNER T, et al. (2015) Ligand Selectivity among the Dopamine and Serotonin Transporters Specified by the Forward Binding Reaction. *Mol Pharmacol* **88**, 12–18.

[242] MARTIN RS, HENNINGSEN RA, SUEN A, APPARSUNDARAM S, LEUNG B, JIA Z, et al. (2008) Kinetic and thermodynamic assessment of binding of serotonin transporter inhibitors. *J Pharmacol Exp Ther* **327**, 991–1000.

[243] TSURUDA PR, YUNG J, MARTIN WJ, CHANG R, MAI N, SMITH JAM (2010) Influence of ligand binding kinetics on functional inhibition of human recombinant serotonin and norepinephrine transporters. *J Pharmacol Tox Met* **61**, 192–204.

[244] MAGNANI F, TATE CG, WYNNE S, WILLIAMS C, HAASE J (2004) Partitioning of the serotonin transporter into lipid microdomains modulates transport of serotonin. *J Biol Chem* **279**, 38770–38778.

[245] CALDERON RO, ATTEMA B, DEVRIES GH (1995) Lipid composition of neuronal cell bodies and neurites from cultured dorsal root ganglia. *J Neurochem* **64**, 424–429.

[246]. Invitrogen Corp. Theory of Binding Data Analysis. Available: https://research.fhcrc.org/content/dam/stripe/hahn/methods/biochem/beacon_fluorescence_guide.pdf.

[247] PLENGE P, MELLERUP ET (1997) An affinity-modulating site on neuronal monoamine transport proteins. *Pharmacol Toxicol* **80**, 197–201.

[248] ZHOU Z, ZHEN J, KARPOWICH NK, GOETZ RM, LAW CJ, REITH MEA, et al. (2007) LeuT-desipramine structure reveals how antidepressants block neurotransmitter reuptake. *Science* **317**, 1390–1393.

[249] SINGH SK, YAMASHITA A, GOUAUX E (2007) Antidepressant binding site in a bacterial homologue of neurotransmitter transporters. *Nature* **448**, 952 EP.

[250] GROSDIDIER A, ZOETE V, MICHIELIN O (2011) SwissDock, a protein-small molecule docking web service based on EADock DSS. *Nucleic Acids Res* **39**, W270-7.

Appendix A - DNA and protein sequences

Human SERT – Bacterial expression

C-Rho-hSERT DNA sequence

ATGGAAACCACCCCGCTGAACAGCCAGAAACAGCTGTCTGCGTGCGAAGATGGCGAAGATTGCCAGGA
AAACGGCGTTCTGCAGAAAGTGGTGCCGACCCCGGGTGATAAAGTGGAAAGCGGCCAGATTAGCAACG
GCTATAGCGCGGTTCCGAGCCCGGGTGCGGGTGATGATACCCGTCATAGCATTCCGGCGACCACCACC
ACCCTGGTGGCGGAACTGCATCAGGGCGAACGTGAAACCTGGGGCAAAAAAGTGGATTTTCTGCTGTC
TGTGATTGGCTATGCGGTGGATCTGGGCAACGTGTGGCGTTTTCCGTATATTTGCTATCAGAACGGCG
GTGGCGCGTTTCTGCTGCCGTATACCATTATGGCGATTTTTGGCGGCATTCCGCTGTTTTATATGGAA
CTGGCCCTGGGTCAGTATCACCGCAACGGCTGCATTAGCATTTGGCGTAAAATCTGCCCGATTTTTAA
AGGCATCGGCTATGCGATTTGCATTATCGCGTTTTATATCGCGAGCTACTACAACACCATCATGGCGT
GGGCGCTGTATTATCTGATTAGCAGCTTTACCGATCAGCTGCCGTGGACCAGCTGCAAAAACAGCTGG
AACACCGGCAATTGCACCAACTATTTCAGCGAAGATAACATTACCTGGACCCTGCATAGCACCAGCCC
GGCGGAAGAATTTTATACCCGTCATGTGCTGCAGATTCATCGTAGCAAAGGCCTGCAGGATCTGGGCG
GCATTAGCTGGCAGCTGGCCCTGTGCATTATGCTGATTTTCACCGTGATCTATTTCAGCATTTGGAAA
GGCGTGAAAACCAGCGGCAAAGTGGTGTGGGTGACCGCGACCTTTCCGTATATCATTCTGAGCGTGCT
GCTGGTGCGTGGTGCGACCCTGCCGGGTGCGTGGCGTGGCGTGCTGTTCTATCTGAAACCGAACTGGC
AGAAACTGCTGGAAACCGGCGTGTGGATTGATGCGGCAGCGCAGATTTTTTTTAGCCTGGGTCCGGGC
TTTGGTGTGCTGCTGGCCTTTGCGAGCTATAACAAATTCAACAACAACTGCTATCAGGATGCGCTGGT
GACCAGCGTGGTGAACTGCATGACCAGCTTTGTGAGCGGCTTTGTGATTTTTACCGTGCTGGGCTATA
TGGCGGAAATGCGTAACGAAGATGTGAGCGAAGTGGCGAAAGATGCGGGTCCGAGCCTGCTGTTTATT
ACCTATGCGGAAGCGATTGCGAACATGCCGGCGAGCACCTTTTTTGCGATCATCTTCTTTCTGATGCT
GATTACCCTGGGCCTGGATAGCACCTTTGCGGGCCTGGAAGGCGTGATTACCGCGGTGCTGGATGAAT
TTCCGCATGTGTGGGCGAAACGTCGTGAACGTTTTGTGCTGGCCGTGGTGATTACCTGCTTTTTTGGC
AGCCTGGTGACCCTGACCTTTGGCGGTGCGTATGTGGTTAAACTGCTGGAAGAATATGCGACCGGTCC
GGCGGTTCTGACCGTGGCGCTGATTGAAGCGGTGGCGGTGAGCTGGTTTTATGGCATTACCCAGTTTT
GCCGTGATGTGAAAGAAATGCTGGGCTTTAGCCCGGGCTGGTTTTGGCGTATTTGCTGGGTGGCGATT
AGCCCGCTGTTTCTGCTGTTTATCATCTGCAGCTTTCTGATGAGCCCGCCGCAGCTGCGTCTGTTTCA
GTATAACTACCCGTATTGGAGCATTATTCTGGGCTATTGCATTGGCACCAGCAGCTTTATTTGCATTC
CGACCTATATTGCGTATCGCCTGATTATTACCCCGGGCACCTTTAAAGAACGCATCATCAAAAGCATT
ACCCCGGAAACCCCGACCGAAATTCCGTGCGGCGATATTCGTCTGAACGCGGTGGGCTCCTCCGGCAC
CGAGACTTCCCAGGTGGCGCCAGTGGGA***TGA***

C-Rho-hSERT Protein sequence

METTPLNSQKQLSACEDGEDCQENGVLQKVVPTPGDKVESGQISNGYSAVPSPGAGDDTRHSIPATTT
TLVAELHQGERETWGKKVDFLLSVIGYAVDLGNVWRFPYICYQNGGGAFLLPYTIMAIFGGIPLFYME
LALGQYHRNGCISIWRKICPIFKGIGYAICIIAFYIASYYNTIMAWALYYLISSFTDQLPWTSCKNSW
NTGNCTNYFSEDNITWTLHSTSPAEEFYTRHVLQIHRSKGLQDLGGISWQLALCIMLIFTVIYFSIWK
GVKTSGKVVWVTATFPYIILSVLLVRGATLPGAWRGVLFYLKPNWQKLLETGVWIDAAAQIFFSLGPG
FGVLLAFASYNKFNNNCYQDALVTSVVNCMTSFVSGFVIFTVLGYMAEMRNEDVSEVAKDAGPSLLFI
TYAEAIANMPASTFFAIIFFLMLITLGLDSTFAGLEGVITAVLDEFPHVWAKRRERFVLAVVITCFFG
SLVTLTFGGAYVVKLLEEYATGPAVLTVALIEAVAVSWFYGITQFCRDVKEMLGFSPGWFWRI
CWVAISPLFLLFIICSFLMSPPQLRLFQYNYPYWSIILGYCIGTSSFICIPTYIAYRLIITPGTFKER
IIKSITPETPTEIPCGDIRLNAVGSSG<u>TETSQVAPA</u>G

N-His$_8$-hSERT DNA sequence

ATGCATCACCATCATCACCATCACCATATGGAAACCACCCCGCTGAACAGCCAGAAACAGCTGTCTGC
GTGCGAAGATGGCGAAGATTGCCAGGAAAACGGCGTTCTGCAGAAAGTGGTGCCGACCCCGGGTGATA
AAGTGGAAAGCGGCCAGATTAGCAACGGCTATAGCGCGGTTCCGAGCCCGGGTGCGGGTGATGATACC
CGTCATAGCATTCCGGCGACCACCACCACCCTGGTGGCGGAACTGCATCAGGGCGAACGTGAAACCTG
GGGCAAAAAAGTGGATTTTCTGCTGTCTGTGATTGGCTATGCGGTGGATCTGGGCAACGTGTGGCGTT
TTCCGTATATTTGCTATCAGAACGGCGGTGGCGCGTTTCTGCTGCCGTATACCATTATGGCGATTTTT
GGCGGCATTCCGCTGTTTTATATGGAACTGGCCCTGGGTCAGTATCACCGCAACGGCTGCATTAGCAT
TTGGCGTAAAATCTGCCCGATTTTTAAAGGCATCGGCTATGCGATTTGCATTATCGCGTTTTATATCG
CGAGCTACTACAACACCATCATGGCGTGGGCGCTGTATTATCTGATTAGCAGCTTTACCGATCAGCTG
CCGTGGACCAGCTGCAAAAACAGCTGGAACACCGGCAATTGCACCAACTATTTCAGCGAAGATAACAT
TACCTGGACCCTGCATAGCACCAGCCCGGCGGAAGAATTTTATACCCGTCATGTGCTGCAGATTCATC
GTAGCAAAGGCCTGCAGGATCTGGGCGGCATTAGCTGGCAGCTGGCCCTGTGCATTATGCTGATTTTC
ACCGTGATCTATTTCAGCATTTGGAAAGGCGTGAAAACCAGCGGCAAAGTGGTGTGGGTGACCGCGAC
CTTTCCGTATATCATTCTGAGCGTGCTGCTGGTGCGTGGTGCGACCCTGCCGGGTGCGTGGCGTGGCG
TGCTGTTCTATCTGAAACCGAACTGGCAGAAACTGCTGGAAACCGGCGTGTGGATTGATGCGGCAGCG
CAGATTTTTTTTAGCCTGGGTCCGGGCTTTGGTGTGCTGCTGGCCTTTGCGAGCTATAACAAATTCAA
CAACAACTGCTATCAGGATGCGCTGGTGACCAGCGTGGTGAACTGCATGACCAGCTTTGTGAGCGGCT
TTGTGATTTTTACCGTGCTGGGCTATATGGCGGAAATGCGTAACGAAGATGTGAGCGAAGTGGCGAAA
GATGCGGGTCCGAGCCTGCTGTTTATTACCTATGCGGAAGCGATTGCGAACATGCCGGCGAGCACCTT
TTTTGCGATCATCTTCTTTCTGATGCTGATTACCCTGGGCCTGGATAGCACCTTTGCGGGCCTGGAAG
GCGTGATTACCGCGGTGCTGGATGAATTTCCGCATGTGTGGGCGAAACGTCGTGAACGTTTTGTGCTG
GCCGTGGTGATTACCTGCTTTTTTGGCAGCCTGGTGACCCTGACCTTTGGCGGTGCGTATGTGGTTAA
ACTGCTGGAAGAATATGCGACCGGTCCGGCGGTTCTGACCGTGGCGCTGATTGAAGCGGTGGCGGTGA
GCTGGTTTTATGGCATTACCCAGTTTTGCCGTGATGTGAAAGAAATGCTGGGCTTTAGCCCGGGCTGG
TTTTGGCGTATTTGCTGGGTGGCGATTAGCCCGCTGTTTCTGCTGTTTATCATCTGCAGCTTTCTGAT
GAGCCCGCCGCAGCTGCGTCTGTTTCAGTATAACTACCCGTATTGGAGCATTATTCTGGGCTATTGCA
TTGGCACCAGCAGCTTTATTTGCATTCCGACCTATATTGCGTATCGCCTGATTATTACCCCGGGCACC
TTTAAAGAACGCATCATCAAAAGCATTACCCCGGAAACCCCGACCGAAATTCCGTGCGGCGATATTCG
TCTGAACGCGGTG***TAATAG***

N-His$_8$-hSERT Protein sequence

MHHHHHHHHMETTPLNSQKQLSACEDGEDCQENGVLQKVVPTPGDKVESGQISNGYSAVPSPGAGDDT
RHSIPATTTTLVAELHQGERETWGKKVDFLLSVIGYAVDLGNVWRFPYICYQNGGGAFLLPYTIMAIF
GGIPLFYMELALGQYHRNGCISIWRKICPIFKGIGYAICIIAFYIASYYNTIMAWALYYLISSFTDQL
PWTSCKNSWNTGNCTNYFSEDNITWTLHSTSPAEEFYTRHVLQIHRSKGLQDLGGISWQLALCIMLIF
TVIYFSIWKGVKTSGKVVWVTATFPYIILSVLLVRGATLPGAWRGVLFYLKPNWQKLLETGVWIDAAA
QIFFSLGPGFGVLLAFASYNKFNNNCYQDALVTSVVNCMTSFVSGFVIFTVLGYMAEMRNEDVSEVAK
DAGPSLLFITYAEAIANMPASTFFAIIFFLMLITLGLDSTFAGLEGVITAVLDEFPHVWAKRRERFVL
AVVITCFFGSLVTLTFGGAYVVKLLEEYATGPAVLTVALIEAVAVSWFYGITQFCRDVKEMLGFSPGW
FWRICWVAISPLFLLFIICSFLMSPPQLRLFQYNYPYWSIILGYCIGTSSFICIPTYIAYRLIITPGT
FKERIIKSITPETPTEIPCGDIRLNAV

Human SERT – Baculovirus/Insect cell expression

C-Rho-hSERT-Sf9 DNA sequence

ATGGAAACTACCCCCCTGAACAGCCAGAAGCAGCTGTCCGCCTGCGAGGATGGCGAGGACTGCCAGGA
AAACGGCGTCCTGCAGAAAGTGGTGCCCACCCCTGGCGATAAGGTGGAGAGCGGCCAGATCAGCAACG
GCTACAGCGCCGTGCCTTCTCCTGGCGCTGGCGACGACACCAGACACAGCATCCCCGCCACCACCACA
ACACTGGTGGCCGAGCTGCACCAGGGCGAGAGGGAAACCTGGGGCAAGAAGGTGGACTTCCTGCTGTC
CGTGATCGGCTACGCCGTGGACCTGGGCAACGTGTGGCGGTTCCCCTACATCTGCTACCAGAATGGCG
GCGGAGCCTTCCTGCTGCCCTACACCATCATGGCCATCTTCGGCGGCATCCCCCTGTTCTACATGGAA
CTGGCTCTGGGACAGTATCACCGGAACGGCTGCATCAGCATCTGGCGGAAGATCTGCCCCATCTTCAA
GGGCATCGGCTATGCCATCTGCATCATTGCCTTCTACATTGCCAGCTACTACAACACAATCATGGCCT
GGGCCCTGTACTACCTGATCAGCAGCTTCACCGACCAGCTGCCCTGGACCAGCTGCAAGAACAGCTGG
AACACCGGCAACTGCACCAACTACTTCAGCGAGGACAACATCACCTGGACCCTGCACAGCACCAGCCC
TGCCGAGGAATTCTACACCCGGCATGTGCTGCAGATCCACCGGTCCAAGGGCCTGCAGGATCTGGGCG
GCATCTCTTGGCAGCTGGCCCTGTGCATCATGCTGATCTTCACCGTGATCTACTTCTCCATCTGGAAG
GGCGTGAAAACCAGCGGCAAGGTGGTGTGGGTGACCGCCACCTTCCCTTACATCATCCTGAGCGTGCT
GCTGGTGCGGGGAGCCACACTGCCTGGCGCTTGGAGGGGCGTGCTGTTCTACCTGAAGCCCAACTGGC
AGAAGCTGCTGGAAACCGGCGTGTGGATCGACGCCGCTGCCCAGATCTTCTTCTCCCTGGGACCTGGC
TTTGGAGTGCTGCTGGCCTTCGCCAGCTACAACAAGTTCAACAACAACTGCTACCAGGACGCCCTGGT
GACCAGCGTGGTGAACTGCATGACCAGCTTCGTGAGCGGCTTCGTGATCTTTACCGTGCTGGGCTACA
TGGCCGAGATGCGGAACGAGGACGTGAGCGAGGTGGCCAAGGATGCCGGCCCTAGCCTGCTGTTCATC
ACCTACGCCGAGGCCATTGCCAACATGCCCGCCAGCACCTTTTTCGCCATCATCTTTTTTCTGATGCT
GATCACCCTGGGCCTGGACAGCACCTTTGCCGGCCTGGAAGGCGTGATCACCGCCGTGCTGGACGAGT
TTCCCCACGTGTGGGCCAAGCGGCGGGAGAGATTCGTGCTGGCCGTGGTGATCACCTGCTTTTTCGGC
AGCCTGGTGACCCTGACCTTTGGCGGAGCCTACGTGGTGAAACTGCTGGAAGAGTACGCCACAGGCCC
TGCCGTGCTGACAGTGGCCCTGATCGAGGCCGTGGCCGTGAGCTGGTTCTACGGCATCACCCAGTTCT
GCCGGGACGTGAAAGAGATGCTGGGCTTCAGCCCCGGCTGGTTCTGGCGGATCTGCTGGGTGGCCATC
AGCCCCCTGTTTCTGCTGTTTATCATCTGCAGCTTTCTGATGAGCCCCCCTCAGCTGCGGCTGTTCCA
GTACAACTACCCCTACTGGTCCATCATCCTGGGCTACTGCATCGGCACCTCCAGCTTCATCTGCATCC
CCACCTACATTGCCTACCGGCTGATCATTACACCCGGCACCTTCAAAGAGCGGATCATCAAGAGCATC
ACCCCTGAGACACCCACCGAGATCCCTTGCGGCGACATCAGGCTGAACGCCGTGGGCTCCTCCGGCAC
CGAGACTTCCCAGGTGGCGCCAGCT***TGATGA***

C-Rho-hSERT-Sf9 Protein sequence

METTPLNSQKQLSACEDGEDCQENGVLQKVVPTPGDKVESGQISNGYSAVPSPGAGDDTRHSIPATTT
TLVAELHQGERETWGKKVDFLLSVIGYAVDLGNVWRFPYICYQNGGGAFLLPYTIMAIFGGIPLFYME
LALGQYHRNGCISIWRKICPIFKGIGYAICIIAFYIASYYNTIMAWALYYLISSFTDQLPWTSCKNSW
NTGNCTNYFSEDNITWTLHSTSPAEEFYTRHVLQIHRSKGLQDLGGISWQLALCIMLIFTVIYFSIWK
GVKTSGKVVWVTATFPYIILSVLLVRGATLPGAWRGVLFYLKPNWQKLLETGVWIDAAAQIFFSLGPG
FGVLLAFASYNKFNNNCYQDALVTSVVNCMTSFVSGFVIFTVLGYMAEMRNEDVSEVAKDAGPSLLFI
TYAEAIANMPASTFFAIIFFLMLITLGLDSTFAGLEGVITAVLDEFPHVWAKRRERFVLAVVITCFFG
SLVTLTFGGAYVVKLLEEYATGPAVLTVALIEAVAVSWFYGITQFCRDVKEMLGFSPGWFWRICWVAI
SPLFLLFIICSFLMSPPQLRLFQYNYPYWSIILGYCIGTSSFICIPTYIAYRLIITPGTFKERIIKSI
TPETPTEIPCGDIRLNAVGSSGTETSQVAPA

C-His8-hCNX-Sf9 DNA sequence

ATGGAAGGCAAGTGGCTGCTGTGCATGCTGCTGGTGCTGGGAACCGCTATCGTGGAAGCTCACGACGG
TCACGACGACGACGTGATCGACATCGAGGACGACCTGGACGATGTCATCGAGGAAGTCGAGGACTCCA
AGCCTGATACCACCGCTCCTCCATCCTCACCTAAAGTGACCTACAAGGCTCCCGTGCCTACCGGCGAA
GTGTACTTCGCTGACTCCTTCGACCGTGGCACCCTGTCCGGATGGATCTTGTCCAAGGCTAAGAAGGA
CGACACCGACGACGAAATCGCTAAGTACGACGGCAAGTGGGAAGTCGAAGAGATGAAGGAATCCAAGC
TGCCCGGCGACAAGGGCCTCGTGTTGATGTCTAGAGCTAAGCACCACGCTATCTCCGCCAAGCTGAAC
AAGCCCTTCCTGTTCGACACCAAGCCTCTGATCGTGCAGTACGAAGTGAACTTCCAGAACGGTATCGA
GTGCGGTGGCGCTTACGTGAAGCTGCTGTCTAAGACCCCTGAGCTGAACCTGGACCAGTTCCACGACA
AGACCCCTTACACCATCATGTTCGGTCCCGACAAGTGCGGCGAGGACTACAAGTTGCACTTCATCTTC
CGTCACAAGAACCCCAAGACCGGCATCTACGAGGAAAAGCACGCTAAGCGTCCCGACGCTGACCTCAA
GACCTACTTCACCGACAAGAAAACCCACCTGTACACCCTGATCTTGAACCCCGACAACTCTTTCGAGA
TCCTGGTGGACCAGTCCGTGGTCAACTCCGGCAACCTGCTGAACGACATGACCCCACCTGTGAACCCT
AGCCGCGAAATCGAGGACCCTGAGGATAGGAAGCCTGAGGACTGGGACGAGCGTCCTAAGATCCCTGA
TCCTGAGGCTGTGAAGCCCGACGATTGGGACGAAGATGCTCCCGCTAAGATTCCCGACGAGGAAGCTA
CCAAGCCAGAAGGCTGGCTGGACGACGAGCCTGAGTACGTGCCAGATCCAGACGCTGAGAAACCAGAG
GACTGGGATGAAGATATGGACGGCGAATGGGAAGCTCCCCAGATCGCTAACCCTCGTTGCGAGTCTGC
TCCTGGTTGCGGTGTTTGGCAGCGTCCCGTGATCGATAACCCCAACTACAAAGGCAAATGGAAGCCGC
CTATGATCGACAACCCTTCCTACCAAGGCATCTGGAAGCCCCGCAAGATCCCCAATCCTGACTTCTTC
GAGGACCTCGAGCCTTTCCGTATGACCCCTTTCTCCGCTATCGGCCTCGAGCTGTGGTCTATGACCTC
CGACATCTTCTTCGACAACTTCATCATCTGCGCTGACCGTCGCATCGTGGACGACTGGGCTAATGACG
GATGGGGCCTGAAGAAAGCTGCTGACGGTGCTGCTGAGCCTGGTGTCGTGGGTCAAATGATCGAGGCT
GCTGAGGAACGCCCTTGGCTGTGGGTTGTGTACATCCTGACTGTGGCTCTGCCCGTGTTCCTGGTCAT
CCTGTTCTGCTGCTCCGGCAAGAAACAGACCTCCGGCATGGAGTACAAAAAGACCGACGCTCCCCAGC
CTGACGTCAAAGAGGAAGAAGAAGAGAAAGAAGAGGAAAAGGACAAGGGCGACGAGGAAGAGGAAGGC
GAGGAAAAGTTGGAAGAGAAGCAGAAGTCCGACGCCGAAGAGGACGGTGGCACCGTGTCTCAAGAGGA
AGAGGACCGCAAGCCTAAGGCTGAAGAGGATGAGATCCTGAACAGGTCCCCTCGTAACAGAAAGCCCC
GTCGCGAACACCACCATCATCACCATCACCAC***TAATAA***

C-His8-hCNX-Sf9 Protein sequence

MEGKWLLCMLLVLGTAIVEAHDGHDDDVIDIEDDLDDVIEEVEDSKPDTTAPPSSPKVTYKAPVPTGE
VYFADSFDRGTLSGWILSKAKKDDTDDEIAKYDGKWEVEEMKESKLPGDKGLVLMSRAKHHAISAKLN
KPFLFDTKPLIVQYEVNFQNGIECGGAYVKLLSKTPELNLDQFHDKTPYTIMFGPDKCGEDYKLHFIF
RHKNPKTGIYEEKHAKRPDADLKTYFTDKKTHLYTLILNPDNSFEILVDQSVVNSGNLLNDMTPPVNP
SREIEDPEDRKPEDWDERPKIPDPEAVKPDDWDEDAPAKIPDEEATKPEGWLDDEPEYVPDPDAEKPE
DWDEDMDGEWEAPQIANPRCESAPGCGVWQRPVIDNPNYKGKWKPPMIDNPSYQGIWKPRKIPNPDFF
EDLEPFRMTPFSAIGLELWSMTSDIFFDNFIICADRRIVDDWANDGWGLKKAADGAAEPGVVGQMIEA
AEERPWLWVVYILTVALPVFLVILFCCSGKKQTSGMEYKKTDAPQPDVKEEEEEKEEEKDKGDEEEEG
EEKLEEKQKSDAEEDGGTVSQEEEDRKPKAEEDEILNRSPRNRKPRRE<u>HHHHHHHH</u>

Acknowledgements

It is a pleasure to thank the many people who made this thesis possible.

First of all, I would like to express my sincere gratitude to my advisor Prof. Dr. Jörg Labahn for his continuous support and encouragement of my PhD study and the related research, for his patience and guidance. I would like to thank Prof. Dr. Henrike Heise for the co-supervision of this thesis. Furthermore, I want to thank Dr. Barbara Maertens, Dr. Jan Kubicek and Dr. Roland Fabis from Cube Biotech for an exciting collaboration and for their support.

I sincerely thank Dr. Udaya Kumar Tiruttani Subhramanyam for guiding me when I joined the group. I am truly grateful for his supervision over the four years, for every discussion we had and for all his help academically and personally. I would like to thank my colleagues, Dr. Ge Yang and Dr. Kun Yu, for their insightful comments on my project whenever necessary. It has been very nice to be lab mates with them. I will always remember the fun we had in our lab. In addition, I would like to thank Sabrina Kress and Abhilasha Singh for their great support in our lab.

My special thanks goes to Dr. Maria Marta Garcia Alai, Ioana Maria Nemtanu, and Janina Hinrichs from SPC at EMBL Hamburg for their help with Biacore and Nanotemper experiments.

I would like to thank the Federal Ministry of Education and Research and Research Center Jülich for the financial support during my PhD study.

Last but not least, I would like to thank my parents, my family and my friends for their great support during my studies and their constant encouragement.

Scientific publication

Parts of this work have been submitted for publication in the scientific journal “Protein Expression and Purification” published by Elsevier. Development, planning, design, execution and evaluation of experiments was done by Daniel Worms. Jörg Labahn and Udaya Kumar Tiruttani Subhramanyam supported the submitted work with scientific discussions.

Erklärung

Ich erkläre, dass ich die vorliegende Arbeit selbständig und ohne unerlaubte Hilfe verfasst habe. Die vorliegende Arbeit wurde weder in der jetzigen oder in ähnlicher Form bei einer anderen Institution eingereicht. Es wurden zuvor keine Promotionsversuche unternommen.

Hamburg, _____

Daniel Worms